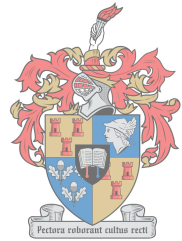


# New Developments in the Nuclear Binary Cluster-Core in the Heavy Nuclear Region

by

Boniface Dimitri Christel KIMENE KAYA



UNIVERSITEIT  
iYUNIVESITHI  
STELLENBOSCH  
UNIVERSITY

100  
1918 - 2018

*Dissertation presented for the degree of Doctorate of  
Philosophy in the Faculty of Sciences at Stellenbosch  
University*

Supervisors:

Prof. Shaun M. Wyngaardt  
Prof. B.I.S Van der Ventel

March 2018

# Declaration

By submitting this dissertation electronically, I declare that the entirety of the work contained therein is my own, original work, that I am the sole author thereof (save to the extent explicitly otherwise stated), that reproduction and publication thereof by Stellenbosch University will not infringe any third party rights and that I have not previously in its entirety or in part submitted it for obtaining any qualification.

Copyright © 2018 Stellenbosch University  
All rights reserved.

# Abstract

## New Developments in the Nuclear Binary Cluster-Core in the Heavy Nuclear Region

B. D. C. KIMENE KAYA

*Department of Physics,  
University of Stellenbosch,  
Private Bag X1, Matieland 7602, South Africa.*

Dissertation: PhD

November 2017

The atomic nucleus is a complex many-body interacting system, which exhibits a underlying correlated set of nucleon states. The cluster model is one of the most reliable models that predicts the strongly correlated subsystem of nucleons close to the decay threshold of nuclei. The binary-cluster model describes the structure and decay properties of super-heavy nuclei.

The phenomenological Cubic Woods-Saxon potential, developed by Buck, Merchant and Perez, has successfully predicted a number of experimental observables associated with clustering phenomenon. The recently developed microscopic double folded M3Y potential results in the inverted spectra for the positive parity excited cluster states, but successfully predicts the decay half-life for the  $\alpha$ -Pb system. These shortcomings of the M3Y based microscopic binary cluster model lead to the newly developed hybrid cluster-core potential, obtained by fitting the phenomenological Saxon-Woods Cubed and the M3Y double folding at the surface region where the two potentials coalesce.

The project presents an overview on nuclear cluster models. The double folding potentials are constructed with the M3Y and the new complex effective Gaussian form factor (CEG) effective nucleon-nucleon interactions. Furthermore the recently developed self-consistent relativistic mean-field cluster-core description is presented with the relativistic Love-Franey amplitudes. The decay half-lives for  $\alpha$ -Pb give satisfactory results for M3Y and CEG with the addition

of a zero-range exchange potential. However, the CEG with a finite-range and the relativistic mean field approach potentials for all cluster-core configurations  $\alpha$ -Pb, C-Pb and O-Pb except Be-Pb, give decay half-lives that overestimate the experimental values. The generated positive parity level structures are inverted for  $\alpha$ -Pb when compared to other cluster configurations which are compressed although positive. Finally we construct the hybrid cluster-core potential from different microscopic potential models. We find that predictions for the positive parity level structure, the transition probability, nuclear charge radii and deformation parameters are in good agreement with the corresponding experimental data for most cluster-core configurations.

# Uittreksel

## Nuwe Ontwikkeling in die Binêre Kern Bondel-Kern Model in die Swaar Kern Gebied

B. D. C. KIMENE KAYA

*Fisika Departement,  
Universiteit van Stellenbosch,  
Privaatsak X1, Matieland 7602, Suid Afrika.*

Proefskrif: PhD

March 2018

Die atoomkern is 'n komplekse veeldeeltjie interaksie sisteem, wat die onderliggende korrelasies van nukleon toestande uitlig. Die bondel model is een van die mees betroubare modelle wat die sterk korrelerende subsisteem van nukleone naby die drumpel van kern verval voorspel. Die binêre-bondel model beskryf die struktuur en verval eienskappe van super swaar kerne.

Die fenomenologiese Kubiese Woods-Saxon potensiaal, beskryf deur Buck, Merchant en Perez, is suksesvol in die beskrywing van 'n aantal eksperimentele waarneembare wat geassosieer word met die bondelings verskynsel. Die onlangse ontwikkelde mikroskopiese dubbele gevoude M3Y potensiaal gee 'n omgekeerde spektrum van die positiewe partiteit opgewekte toestande, maar is suksesvol in die voorspelling van die verval halfleeftyd van die  $\alpha$ -Pb sisteem. Hierdie tekortkomminge van die M3Y gebaseerde mikroskopiese binêre-bondel model lei tot die nuut ontwikkelde hibried bondel-kern potensiaal, deur die fenomenologiese Kubiese Woods-Saxon potensiaal en die M3Y dubbel gevoude potensiaal by die oppervlak gebied waar die twee potensiale oorvleuel, te pas.

Die projek bied aan 'n oorsig van kern bondel modelle. Die dubbelgevoude potensiale is gekonstrueer deurmiddel van die M3Y en die nuwe kompleks effektiewe Gaussian vorm faktor (CEG). Verder word die onlangse self konsistente ontwikkelde relativistiese gemideelde veld bondel-kor beskryf. Die

verval halfleeftyd van  $\alpha$ -Pb gee bevredigende resultate vir M3Y en CEG met die byvoeging van 'n nul reeks ruil potensiaal. Alhoewel CEG met 'n eindigende reeks en relativistiese gemiddelde veld benadering, word potensiale vir alle konfigurasies van  $\alpha$ -Pb, C-Pb and O-Pb geproduseer, behalwe vir Be-Pb, wat die eksperimentele waardes oorskakel. Die genereerde positiewe pariteitsvlak strukture is omgekeerd vir  $\alpha$ -Pb wanneer dit vergelyk word met die ander bondel opset wat saamgepers is. Laastens was die hibride bondel-kor potensiaal van verskillende mikroskopiese potensiale gekonstrueer. Die voorspellings van die positiewe pariteitsvlak strukture was gekry. Die oorgangs waarskynlikheid, kernladings radius en vervormings parameters stem ooreen met die ooreenstemmende eksperimentele data vir meeste van die bondel-kern konfigurasies.

# Acknowledgements

All praise is for God, the most High, without whom the completion of this project would have not been possible.

I am so greatly indebted to my promoters Prof S. M. Wyngaardt and B. I. S van der Ventel for suggesting such an exciting project. Their simplicity and strong encouragement to motivate me through out my Ph.D. project. They have shown me their tremendous guidance, put up with me in patience and numerous open and fruitful discussions. These have contributed to the success of my work. They have taught me most of tools that I know in computing with various programming languages useful for my simulations, and also their kindness with many of my insignificant questions.

I would like to express my sincere thanks to my co-promoter Dr T. T. IBRAHIM who paved the way in suggesting new elements that have been included in the project and providing with the code that have been used for calculations.

I would like also to thank all the department members and colleagues for the time they spent to support me and specially to Wasiu, my officemate for helpful interactions.

I feel so privileged for having received funding from the department of physics through the National Institute of Theoretical Physics (NITheP) and Stellenbosch University, and the top-up from ICS-INDUSTRIAL Company led by my uncle Mr Boniface Kaya. These have helped me to immerse myself in completing my thesis.

Finally I would like to thank my family , and particularly my wife for supporting and being patient with me during the last times that I was finalizing my project. Specially thanks to my uncles, Mr Cyrille Kimenet Kimosso and Mr Boniface Kaya considered as pillar and model of my family for their support and encouragements. My son Nathan Kimene and Daughter Winner Kimene.

# Contents

<b>Declaration</b>	<b>i</b>
<b>Abstract</b>	<b>ii</b>
<b>Uittreksel</b>	<b>iv</b>
<b>Acknowledgements</b>	<b>vi</b>
<b>Contents</b>	<b>vii</b>
<b>List of Figures</b>	<b>ix</b>
<b>List of Tables</b>	<b>xi</b>
<b>1 Introduction</b>	<b>1</b>
<b>2 Binary Cluster Model and Structure Observables</b>	<b>6</b>
2.1 Introduction . . . . .	6
2.2 Cluster-Core Configuration . . . . .	6
2.3 Decay Half-Life and Width . . . . .	13
2.4 Level Structures and Electromagnetic Transitions . . . . .	16
2.5 Mean Square Charge Radius . . . . .	27
2.6 Deformations Parameters . . . . .	27
<b>3 Nuclear Cluster-Core Potential</b>	<b>28</b>
3.1 Introduction . . . . .	28
3.2 Phenomenological Nuclear Potential . . . . .	28
3.3 Microscopic Nonrelativistic Nuclear Potential . . . . .	29
3.4 Microscopic Relativistic Nuclear Potential . . . . .	40
3.5 Relativistic Nuclear Densities . . . . .	56
<b>4 Numerical Analysis and Observables</b>	<b>62</b>
4.1 Introduction . . . . .	62
4.2 Double Folding Potential Calculation . . . . .	62
4.3 Hybrid Potential Construction . . . . .	76



<i>CONTENTS</i>	viii
<b>5 Conclusions and Outlook</b>	<b>91</b>
<b>List of References</b>	<b>93</b>

# List of Figures

2.1	Fit to binding energy data (shown as blue dot) with mathematica package for stable even $A$ nuclei using the liquid drop model with coefficients given in the text, the predictions (actual binding energy) are shown as black dot. Notice the strong deviations at the magic numbers. . . . .	8
2.2	Central effective potential versus cluster-core relative position $r$ . The three classical turning points are illustrated for a specific given state energy $E$ . . . . .	16
2.3	Central potential with localized classical turning points where arrows indicate connecting regions. . . . .	20
2.4	Coordinates representation of cluster-core relative motion . . . . .	24
3.1	Cluster-Core coordinates used in the double folded model . . . . .	39
3.2	Relativistic direct and exchange one-meson diagrams for the Love-Franey model. . . . .	47
4.1	Plots of cluster-core local potential for ${}^4\text{He} + {}^{208}\text{Pb}$ . CEG83a (zero-range exchange interaction) and CEG83b (finite-range exchange interaction) along with the phenomenological Saxon-Woods potential, SW3 (black dashed line) . . . . .	65
4.2	Plots of cluster-core local potential for ${}^{10}\text{Be} + {}^{208}\text{Pb}$ . CEG83a (zero-range exchange interaction) and CEG83b (finite-range exchange interaction) along with the phenomenological Saxon-Woods potential, SW3 (black dashed line) . . . . .	66
4.3	Plots of cluster-core local potential for ${}^{14}\text{C} + {}^{208}\text{Pb}$ . CEG83a (zero-range exchange interaction) and CEG83b (finite-range exchange interaction) along with the phenomenological Saxon-Woods potential, SW3 (black dashed line) . . . . .	66
4.4	Plots of cluster-core local potential for ${}^{20}\text{O} + {}^{208}\text{Pb}$ . CEG83a (zero-range exchange interaction) and CEG83b (finite-range exchange interaction) along with the phenomenological Saxon-Woods potential, SW3 (black dashed line) . . . . .	67

4.5	Scalar and vector ${}^4\text{He}$ nucleons densities distribution. Top and bottom panels are results calculated with NL3 and FSU Lagrangian densities . . . . .	68
4.6	Scalar and vector ${}^{10}\text{Be}$ nucleons densities distribution. Top and bottom panels are results calculated with NL3 and FSU Lagrangian densities . . . . .	69
4.7	Scalar and vector ${}^{14}\text{C}$ nucleons densities distribution. Top and bottom panels are results calculated with NL3 and FSU Lagrangian densities . . . . .	70
4.8	Scalar and vector ${}^{20}\text{O}$ nucleons densities distribution. Top and bottom panels are results calculated with NL3 and FSU Lagrangian densities . . . . .	71
4.9	Scalar and vector ${}^{208}\text{Pb}$ nucleons densities distribution. Top and bottom panels are results calculated with NL3 and FSU Lagrangian densities . . . . .	72
4.10	Plot of the individual scalar and vector potentials (left panel) for a typical parameter set, NL3 and FSU Lagrangian densities. The right panel is the total potential resulting from the near-cancellation of scalar and vector terms for ${}^4\text{He} + {}^{208}\text{Pb}$ , and the phenomenological Saxon-Woods potential, SW3 (blue line) . . . . .	72
4.11	Plot of the individual scalar and vector potentials (left panel) for a typical parameter set, NL3 and FSU Lagrangian densities. The right panel is the total potential resulting from the near-cancellation of scalar and vector terms for ${}^{10}\text{Be} + {}^{208}\text{Pb}$ , and the phenomenological Saxon-Woods potential, SW3 (blue line) . . . . .	74
4.12	Plot of the individual scalar and vector potentials (left panel) for a typical parameter set, NL3 and FSU Lagrangian densities. The right panel is the total potential resulting from the near-cancellation of scalar and vector terms for ${}^{14}\text{C} + {}^{208}\text{Pb}$ , and the phenomenological Saxon-Woods potential, SW3 (blue line) . . . . .	74
4.13	Plot of the individual scalar and vector potentials (left panel) for a typical parameter set, NL3 and FSU Lagrangian densities. The right panel is the total potential resulting from the near-cancellation of scalar and vector terms for ${}^{20}\text{O} + {}^{208}\text{Pb}$ , and the phenomenological Saxon-Woods potential, SW3 (blue line) . . . . .	75

# List of Tables

2.1	Different cluster partitions used in our models . . . . .	11
3.1	gamma matrices of the Dirac space . . . . .	44
3.2	Parameters used for different QHD models given in MeV . . . . .	61
4.1	The parameters of the Reid M3Y interactions . . . . .	63
4.2	Parameters of the central part for the CEG83 in the range (fm); $\lambda_1 = 2.500$ , $\lambda_2 = 0.8900$ , $\lambda_3 = 0.5000$ . . . . .	64
4.3	Real RLF parameters. The last parameters are dimensionless except the masses and cutoff parameters which are in MeV . . . . .	73
4.4	Normalization constant for different potential models . . . . .	75
4.5	Decay widths calculated with different potential models and their corresponding values extracted from experimental decay half – lives	76
4.6	Decay half – lives obtained with different potential models . . . . .	77
4.7	Spectrum of positive parity for ${}^4_2\text{He} + {}^{208}_{82}\text{Pb}$ in MeV calculated with different potential models and their experimental values in MeV . .	78
4.8	Spectrum of positive parity for ${}^{10}_4\text{Be} + {}^{208}_{82}\text{Pb}$ in MeV calculated with different potential models and their experimental values in MeV. . .	79
4.9	Spectrum of positive parity for ${}^{14}_6\text{C} + {}^{208}_{82}\text{Pb}$ in MeV calculated with different potential models and their experimental values in MeV. .	80
4.10	Spectrum of positive parity for ${}^{20}_8\text{O} + {}^{208}_{82}\text{Pb}$ in MeV calculated with different potential models and their experimental values in MeV. .	81
4.11	Optimized paramters for SW3 potential for ${}^{212}_{84}\text{Po}$ . . . . .	82
4.12	Optimized paramters for SW3 potential for ${}^{218}_{86}\text{Rn}$ . . . . .	82
4.13	Optimized paramters for SW3 potential for ${}^{222}_{88}\text{Ra}$ . . . . .	83
4.14	Optimized paramters for SW3 potential for ${}^{228}_{90}\text{Th}$ . . . . .	83
4.15	Spectrum of positive parity for ${}^4_2\text{He} + {}^{208}_{82}\text{Pb}$ in MeV calculated with different potential models and their experimental values in MeV. .	84
4.16	Spectrum of positive parity for ${}^{10}_4\text{Be} + {}^{208}_{82}\text{Pb}$ in MeV calculated with hybrid potential models and their experimental values in MeV. . .	85
4.17	Spectrum of positive parity for ${}^{14}_6\text{C} + {}^{208}_{82}\text{Pb}$ in MeV calculated with hybrid potential models and their experimental values in MeV. . .	86
4.18	Spectrum of positive parity for ${}^{20}_8\text{O} + {}^{208}_{82}\text{Pb}$ in MeV calculated with hybrid potential models and their experimental values in MeV. . .	87

4.19	Electromagnetic transitions calculated for different hybrid potentials along with experimental values in Weisskopf unit (W.u.), for $^{212}_{84}\text{Po}$	88
4.20	Electromagnetic transitions calculated for different hybrid potentials along with experimental values in Weisskopf unit (W.u.), for $^{218}_{84}\text{Rn}$	88
4.21	Electromagnetic transitions calculated for different hybrid potentials along with experimental values in Weisskopf unit (W.u.), for $^{222}_{88}\text{Ra}$	89
4.22	Electromagnetic transitions calculated for different hybrid potentials along with experimental values in Weisskopf unit (W.u.), for $^{228}_{90}\text{Th}$	89
4.23	The deformation parameters $\beta_2$ calculated with NL3 Lagrangian, and cluster model predictions for the root mean square charge radii, $\langle r_{ch}^2 \rangle^{1/2}$ in fm along with the measured values. . . . .	90

# Chapter 1

## Introduction

Nuclear matter exhibits varied and rich structure due to its complexity and the unknown nature of the nucleon-nucleon strong interaction that has still not been pinned down to any definite form. Since the many-body of strongly interacting nucleons cannot be solved exactly, one has to look for alternative approximations. These are approximate methods which are at the heart of nuclear models developed in the past decades. Consequently, in one sight, nuclei behave as a liquid drop in which the nucleus is treated as an incompressible quantum drop of the uniform density. This is a consequence of strong correlations resulting from the long range attraction and the short range repulsion of mutual interaction among nucleons including the charges of protons, which bind them. The nuclear binding energies and masses are then determined from the " semi-empirical-mass-formulae", C.F. von Weizsäcker, [1], for an unknown nuclei with arbitrary  $A$  and  $Z$ . However, we notice a major discontinuity in binding energies occurring at particular neutron and proton numbers which cannot be explained by the liquid drop model. Eventually these peculiar numbers are well described by the shell model (independent particle model) and are called "magic numbers" in which nuclear binding energies are particularly strong. They indicate the shell closure [2]. Although this model, successfully predicted nuclear spins and parities of ground state, but failed to reproduce magnetic moments and spins of excited states with any real certainty. Therefore, the nucleus displays collective behaviour (collective model) arising from residual interactions between neutrons and protons that are located further away from closed shells (valence nucleons) [3]. It describes a nucleus as being made of a hard core of nucleons in completely filled shells similar to shell model, with outer valence nucleons acting as surface molecules of a liquid drop. In fact, this is a reconciliation between the liquid drop and shell models. Not only a single nucleon is involved, but the entire nucleus acting as a whole. Two modes of excitation are possible, either the nucleus acquires a rotational mode due to the surface motion of valence nucleons (strong deformation) or vibrational mode, involving both the core and surface (fluctuation of nuclear shape).

These two modes of excitations, generally are confirmed by experiment where they are able to predict electric quadrupole and magnetic moments with some success. Another feature takes place when ignoring residual interaction; valence nucleons are lumped together into subsystems of tightly bound particles (clustering).

The subject of clustering cuts across many areas of science extending from clusters of galaxies to micro-organisms. Etymologically, cluster refers to a group of similar things that are close together. In nuclear physics, there is a strong relationship between nucleon-nucleon correlations and the complexity of the nuclear system. This determines a spatial arrangement of the nucleons in bound sub-units denoted by cluster constituents and which are key aspects of the nuclear environment. The clustering phenomenon is actually one of the oldest models describing nuclear structure. Its essence is drawn back from the birth of nuclear physics after the discovery of natural radioactivity. The unknown radiations,  $\alpha$ ,  $\beta$ , and  $\gamma$  are observed from radioactive sources by Pierre and Marie Curie and which later will be known as helium, positron or electron and photon. In 1911, Rutherford suggested a nuclear model in which nucleus occupies only a very small volume taken up by the atom after an experiment involving the scattering of  $\alpha$ -particles from heavy element such as gold, silver and copper [4].

Cluster phenomena had been predicted from the early 1930's. It has been shown that the short range interaction between individual groups of nucleons is described by partial wave functions, constructed out of "resonating group structure" [5]. Later, in heavy nuclei, fragments close to doubly magic  $^{208}\text{Pb}$  and resulting from highly asymmetric fission were reported [6]. These are consequences of shell effects generated in the fragmentation potential in which one of the two nuclei being a spherical nucleus. The emission of heavy clusters such that  $^{14}\text{C}$  from  $^{223}\text{Ra}$  and  $^{222-226}\text{Ra}$  are observed, from experiments carried out by individual groups [7–11]. Then followed numerous theoretical approaches to investigate these new types of emissions named "cluster radioactivity" or "heavy-ion radioactivity", including  $\alpha$  emission [12–17]. Other exotic radioactive decay modes of elements such as  $^{20}\text{O}$ ,  $^{24}\text{Ne}$ ,  $^{28}\text{Mg}$ ,  $^{34}\text{Si}$  have been detected as reported by Barwich *et al.* [18], Price *et al.* [19] and Audi *et al.* [20]. These reveal the evidence of clustering in atomic nuclei. Thus, a cluster is a light nucleus, which can be viewed as being emitted from a parent nucleus as stated by Lova *et al* [21]. Cluster structures have been observed as states near the corresponding decay threshold [22, 23].

Nuclear clustering has its origin in the nucleon-nucleon effective interaction. However, the describing mechanism that leads to the formation of those sub-units is not well understood. This mechanism is, however related to the theory of quantum fragmentation [24], and goes beyond the scope of our investigation. In particular, the depth of the confining potential is essential to track the

manifestation of nuclear clustering which represents a good indication of the cluster density. This includes the level spacings between single-nucleon orbitals in deformed nuclei and its localized wave functions.

Although, for a given nucleus, experimental signatures of clustering are generally not straightforward, the break up of nuclei allow us to observe these cluster structures. Quasi-bound states are investigated through scattering of one cluster on another, such as the  $^{12}\text{C}+^{12}\text{C}$  di-nuclear system [25, 26]. Clustering phenomena represent a basic characteristic which describes the dynamics of many-nucleon system within the nuclear mean-field. A common microscopic understanding of the cluster's dynamics relies on a global description that encloses both cluster states and quantum liquid drop models in light and heavy nuclei [27–30]. The required degrees of freedom for a realistic cluster configuration are orientation (rotation-oscillation) and deformation (vibrations) which make the cluster model mimic other existing models such as nuclear collective models (rotational, vibrational,...). Cluster states are seldom found in the nuclear ground state, but rather in highly excited states [31] and specifically alpha- and exotic-conjugate nuclei [25, 32–34]

The formation of a cluster is favoured by the decay threshold and its closeness to nuclear deformations known as collective excitations. Therefore, at the threshold, cluster states belong to an open quantum system. This explains the relationship between states related to particle-emission, and the vicinity of scattering states. The strong selective excitation in alpha-transfer reactions, the rotational band patterns, transitional strengths and enhanced electromagnetic moments, including the width of resonant states above the threshold observed during experiment, are good indications of cluster states within nuclei, as explained in [35].

The clustering phenomenon proves its merits in describing nuclear spectroscopy when correlation is so strong and the well-developed cluster structure is realized. Indeed, the relative motion between clusters becomes a fundamental mode of the nucleus motion. The spacial localization of clusters and their relative motion give us a clear concept of the well developed cluster structure [25].

Nevertheless, much work have been done to probe the spectroscopy of nuclear systems using cluster structures. The bound states and single particle resonances of the cluster-core potential which describes the properties of nuclei can be well understood using the cluster states. It was shown that rotational bands present quite a significant degree of alpha-cluster structure in light nuclei [36]. In refs. [37–40], a preformed alpha cluster can be emitted from a parent nucleus, confirming the existence of such a particle which moves into different orbits with respect to the core. In the actinide region, features of the ground state rotational band such as exotic decay lifetimes, spectra of



low-lying states (positive parity) and electromagnetic decay rates (enhanced E2 transition rates), are well reproduced using cluster models [29, 35, 41–48]. The actual superdeformed band and normal deformed ground states in  $^{60}\text{Zn}$  have been probed by treating it as  $^{56}\text{Ni}+\alpha$  and  $^{32}\text{S}+^{28}\text{Si}$  cluster structures [45]. These models have been widely used to investigate nuclear spectroscopy such as molecular states (strong deformations), resonances describing unbound nuclei, beta-decay, and exotic and halo nuclei.

Overall, in studies that were carried out so far in accordance with the methods and references listed therein, the nuclear potentials, central keys of structures and scattering observables used, were either the phenomenological (Saxon-Woods [49] and Saxon-Woods Cubed [41, 43–46]) or the double folded potential with M3Y (Michigan three Yukawa), nucleon-nucleon interaction and its density dependent versions including the zero-range pseudo-potential which account for exchange contribution, [22, 23, 50–54]. However, the double folding model with M3Y inter-nucleon interaction that was constructed to investigate properties of the surface region, such as the decay half life, the width and scattering, failed to reproduce the ground state band of low-lying states and resulting in inverted or compressed spectra in a number of nuclei. Recently, Ibrahim *et al.* [55–57], developed a hybrid potential of the Saxon-Woods plus Saxon-Woods cubed type to remediate the ambiguity due to the folding model in the interior region. This local form obtained with parameters fitting at the surface of the M3Y effective interaction gave, excellent results for the spectroscopy of even-even heavy nuclei, consistent with available experimental data.

In this thesis, an attempt to describe cluster structure microscopically using Binary Cluster Model (BCM) [27], will lead us to outline different potential models, from microscopic to the phenomenological hybrid type as discussed above. The M3Y and the later developed realistic interaction in 1983, CEG83 (Complex Effective Gaussian form factor) , [58] are used to construct the double folded cluster-core potential. Extension to relativistic mean-field approximation treatment (RMFT) and widely known Relativistic Love-Franey parametrization of the nucleon-nucleon amplitude [59, 60] will be discussed and in more details in order to compare with their non-relativistic counterparts.

It was shown that the spectroscopy of low-lying states (energy, parity, spin, wave function,...), and low-energy reactions are well described with cluster model [61], where antisymmetrization effects are expected to be very significant. Then, our cluster model will treat consistently the exchange effects of the nucleon-nucleon interaction.

In chapter 2, we emphasize the choice of binary cluster models relying on certain criteria. We number the different cluster-core configurations to be tested

in our model. The basic structure observables of interest will be discussed as probes to cluster states within nuclei.

In chapter 3, which is the main body of this thesis, we will discuss and compare different potential models transcending from phenomenological to microscopic. We shall adopt the multiple scattering formalism to construct the microscopic cluster-core potentials. We will give consistent arguments on different nucleon-nucleon effective interactions used in this thesis. The relativistic mean field approach which described the ground state properties of many nuclei is discussed.

Chapter 4, is devoted to the numerical discussions obtained from the three potential models. We compare their results and draw conclusions on their advantages and shortcomings and construct a hybrid potential. In chapter 5, we give conclusions and the future directions of our project.

## Chapter 2

# Binary Cluster Model and Structure Observables

### 2.1 Introduction

Cluster models are constructed on the basis of effects observed in nuclei where cluster structures can be prominent. Hence, as a model, in the cluster approximation, the A-nucleons system whose dynamics is described by the Schrödinger Hamiltonian

$$\hat{H} = \sum_{i=1}^A \frac{\mathbf{P}_i^2}{2m_N} + \sum_{i<j}^A V_{NN}(\mathbf{r}_i - \mathbf{r}_j) \quad (2.1.1)$$

where  $m_N$  is the nucleon mass,  $p_i$  and  $r_i$  are the momentum and space coordinate of nucleon  $i$ , and  $V_{NN}$  a nucleon-nucleon interaction is assumed to be partitioned into clusters. We adopt the simplest model; the binary cluster model of Buck *et al* [41] in which we consider the parent nucleus as a dinuclear system consisting of two touching nuclei and keeping their individuality. The relative motion between the two nuclei gives rise to quasi-bound states or molecular resonances in the internuclear potential, and their decay process. This collective motion governs the dynamics of the cluster-core system and represents its main degree of motion.

### 2.2 Cluster-Core Configuration

Alpha and exotic emissions (massive ejectile) are common modes of decays in the actinide region. These easily assign an appropriate mass and charge to describe the cluster-core system. Therefore, the two fragments should be single or doubly magic and even-even to prevent any internal break-up. This is a requirement, since the nucleus will prefer a nuclear state involving the tightly bound cluster-core system. Basically, a large binding energy ensures a great stability for the cluster-core system. We follow the method developed

in refs. [27, 29, 30]. This approach states that, the likely decomposition of a nucleus with charge and mass  $(Z_T, A_T)$  into a core  $(Z_1, A_1)$  and a cluster  $(Z_2, A_2)$  can be obtained from the local maximum of the quantity

$$D(Z_1, A_1, Z_2, A_2) = \sum_{i=1}^2 \left[ B_A(Z_i, A_i) - B_L(Z_i, A_i) \right] \quad (2.2.1)$$

defining the sum of the difference between  $B_A(Z_i, A_i)$  corresponding to the binding energy for each fragment of charge and mass  $(Z_i, A_i)$  with  $i = 1, 2$ , in the unit of MeV and obtained from nuclear mass spectroscopy and the term  $B_L(Z_i, A_i)$  defined below,

$$B_L(Z_i, A_i) = \sum_{j=v}^p f_j(A_i, Z_i), \quad (2.2.2)$$

containing all the various terms that constitute the semi-empirical mass formula (SEMF), firstly written down by Weizsäcker in 1935. The most significant term is the *volume* term, which explains the effect of saturation in nuclear medium,

$$f_v(Z_i, A_i) = a_v A_i. \quad (2.2.3)$$

The second is the *surface* term which corrects the *volume* term. This term is due to nucleons at the surface that experience less attraction compared to nucleons further inside,

$$f_s(Z_i, A_i) = -a_s A_i^{\frac{2}{3}}. \quad (2.2.4)$$

The third term, the *coulomb* term accounts for the energy of protons in the nucleus repelling each other,

$$f_c(Z_i, A_i) = -a_c \frac{Z_i(Z_i - 1)}{A_i^{\frac{1}{3}}}. \quad (2.2.5)$$

The fourth, the *asymmetry* term is purely quantum mechanical arising from Pauli exclusion. It shows the tendency observed for symmetric nuclear matter ( $Z = N$ ),

$$f_a(Z_i, A_i) = -a_a \frac{(A_i - 2Z_i)^2}{A_i}. \quad (2.2.6)$$

The last, *pairing* term, which corrects the omission of nuclear internal spin and shell effects is given by:

$$f_p(Z_i, A_i) = \delta(A_i) \quad (2.2.7)$$

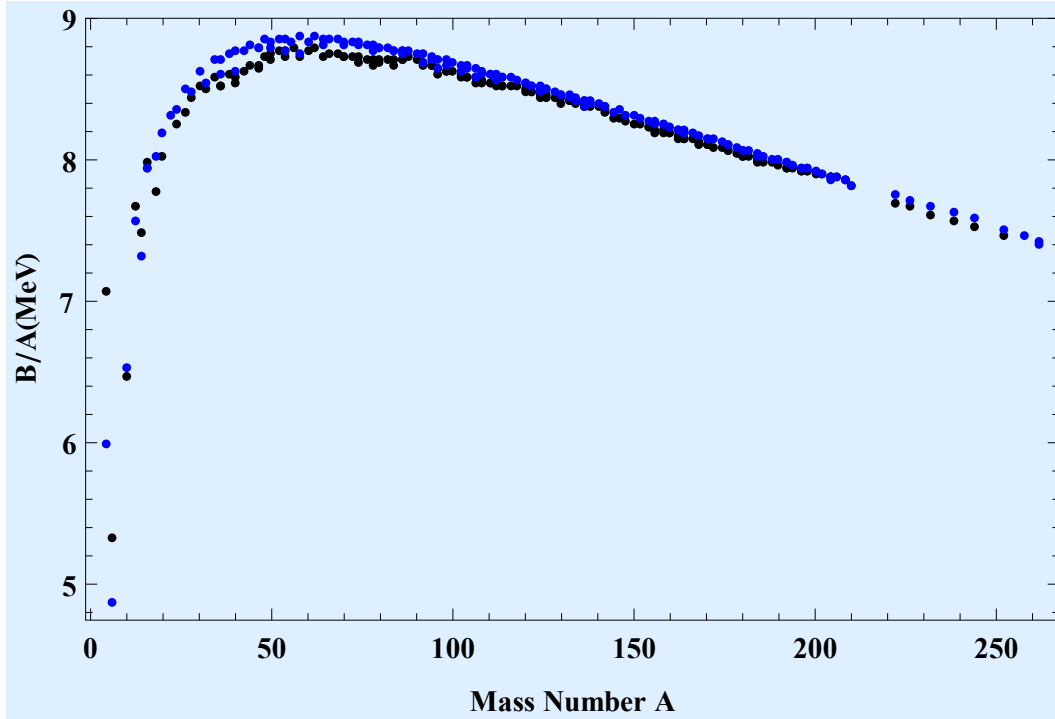


**Figure 2.1:** Fit to binding energy data (shown as blue dot) with mathematica package for stable even  $A$  nuclei using the liquid drop model with coefficients given in the text, the predictions (actual binding energy) are shown as black dot. Notice the strong deviations at the magic numbers.

where

$$\delta(A_i) = \begin{cases} a_p A_i^{-\frac{1}{3}}, & \text{if } Z_i, N_i \text{ even} \\ -a_p A_i^{-\frac{1}{3}}, & \text{if } Z_i, N_i \text{ odd} \\ 0, & \text{if } Z_i, N_i \text{ even-odd or odd-even} \end{cases} \quad (2.2.8)$$

The coefficients  $a_v, a_s, a_c, a_a, a_p$  are evaluated with the use of information about the binding energies of the nuclei. For specific values of  $a_v, a_s, a_c, a_a, a_p$  used in ref. [62], the plot in figure 2.1 shows the deviation of spectroscopic binding energies from those calculated with the liquid drop model.

There is an extra input that comes from experimental observation, a weak electric dipole transition in heavy which results from the strong neutron-proton force causing the centres of charge and mass to coincide in the nucleus. For a spinless final state, this yields the non-dipole constraint

$$\frac{Z_1}{A_1} = \frac{Z_2}{A_2} = \frac{Z_T}{A_T} \quad (2.2.9)$$

and

$$\frac{N_1}{A_1} = \frac{N_2}{A_2} = \frac{N_T}{A_T}. \quad (2.2.10)$$

However, no single choice of cluster-core configuration satisfies this condition. Nevertheless, we consider a nucleus as a superposition of neighbouring isotopes or isotones made of four fragments such as

$$(Z_T, A_T) \longrightarrow (Z_1, A_1), (Z_2, A_2), (Z_1 - 2, A_1), (Z_2 + 2, A_2).$$

For each specific even cluster charge,  $Z_2 = 2, 4, 6, 8, 10, 12, 14, 16, 18, \dots$ , we deduce the corresponding mass  $A_2$  such as

$$\frac{A_2}{Z_2} \leq \frac{A_T}{Z_T} \leq \frac{(A_2 + 2)}{Z_2}. \quad (2.2.11)$$

We assign the probabilities  $P(A_2)$  and  $P(A_2 + 2)$  to the two isotopic masses so that the dipole constraint is fulfilled,

$$P(A_2) + P(A_2 + 2) = 1 \quad (2.2.12)$$

and

$$P(A_2) \left( \frac{Z_2}{A_2} \right) + P(A_2 + 2) \left( \frac{Z_2}{A_2 + 2} \right) = \frac{Z_T}{A_T}. \quad (2.2.13)$$

The mean cluster mass and neutron numbers can be calculated as follow,

$$\bar{A}_2 = \frac{A_T Z_2}{Z_T} \quad (2.2.14)$$

and

$$\bar{N}_2 = \frac{N_T Z_2}{Z_T}. \quad (2.2.15)$$

It is now possible to calculate the mean deviations or weighted average  $\bar{D}(1, 2) = \bar{D}(Z_1, A_1, Z_2, A_2)$  according to

$$\begin{aligned} \bar{D}(Z_1, A_1, Z_2, A_2) &= P(A_2) D(Z_1, A_1, Z_2, A_2) \\ &+ P(A_2 + 2) D(Z_1, A_1 - 2, Z_2, A_2 + 2). \end{aligned} \quad (2.2.16)$$

For adjacent cluster isotones, the fragmentation of total charge and mass number

$(Z_T, A_T) \longrightarrow (Z_1, A_1), (Z_2, A_2), (Z_1 - 2, A_1 - 2), (Z_2 + 2, A_2 + 2)$  is done by taking each even cluster neutron number

$N_2 = 4, 6, 8, 10, 12, 14, 16, 18, 20, 22, 24, 26, 28, 30, 32$ ; and find the corresponding mass  $A_2$  such as

$$\frac{A_2}{N_2} \leq \frac{A_T}{N_T} \leq \frac{(A_2 + 2)}{N_2}. \quad (2.2.17)$$

We then assign the probabilities  $P(A_2)$  and  $P(A_2 + 2)$  to each cluster isotone, yielding

$$P(A_2) + P(A_2 + 2) = 1 \quad (2.2.18)$$

and

$$P(A_2) \left( \frac{N_2}{A_2} \right) + P(A_2 + 2) \left( \frac{N_2}{A_2 + 2} \right) = \frac{N_T}{A_T}. \quad (2.2.19)$$

The mean cluster mass and charge are given so that the dipole condition is satisfied,

$$\bar{A}_2 = \frac{A_T N_2}{N_T} \quad (2.2.20)$$

and

$$\bar{Z}_2 = \frac{Z_T N_2}{N_T}. \quad (2.2.21)$$

The mean deviation or weighted average can be calculated as

$$\begin{aligned} \bar{D}(Z_1, A_1, Z_2, A_2) &= P(A_2) D(Z_1, A_1, Z_2, A_2) \\ &+ P(A_2 + 2) D(Z_1 - 2, A_1 - 2, Z_2 + 2, A_2 + 2). \end{aligned} \quad (2.2.22)$$

A subsequent way is to obtain a continuous function  $\bar{D}(Z_1, A_1, Z_2, A_2)$  for arbitrary values of  $\bar{Z}_2$ . In this case, the nucleus is composed of mixtures of four neighbouring isotope and isotone core-cluster systems. By selecting any arbitrary mean charge number  $\bar{Z}_2$  ranging from  $Z_2 = 2$  to  $Z_2 = 18$  for our choice, we ensure that the correct mean neutron number satisfying the dipole constraint is given by

$$\bar{N}_2 = \frac{N_T \bar{Z}_2}{Z_T}. \quad (2.2.23)$$

The well known values of  $\bar{Z}_2$  and  $\bar{N}_2$  allow us to find the four cluster nuclei  $(Z_2 - 2, N_2 - 2)$ ,  $(Z_2 - 2, N_2)$ ,  $(Z_2, N_2 - 2)$  and  $(Z_2, N_2)$ . The cluster charge

and neutron numbers bracket the mean values,

$$\begin{aligned} Z_2 - 2 &\leq \bar{Z}_2 \leq Z_2 \\ N_2 - 2 &\leq \bar{N}_2 \leq N_2 \end{aligned} \quad (2.2.24)$$

The weighted probabilities assigned to each cluster are expressed by

$$\begin{aligned} P(Z_2) &= \frac{1}{2} [\bar{Z}_2 - (Z_2 - 2)] \\ P(Z_2 - 2) &= \frac{1}{2} [Z_2 - \bar{Z}_2] \\ P(N_2) &= \frac{1}{2} [\bar{N}_2 - (N_2 - 2)] \\ P(N_2 - 2) &= \frac{1}{2} [N_2 - \bar{N}_2] \end{aligned} \quad (2.2.25)$$

We then obtain the average deviation  $\bar{D}(\bar{Z}_1, \bar{N}_1, \bar{Z}_2, \bar{N}_2)$  by writing

$$\bar{D}(\bar{Z}_1, \bar{N}_1, \bar{Z}_2, \bar{N}_2) = \sum_{i,j=0}^1 P(Z_2-2i)P(N_2-2j)D(Z_1+2i, N_1+2j, Z_2-2i, N_2-2j). \quad (2.2.26)$$

**Table 2.1:** Different cluster partitions used in our models

Cluster partitions	Probabilities	Q-values (MeV)
$^{212}\text{Po} \longrightarrow {}^4_2\text{He} + {}^{208}_{82}\text{Pb}$	1	8.985
$^{218}\text{Rn} \longrightarrow {}^{10}_4\text{Be} + {}^{208}_{82}\text{Pb}$	1	14.36
$^{222}\text{Ra} \longrightarrow {}^{14}_6\text{C} + {}^{208}_{82}\text{Pb}$	0.5733	33.050
$^{228}\text{Th} \longrightarrow {}^{20}_8\text{O} + {}^{208}_{82}\text{Pb}$	0.38	44.723

With this approach, our primary interest is directed to double-magic core and cluster nuclei. And especially the trans-Pb system as listed in Table 2.1 obtained from Erasmus [62], except for  $(^{212}\text{Po} \rightarrow {}^4_2\text{He} + {}^{208}_{82}\text{Pb})$  and  $(^{218}\text{Rn} \rightarrow {}^{10}_4\text{Be} + {}^{208}_{82}\text{Pb})$  configurations with pre-formation probabilities to be equal one, as mentioned in ref [63].



### 2.2.1 Cluster-Core Potential

We have a spherically symmetric system in which we consider the cluster and core in their respective ground states, interacting through an effective central potential  $V(r)$ . This interaction is the sum of local nuclear,  $U(r)$ , Coulomb,  $U_C(r)$  and the repulsive or centrifugal  $U_L(r)$  potentials, such as

$$V(r) = U_N(r) + U_C(r) + U_L(r). \quad (2.2.27)$$

The Coulomb potential accounts for interaction between the cluster charge  $Z_2$ , and a uniformly spherically charged core  $Z_1$  with radius  $R_c$ ,

$$\begin{aligned} U_C(r) &= \frac{Z_1 Z_2 e^2}{r}, & \text{if } r \geq R_c \\ &= \frac{Z_1 Z_2 e^2}{2R_c} \left( 3 - \left| \frac{r}{R_c} \right|^2 \right), & \text{if } r \leq R_c. \end{aligned} \quad (2.2.28)$$

The Coulomb radius  $R_c$  is taken as nuclear potential radius  $R_0$  in order to minimize the number of free parameters [64].

The centrifugal potential, also called the rotational energy barrier, is associated with the orbital quantum number  $L$ , given by

$$U_L(r) = \frac{L(L+1)\hbar^2}{2\mu r^2} \quad (2.2.29)$$

where  $\mu = A_1 A_2 / (A_1 + A_2)$  is the reduced mass of the system. The modified form of the centrifugal potential is given by the Langer form which takes into account the contribution from  $L = 0$ . That is,

$$U_L(r) = \frac{(L + 1/2)^2 \hbar^2}{2\mu r^2}. \quad (2.2.30)$$

For the local nuclear interaction,  $U(r)$ , a complete description of different potential models are discussed in chapter 3. Since both cluster and core have spin zero, there is no additional non-central forces arising from either spin-orbit coupling or tensor forces.

### 2.2.2 Cluster-Core Global Quantum Number

Once we have configured our cluster-core system and decided on which interacting potential to use, we next need to specify a global quantum number for the relative motion. As the Wildermuth condition [65] stated, the energetically favoured correlation between nucleons that build up the cluster structure

can only be located near the surface of the Fermi sea belonging to the core (Pauli Exclusion Principle). This condition yields an appropriate choice for the global quantum number  $G$ , such as

$$G = 2n + L = \sum_{i=1}^{n_c} (2n_i + l_i) - \bar{g}. \quad (2.2.31)$$

$n$  and  $L$  are the number of nodes and the orbital angular momentum characterizing the orbit.  $n_c$ , corresponds to the number of nucleons in the cluster. The quantum numbers,  $n_i$  and  $l_i$  are the corresponding filling of the shell-model orbitals above the closed core.  $\bar{g}$  is associated with the shell model cluster's ground state structure [44]. This condition is valid if we were describing the cluster and core nucleon orbitals by harmonic oscillator wave functions, with a common length parameter. Hence, the generated bands of states are well described by their common value of  $G$ . Even values of  $G$  correspond to low-lying positive parity states of orbital angular momentum  $L^\pi = 0^+, 2^+, 4^+, \dots, G^+$ , while odd  $G$  gives the low-lying negative parity states with orbital angular momentum  $L^\pi = 1^-, 3^-, 5^-, \dots, G^-$ . In our calculations, we will also use the approximate values of  $G$  given by Buck *et al.* [27].

### 2.3 Decay Half-Life and Width

The clear manifestation of cluster states in nuclei is seen through their decay modes beyond the threshold for alpha-particle or exotic decays (heavier clusters). This requires a preformed cluster feeling a strong nuclear force within the parent nucleus. Once reached the edge, it can tunnel through the coulomb barrier. There are phenomenological and microscopic descriptions of the decay process. Our approach is geared to the simplest phenomenological formalism developed by Gamow and the extended quasi-classical approximation of Gurvitz and Kalb ermann [66, 67]. In the following, we shall rather underline only global results of measurable observables of interest in our description of the cluster model than developing a detailed mathematical framework.

We start by first elaborating on the laws of conservation that govern this process. Consider a decaying nuclear reaction



where  $X$ ,  $X'$  and  $Y$  represent respectively, the parent, daughter and ejected particles. From the laws of conservation of total energy, we define the reaction  $Q$ -value, which is the amount of energy carried away by the two fragments, as

$$Q = (M_X - M_{X'} - M_Y)c^2 = T_{X'} + T_Y \quad (2.3.2)$$

where we have assumed the parent nucleus at rest.  $T_{X'}$  and  $T_Y$  are the daughter and ejectile kinetic energies defined as

$$T_{X'} = \frac{p^2}{2M_{X'}}, \quad T_Y = \frac{p^2}{2M_Y}, \quad (2.3.3)$$

with  $p$  the momentum calculated in the centre of mass of the decay and  $M_i$ , their nuclear mass. Then from equation 2.3.2, we deduce the relation with the Q-value

$$Q = T_Y \left( 1 + \frac{M_Y}{M_{X'}} \right) \quad (2.3.4)$$

or rewritten as

$$T_Y = Q \left( \frac{M_X - M_Y}{M_X} \right). \quad (2.3.5)$$

Since the decay remains essentially a Coulomb barrier problem, there is an additional shielding correction energy due to electrons surrounding the nucleus [68],

$$E_Z = 32.6Z_2(Z_T)^{7/5}10^{-6}\text{MeV}. \quad (2.3.6)$$

Then for the ground state decay where  $T_Y$  is unknown, the Q-value can be calculated either from the binding energies of particles, (first equality in equation 2.3.2) or from the kinetic energy coming from the recoil and the electron shielding corrections in the case of an alpha particle;

$$Q_\alpha = \frac{A_T}{A_T - A_\alpha} T_Y + 32.6Z_2(Z_T)^{7/5}10^{-6}\text{MeV}. \quad (2.3.7)$$

We assumed the same mass for the proton and the neutron. But for heavier clusters than alpha, we use instead the effective Q-value [68], with electron shielding correction given by

$$Q_{eff} = Q + 32.6Z_2(Z_T)^{7/5}10^{-6}\text{MeV}. \quad (2.3.8)$$

Spontaneous emission implies a positive value of Q, from the energetics point of view.

We should note that the angular momentum of the ejected particle coming from the rotational potential energy

$$U_L(r) = \frac{L(L+1)\hbar^2}{2\mu r^2}$$

results in a thicker and higher barrier that the particle has to overcome. For a spin zero ejectile, the conservation of angular momentum and parity gives rise to certain constraints on the decay process. For even-even nuclei, as in our cluster model, we have a favoured decay with no change of the angular momentum and parity for the parent and daughter nuclei. The allowed values

of  $J^\pi$  of the daughter nucleus are  $0^+$  ( $L=0$ ),  $1^-$  ( $L=1$ ),  $2^+$  ( $L=2$ ), and so forth, for spin  $J^\pi = 0^+$  of the parent nucleus.

The most important quantity calculated during the break up of a given nucleus into a cluster and a core is the decay width denoted by  $\Gamma$ . This quantity, in a quasi-classical approximation [38, 39, 66, 67], is expressed as

$$\Gamma = PF \frac{\hbar^2}{2\mu} \exp \left[ -2 \int_{r_2}^{r_3} k(r) dr \right]. \quad (2.3.9)$$

Here  $P$  is the preformed cluster-core probability inside the parent nucleus. The normalization factor  $F$ , such that

$$F \int_{r_1}^{r_2} dr \frac{1}{k(r)} \cos^2 \left( \int_{r_1}^r dr' k(r') - \frac{\pi}{4} \right) = 1 \quad (2.3.10)$$

is usually written as

$$F \int_{r_1}^{r_2} \frac{dr}{2k(r)} = 1 \quad (2.3.11)$$

where we have replaced the squared cosine term by  $1/2$  without any loss of accuracy.  $r_1$ ,  $r_2$  and  $r_3$  are three classical turning points in order of increasing distance from the origin, as illustrated in figure 2.2. For the ground state decay, their values are determined by solving numerically the equation  $V(r)=Q$ . The local wave number  $k(r)$  is defined as

$$k(r) = \sqrt{\frac{2\mu}{\hbar^2} |Q - V(r)|}. \quad (2.3.12)$$

To this end, the decay half-life  $T_{1/2}$ , defining the necessary time taken to halve a number of nuclei, is given by

$$T_{1/2} = \frac{\hbar \ln 2}{\Gamma}. \quad (2.3.13)$$

The half-life estimations are also done by using the universal formula for the cluster decay, also called the phenomenological law of Viola and Seaborg [69], such that

$$\log_{10} T_{1/2}(s) = \frac{a(Z_1 + Z_2) - b}{\sqrt{Q}} - (c(Z_1 + Z_2) + d) + h_{\log} \quad (2.3.14)$$

where  $a=1.66175$ ,  $b=8.5166$ ,  $c=0.20228$ ,  $d=33.9069$  and

$$h_{\log} = \begin{cases} 0, & \text{if } Z_i, N_i \text{ even} \\ -0.772, & \text{if } Z_i, N_i \text{ odd} \\ 0, & \text{if } Z_i, N_i \text{ even-odd or odd-even} \end{cases} \quad (2.3.15)$$

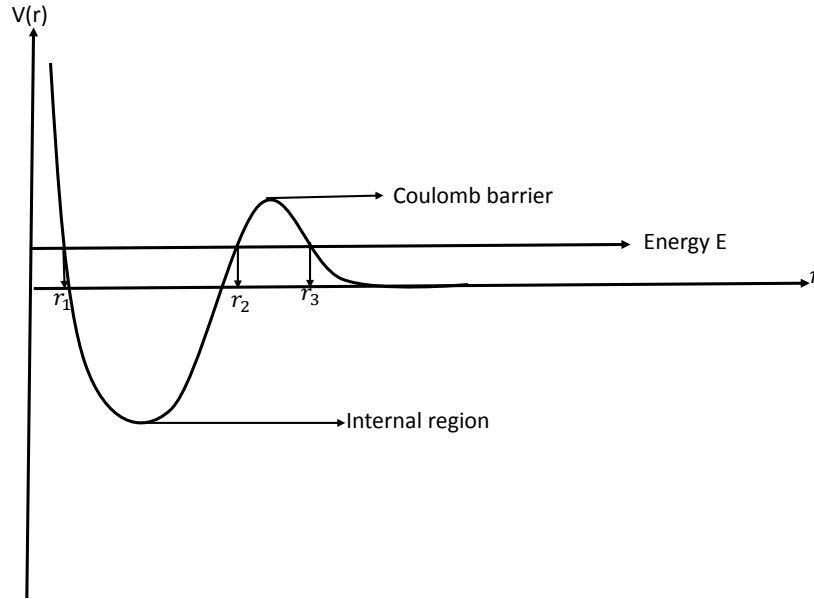


**Figure 2.2:** Central effective potential versus cluster-core relative position  $r$ . The three classical turning points are illustrated for a specific given state energy  $E$ .

## 2.4 Level Structures and Electromagnetic Transitions

The energy spectrum obtained with cluster models seems to follow a rotational pattern. But this does not mean evidently that the cluster and rotational models carry the same internal configuration. It was shown that, the cluster phenomenon is associated with large intrinsic deformation which results in a very enhanced quadrupole moment. These deformations are related to the electromagnetic transitions between cluster or super-deformed states in heavy nuclei [45]. These evidences secure the entire basis of the cluster model.

### 2.4.1 The Bohr-Sommerfeld and Wentzel-Kramers-Brillouin Rules

Consider a radial Schrödinger equation

$$\frac{-\hbar^2}{2m} \frac{d^2\psi(r)}{dr^2} + (V(r) - E)\psi(r) = 0 \quad (2.4.1)$$

where the wave function solution is written in terms of an arbitrary function  $S(r)$  as

$$\psi(r) = \exp(iS(r)/\hbar). \quad (2.4.2)$$

Equation 2.4.1, can be expressed as

$$S'^2(r) = 2m(E - V(r)) + i\hbar S''(r). \quad (2.4.3)$$

We then expand  $S(r)$  in powers of  $\hbar$ :

$$S(r) = S_0(r) + \frac{\hbar}{i} S_1(r) + \frac{\hbar^2}{i^2} S_2(r) + \dots \quad (2.4.4)$$

Followed by substitution into equation 2.4.3 and equating terms that have the same power by taking only terms up to  $\hbar^1$ , we obtain

$$S_0'^2(r) = 2m(E - V(r)) \quad (2.4.5)$$

and

$$2S_0'(r)S_1'(r) + S_0''(r) = 0. \quad (2.4.6)$$

Two cases are considered when solving these equations:

The classical allowed region:  $V(r) < E$  implying

$$S_0(r) = \pm \int_{r_0}^r dr' p(r') \quad (2.4.7)$$

and

$$S_1(r) = -\frac{1}{2} \log S_0'(r) + c \quad (2.4.8)$$

where we have introduced

$$p(r) = \sqrt{2m(E - V(r))} \quad (2.4.9)$$

and the constant  $c$ .

Then, the general solution is given by

$$\psi(r) = \frac{a_+}{p(r)} \exp \left[ \frac{i}{\hbar} \int_{r_0}^r dr' p(r') \right] + \frac{a_-}{p(r)} \exp \left[ -\frac{i}{\hbar} \int_{r_0}^r dr' p(r') \right]. \quad (2.4.10)$$

The classical forbidden region:  $V(r) > E$ , the general solution is written as

$$\phi(r) = \frac{b_+}{q(r)} \exp \left[ \frac{1}{\hbar} \int_{r_0}^r dr' q(r') \right] + \frac{b_-}{q(r)} \exp \left[ -\frac{1}{\hbar} \int_{r_0}^r dr' q(r') \right]. \quad (2.4.11)$$

Likewise, we have defined

$$q(r) = \sqrt{2m(V(r) - E)}. \quad (2.4.12)$$

Here  $a_{\pm}$  and  $b_{\pm}$  are constants and  $r_0$  is an arbitrary point. Note that, there is a point such that  $V(\bar{r}) = E$ , called the classical turning point where classically the particle stops and turns back in the opposite direction. The Wentzel-Kramer-Brillouin (WKB) is proven to be valid if the variation of the potential over a distance of the size of the de Broglie wavelength,  $\lambda_0(r) = 2\pi\hbar/p(r)$ , has to be small with respect to the kinetic energy of the particle. That is

$$\lambda_0(r) \frac{dV(r)}{dr} \ll \frac{p^2(r)}{2m} \quad (2.4.13)$$

otherwise, it will not hold since this relation breaks down at the turning point where  $p(r) = 0$ .

We then examine different possibilities, where we have a case of the potential barrier on the left of figure 2.3 with a turning  $r_1$  point such that

$$\begin{aligned} E < V(r) & \quad \text{for} \quad r < r_1 \\ E > V(r) & \quad \text{for} \quad r > r_1 \end{aligned} \quad (2.4.14)$$

Since the WKB is invalid at the turning point  $r_1$ , we expand to first order the potential  $V(r)$  near  $r_1$  in order to solve the stationary equation 2.4.1;

$$E - V(r) = E - V(r_1) - (r - r_1)V'(r). \quad (2.4.15)$$

Then, the equation 2.4.1 becomes,

$$\frac{d^2\psi(r)}{dt^2} + t\psi(r) = 0 \quad (2.4.16)$$

where

$$t = \left( \frac{2m}{\hbar^2 a_1} \right)^{1/3} (r - r_1), \quad a_1 = -V'(r). \quad (2.4.17)$$

The solution of this equation is expressed as a linear combination of Bessel functions,

$$\begin{aligned} \psi(r) &= \frac{A}{\sqrt{p(r)}} \sqrt{y} J_{1/3}(y) + \frac{B}{\sqrt{p(r)}} \sqrt{y} J_{-1/3}(y) \quad \text{for} \quad r > r_1 \\ \psi(r) &= \frac{C}{\sqrt{q(r)}} \sqrt{y} I_{1/3}(y) + \frac{D}{\sqrt{q(r)}} \sqrt{y} I_{-1/3}(y) \quad \text{for} \quad r < r_1 \end{aligned} \quad (2.4.18)$$

Applying the asymptotic form of Bessel function such that,

$$J_{\pm 1/3}(y) \rightarrow \begin{cases} \left( \frac{y}{2} \right)^{\pm 1/3} \frac{1}{\Gamma(1 \pm 1/3)} & y \rightarrow 0 \\ \left( \frac{1}{2y\pi} \right)^{1/2} \cos \left( y \mp \pi/6 - \pi/4 \right) & y \rightarrow \infty \end{cases} \quad (2.4.19)$$

$$I_{\pm 1/3}(y) \rightarrow \begin{cases} \left(\frac{y}{2}\right)^{\pm 1/3} \frac{1}{\Gamma(1 \pm 1/3)} & y \rightarrow 0 \\ \left(\frac{1}{2y\pi}\right)^{1/2} \left(e^y + e^{-y} + e^{-i(1/2 \pm 1/3)}\right) & y \rightarrow \infty \end{cases}. \quad (2.4.20)$$

thus, solutions belonging to both regions can be connected so that

$$\begin{aligned} \frac{1}{\sqrt{q(r)}} \exp\left[-\frac{1}{\hbar} \int_r^{r_1} dr' q(r')\right] &\leftrightarrow \frac{2}{\sqrt{p(r)}} \cos\left[\frac{1}{\hbar} \int_{r_1}^r dr' p(r') - \frac{\pi}{4}\right] \\ \frac{1}{\sqrt{q(r)}} \exp\left[\frac{1}{\hbar} \int_r^{r_1} dr' q(r')\right] &\leftrightarrow -\frac{2}{\sqrt{p(r)}} \sin\left[\frac{1}{\hbar} \int_{r_1}^r dr' p(r') - \frac{\pi}{4}\right] \end{aligned}. \quad (2.4.21)$$

In a similar way, if a turning point  $r_1$  is located on the right of the potential barrier such that

$$\begin{aligned} E > V(r) &\quad \text{for } r < r_1 \\ E < V(r) &\quad \text{for } r > r_1' \end{aligned}, \quad (2.4.22)$$

then the solution is expressed as,

$$\begin{aligned} \frac{2}{\sqrt{p(r)}} \cos\left[\frac{1}{\hbar} \int_r^{r_1} dr' p(r') - \frac{\pi}{4}\right] &\leftrightarrow \frac{1}{\sqrt{q(r)}} \exp\left[-\frac{1}{\hbar} \int_{r_1}^r dr' q(r')\right] \\ \frac{2}{\sqrt{p(r)}} \sin\left[\frac{1}{\hbar} \int_{r_1}^r dr' p(r') - \frac{\pi}{4}\right] &\leftrightarrow -\frac{1}{\sqrt{q(r)}} \exp\left[\frac{1}{\hbar} \int_r^{r_1} dr' q(r')\right] \end{aligned}. \quad (2.4.23)$$

These results can be used now to describe a potential given in figure 2.3 which contains two turning points  $r_1$  and  $r_2$  so that the classically allowed region is located in between  $r_1$  and  $r_2$ .

Let us situate the regions I, II and III within intervals  $]-\infty, r_1]$ ,  $]r_1, r_2]$ ,  $]r_2, \infty[$ . In region I, the asymptotic solution  $r \rightarrow -\infty$ , is

$$\psi_I(r) = C \frac{1}{\sqrt{q(r)}} \exp\left[-\frac{1}{\hbar} \int_r^{r_1} dr' q(r')\right]. \quad (2.4.24)$$

Therefore, this solution is matched in region II to

$$\psi_{II}(r) = C \frac{2}{\sqrt{p(r)}} \cos\left[\frac{1}{\hbar} \int_{r_1}^r dr' p(r') - \frac{\pi}{4}\right]. \quad (2.4.25)$$

Next, we define from equation 2.4.23,

$$\zeta = \frac{1}{\hbar} \int_{r_1}^{r_2} dr' p(r') - \frac{\pi}{2} \quad (2.4.26)$$



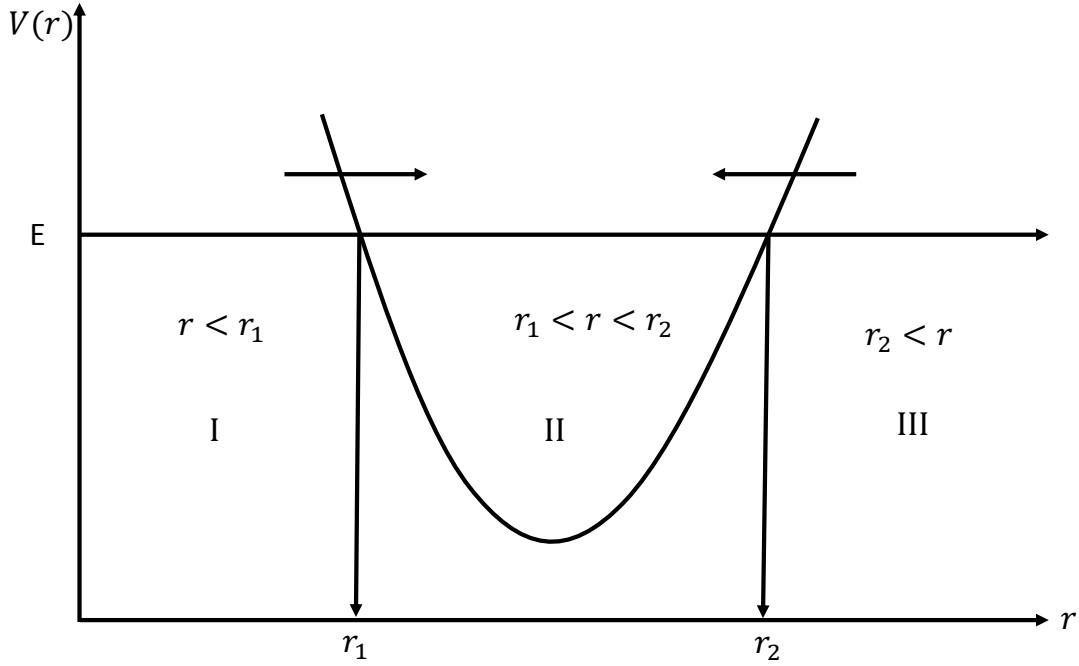


**Figure 2.3:** Central potential with localized classical turning points where arrows indicate connecting regions.

so that in region II, the solution may be written as

$$\begin{aligned}
 \psi_{II}(r) &= C \frac{2}{\sqrt{p(r)}} \cos \left[ \frac{1}{\hbar} \int_{r_1}^r dr' p(r') - \frac{\pi}{4} - \zeta \right] \\
 &= C \frac{2}{\sqrt{p(r)}} \left[ \cos \left( \frac{1}{\hbar} \int_{r_1}^r dr' p(r') - \frac{\pi}{4} \right) \cos(\zeta) \right. \\
 &\quad \left. + \sin \left( \frac{1}{\hbar} \int_{r_1}^r dr' p(r') - \frac{\pi}{4} \right) \sin(\zeta) \right].
 \end{aligned} \tag{2.4.27}$$

This last equation is now connected to the solution in region III at the second

turning point  $r_2$  to yield,

$$\psi_{III}(r) = C \frac{1}{\sqrt{q(r)}} \left[ \exp\left(-\frac{1}{\hbar} \int_{r_2}^r dr' q(r')\right) \cos(\zeta) - 2 \exp\left(\frac{1}{\hbar} \int_{r_2}^r dr' q(r')\right) \sin(\zeta) \right]. \quad (2.4.28)$$

Therefore,  $E$  is an eigenvalue if and only if

$$\sin(\zeta) = 0 \quad \text{or} \quad \zeta = n\pi, \quad (2.4.29)$$

leading to the well known Bohr-Sommerfeld Quantization Rule [70, 71],

$$\int_{r_1}^{r_2} dr \frac{p(r)}{\hbar} = (2n + 1) \frac{\pi}{2}. \quad (2.4.30)$$

So for a given potential  $V(r)$  and a known value of the quantum number  $G$ , the spectrum,  $E_L$  associated with the angular momentum  $L$ , is computed either with the quantization rule

$$\int_{r_1}^{r_2} \sqrt{\frac{2\mu}{\hbar^2} [E_L - V(r)]} dr = (2n + 1) \frac{\pi}{2} = (G - L + 1) \frac{\pi}{2} \quad (2.4.31)$$

or directly by solving the radial Schrödinger equation 2.4.1 for the quasi-bound states. Note that the energies  $E_L = Q + E_L^*$  where  $E_L^*$  are the excited energies for  $L^\pi = 0^+, 2^+, 4^+, \dots$  band states. This quantization condition also, allows to adjust the depth of the cluster-core total potential.

## 2.4.2 Transition Probability

The cluster model makes definite predictions concerning the electromagnetic properties of its constituent states. And such electromagnetic transitions involve composite single-particle clusters in our case, instead of single-particles like a proton or neutron. It is well known that excited states of nuclei usually de-excite to their ground states via spontaneous photon emission (multipole radiation) or the inverse process, absorption giving rise to *electromagnetic transitions*. Such processes are described as resulting from the interaction of the nucleus with an external electromagnetic field. These interactions are mediated by the four-potential  $(\phi, \mathbf{A})$ . The scalar potential,  $\phi$ , couples to nuclear charge  $\rho$  and the vector potential  $\mathbf{A}$ , to the nuclear current  $\mathbf{j}$ . We will not get involved in any complicated calculation, but we rather list only interesting results.

We consider a transition probability per unit time or *transition probability* in short, of gamma radiation with angular momentum  $(L, m)$  representing also the multipole moment of the radiation field. The decay occurs from an initial nuclear state  $(J_i, m_i)$  to a final nuclear state  $(J_f, m_f)$  where the sources

of the field are either electric or magnetic, denoted by an index  $\sigma = \mathbf{E}$  or  $\sigma = \mathbf{M}$ . This transition probability is calculated from time-dependent perturbation theory (*Fermi's golden rule*) [72],

$$\mathcal{W}(L; J_i \longrightarrow J_f) = \frac{8\pi(L+1) \left(\frac{E_\gamma}{\hbar c}\right)^{2L+1}}{L\hbar [(2L+1)!!]^2} \sum_{mm_f} \left| \langle J_f m_f | \mathcal{M}_{\sigma L m} | J_i m_i \rangle \right|^2. \quad (2.4.32)$$

The radiation or gamma ray energy is given by  $E_\gamma = E_i - E_f$ . The spherical tensor of rank  $L$ ,  $\mathcal{M}_{\sigma L m}$ , represents the nuclear electromagnetic transition operator.

We note that the transition conserves the angular momentum,

$$\mathbf{J}_i = \mathbf{J}_f + \mathbf{L} \quad (2.4.33)$$

and the allowed transitions are restricted to the *triangular condition*

$$|J_i - J_f| \leq L \leq J_i + J_f, \quad m_i = m_L + m_f \quad (2.4.34)$$

### 2.4.3 Reduced Transition Probability

Since magnetic substates for a given angular momentum are not accessible directly, an adequate observable turns out to be the *reduced transition probability*, defined as

$$\begin{aligned} B(\sigma L; J_i \longrightarrow J_f) &\equiv \sum_{mm_f} \left| \langle J_f m_f | \mathcal{M}_{\sigma L m} | J_i m_i \rangle \right|^2 \\ &= \frac{1}{2J_i + 1} \left| \langle J_f || \mathcal{M}_{\sigma L m} || J_i \rangle \right|^2. \end{aligned} \quad (2.4.35)$$

In the last step, we have used the *Wigner-Eckart Theorem*, and  $\langle J_f || \mathcal{M}_{\sigma L m} || J_i \rangle$  is called the *reduced matrix element* of the multipole operator  $\mathcal{M}_{\sigma L m}$ . So, the *transition probability* written above, in 2.4.32 will read

$$\mathcal{W}(L; J_i \longrightarrow J_f) = \frac{8\pi(L+1) \left(\frac{E_\gamma}{\hbar c}\right)^{2L+1}}{L\hbar [(2L+1)!!]^2} B(\sigma L; J_i \longrightarrow J_f). \quad (2.4.36)$$

With the convenient notation used for the multipole operator,

$$\mathcal{M}_{EL} = Q_L, \quad \mathcal{M}_{ML} = M_L, \quad (2.4.37)$$

we then write down the components of electric and magnetic tensors of rank  $L$  as

$$Q_{Lm} = \sum_{j=1}^A e(j) r_j^L Y_{Lm}^*(\Omega_j) \quad (2.4.38)$$

$$M_{Lm} = \frac{\mu_N}{\hbar c} \sum_{j=1}^A \left[ \frac{2}{L+1} g_l^{(j)} \mathbf{l}(j) + g_s^{(j)} \mathbf{s}(j) \right] \cdot \nabla \left[ r_j^L Y_{Lm}^*(\Omega_j) \right].$$

$e(j)$  ( $e$  for proton, 0 for neutron) is the electric charge.  $\mathbf{l}(j)$  and  $\mathbf{s}(j)$  are the orbital and spin angular momenta of nucleon  $j$ , with polar coordinates  $\Omega_j = (\theta_j, \phi_j)$ .

The spin factor  $g_s^{(j)} = (g_p = 5.586$  for proton,  $g_n = -3.826$  for neutron) and orbital factor  $g_l^{(j)} = (1$  for proton, 0 for neutron) are gyromagnetic ratios.  $\mu_N = \hbar/2m_p = 0.10515$  cefm is the nuclear magneton with  $m_p = 938.27$  MeV/ $c^2$ , the proton mass.

Therefore, we can see from equation 2.4.38 that the  $L$ -pole, electric and magnetic operators have parities,  $\pi = (-1)^L$  and  $\pi = (-1)^{L+1}$ . It follows that the *parity conservation* rule during the transition implies

$$\pi_i \pi_f = \begin{cases} (-1)^L & \text{for } Q_L, \\ (-1)^{L+1} & \text{for } M_L. \end{cases} \quad (2.4.39)$$

where  $\pi_i$  and  $\pi_f$  denote the parities of initial and final nuclear states. Hence the likeliest transition is the one with smallest multipolarity, constrained to angular momentum and parity selection rules 2.4.34 and 2.4.39.

Our model uses electric transitions as a probe to the structure of nuclear states involving multipole moments and gamma decay such that the sum in the electric tensor operator runs over the two total charges  $Z_1$  and  $Z_2$  of the core and cluster [63], as shown in figure 2.4.

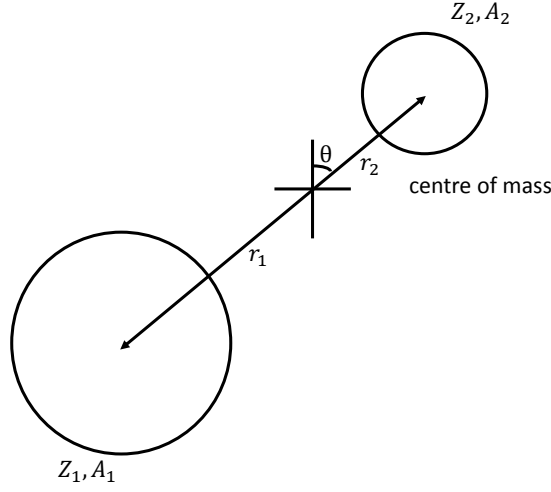


**Figure 2.4:** Coordinates representation of cluster-core relative motion

$$\begin{aligned}
 Q_{Lm} &= \sum_{j=1}^A e(j) r_j^L Y_{Lm}^*(\Omega_j) \\
 &\approx Z_1 r_1^L Y_{Lm}^*(\Omega_1) + Z_2 r_2^L Y_{Lm}^*(\Omega_2) \\
 &= Z_1 r_1^L Y_{Lm}^*(\theta_1, \phi_1) + Z_2 r_2^L Y_{Lm}^*(\theta_2, \phi_2) \\
 &= Z_1 r_1^L Y_{Lm}^*(\pi - \theta, \pi + \phi) + Z_2 r_2^L Y_{Lm}^*(\theta, \phi) \\
 &= \left[ (-1)^L Z_1 r_1^L + Z_2 r_2^L \right] Y_{Lm}^*(\theta, \phi) \\
 &= \left[ (-1)^L Z_1 \left( \frac{-A_2 r}{A} \right)^L + Z_2 \left( \frac{A_1 r}{A} \right)^L \right] Y_{Lm}^*(\theta, \phi) \\
 &= \beta_L r^L Y_{Lm}^*(\theta, \phi)
 \end{aligned} \tag{2.4.40}$$

where

$$\beta_L = \left[ Z_1 \left( \frac{-A_2}{A} \right)^L + Z_2 \left( \frac{A_1}{A} \right)^L \right]. \tag{2.4.41}$$

Furthermore our model is geared to spin zero nuclei, thus the total angular momentum,  $\mathbf{J} = \mathbf{L} + \mathbf{S}$  is reduced to the orbital angular momentum  $\mathbf{L}$ . So, the matrix element for a given  $L$ -pole electric operator is written according to

the Wigner-Eckart theorem [73],

$$\begin{aligned}
 \langle L_f m_f | \mathbf{Q}_{Lm} | L_i m_i \rangle &= \langle L_f m_f | \beta_L r^L Y_{Lm}^*(\theta, \phi) | L_i m_i \rangle \\
 &= (-1)^m \langle L_f m_f | \beta_L r^L Y_{L-m}(\theta, \phi) | L_i m_i \rangle \\
 &= \langle L_i m_i L - m | L_f m_f \rangle \langle L_f || \mathbf{Q}_L || L_i \rangle \\
 &= \frac{\hat{L}_f}{\hat{L}_i} \langle L_f m_f L m | L_i m_i \rangle \langle L_f || \mathbf{Q}_L || L_i \rangle
 \end{aligned} \tag{2.4.42}$$

with the 'hat factor',  $\hat{L} = \sqrt{2L + 1}$ .

A straightforward application of this to the reduced transition probability gives

$$\begin{aligned}
 B(EL; L_i \longrightarrow L_f) &= \sum_{mm_f} \left| \langle L_f m_f | \mathbf{Q}_{Lm} | L_i m_i \rangle \right|^2 \\
 &= \sum_{mm_f} \left( \frac{\hat{L}_f}{\hat{L}_i} \right)^2 \left| \langle L_f m_f L m | L_i m_i \rangle \right|^2 \left| \langle L_f || \mathbf{Q}_L || L_i \rangle \right|^2 \\
 &= \left( \frac{\hat{L}_f}{\hat{L}_i} \right)^2 \left| \langle L_f || \mathbf{Q}_L || L_i \rangle \right|^2,
 \end{aligned} \tag{2.4.43}$$

where we have considered the symmetry properties of the Clebsch-Gordon coefficients (CG).

Next we would like to give an evaluated expression for the reduced matrix element  $\langle L_f || \mathbf{Q}_L || L_i \rangle$ . We recall that the cluster-core initial and final nuclear states are written as:

$$|L_i m_i\rangle = \frac{\varphi_{nL_i}(r)}{r} Y_{L_i m_i}(\theta_i, \phi_i), \quad |L_f m_f\rangle = \frac{\varphi_{nL_f}(r)}{r} Y_{L_f m_f}(\theta_f, \phi_f). \tag{2.4.44}$$

According to Brink and Satchler [73], the reduced matrix element is given by

$$\langle L_f || \mathbf{Q}_L || L_i \rangle = \frac{\beta_L}{\sqrt{4\pi}} \left( \frac{\hat{L}_i \hat{L}}{\hat{L}_f} \langle L_i 0 L 0 | L_f 0 \rangle \right) \langle \varphi_{nL_f}(r) | r^L | \varphi_{nL_i}(r) \rangle \tag{2.4.45}$$

which yield the reduced transition probability

$$B(EL; L_i \longrightarrow L_f) = \frac{(\beta_L \hat{L})^2}{4\pi} \left( \langle L_i 0 L 0 | L_f 0 \rangle \right)^2 \left| \langle \varphi_{nL_f}(r) | r^L | \varphi_{nL_i}(r) \rangle \right|^2. \tag{2.4.46}$$

We can derive a convenient simple estimate approximation for the reduced transition probabilities  $B(EL; L_i \longrightarrow L_f)$ . This is possible, if we assume a constant radial wave function, inside the nucleus and zero outside. Finally,

this results in the so-called Weisskopf single-particle estimate or Weisskopf unit (W.u.) [74];

$$B_W(EL) \approx \frac{1.2^{2L}}{4\pi} \left( \frac{3}{L+3} \right)^2 A^{2L/3} e^2 f m^{2L}. \quad (2.4.47)$$

For a transition involving a given nuclear state  $L_i = L$  to the ground state  $L_f = 0$ , the reduced transition probability is,

$$B(EL; L \rightarrow 0) = \left( \frac{\beta_L}{\sqrt{4\pi}} \right)^2 \left| \int dr \varphi_{nL}^*(r) r^L \varphi_{n0}(r) \right|^2 \quad (2.4.48)$$

The state  $L = 1$ , corresponds to dipole transitions, with the reduced transition probability

$$B(E1; 1^- \rightarrow 0^+) = \left( \frac{\beta_1}{\sqrt{4\pi}} \right)^2 \left| \int dr \varphi_{n1}^*(r) r \varphi_{n0}(r) \right|^2, \quad (2.4.49)$$

which are weak for low-lying states in heavy nuclei. This gives rise to a vanishing charge factor

$$\beta_1 = \left[ Z_1 \left( \frac{-A_2}{A} \right) + Z_2 \left( \frac{A_1}{A} \right) \right] \approx 0, \quad (2.4.50)$$

leading to the dipole constraint

$$\frac{Z_1}{A_1} = \frac{Z_2}{A_2} = \frac{Z}{A}. \quad (2.4.51)$$

The state  $L = 2$ , corresponds to quadrupole transitions between positive parity low-lying states, where experimental values are well known. The reduced transition probability is

$$\begin{aligned} B(E2; 2^+ \rightarrow 0^+) &= \left( \frac{\beta_2}{\sqrt{4\pi}} \right)^2 \left| \int dr \varphi_{n2}^*(r) r^2 \varphi_{n0}(r) \right|^2 \\ &\approx \left( \frac{Z_1 Z_2}{\sqrt{4\pi} Z} \right)^2 \left| \int dr \varphi_{n2}^*(r) r^2 \varphi_{n0}(r) \right|^2, \end{aligned} \quad (2.4.52)$$

where we have used the dipole constraint defined in 2.4.51.

## 2.5 Mean Square Charge Radius

This quantity accounts for the nuclear shape and demonstrates a large degree of surface clustering. Its value is estimated according to [75]:

$$\langle r_{ch}^2 \rangle = \frac{Z_1}{Z_1 + Z_2} \langle r_{ch1}^2 \rangle + \frac{Z_2}{Z_1 + Z_2} \langle r_{ch2}^2 \rangle + \frac{Z_1 A_2^2 + Z_2 A_1^2}{(Z_1 + Z_2)(A_1 + A_2)^2} \langle r_m^2 \rangle \quad (2.5.1)$$

where  $\langle r_{ch1}^2 \rangle$  and  $\langle r_{ch2}^2 \rangle$  are core and cluster rms charge radii and  $\langle r_m^2 \rangle$  their mean square separation defined as

$$\langle r_m^2 \rangle = \int_0^\infty r^2 \varphi_{nL}^2(r) dr. \quad (2.5.2)$$

Here the radial wave function  $\varphi_{nL}(r)$  obtained from the radial Schrödinger equation 2.4.1 is normalized to unity.

## 2.6 Deformations Parameters

In the relativistic-mean-field-theory formalism, the signature of cluster states are indicated by large deformations [32]. This suggests the knowledge of quadrupole moments for protons and neutrons which are measurable observables. These observables are related to the expectation values of spherical harmonics such that

$$\langle r^2 Y_{20}(\theta, 0) \rangle_{p,n} = \frac{1}{2} \sqrt{\frac{5}{4\pi}} Q_{p,n}. \quad (2.6.1)$$

Though, it will be rather convenient to express these quantities as a dimensionless deformation parameter  $\beta_2$ , in such a way that the matter quadrupole moment  $Q_{20}$

$$Q_{20} = Q_p + Q_n = \frac{3}{4\pi} \sqrt{\frac{16\pi}{5}} A R_0^2 \beta_2. \quad (2.6.2)$$

with

$$R_0 = 1.2A^{1/3}$$

Having described tools that we needed in order to investigate nuclear spectroscopy within binary cluster models, in the next chapter, we will be discussing different potential models of interest.



## Chapter 3

# Nuclear Cluster-Core Potential

### 3.1 Introduction

Optical potentials enable not only excellent fits to elastic and inelastic scattering data but also allow one to describe the excitation energies of cluster states in given nuclei and their  $\gamma$ -decay properties. The bound cluster-core system is considered as a projectile-target system in their respective ground states. The two nuclei interact with each other through the two-nucleon interaction, which is described as an effective interaction. In the following sections, different potential models are discussed.

### 3.2 Phenomenological Nuclear Potential

The phenomenological potential is constructed on a basis of certain considerations based on the bulk properties related to specific nuclear phenomenon such as nuclear clustering. It depends on some parameters related to its geometrical functional form that need to be adjusted so that they may fit to experimental data. A widely known is the Saxon-Woods plus Saxon-Woods cubed (SW + SW<sup>3</sup>) [27],

$$U(r) = -V_0 \left[ \frac{x}{1 + \exp\left(\frac{r-R}{a}\right)} + \frac{1-x}{\left[1 + \exp\left(\frac{r-R}{3a}\right)\right]^3} \right]. \quad (3.2.1)$$

Here  $V_0$ , defines the depth of the potential, while  $x$ ,  $a$  and  $R$ , are the mixing parameter, the diffuseness and the nuclear radius.

This potential reproduces consistently the alpha and exotic decay half-lives. It also predicts accurately the level structures of nuclei in the rare earth and actinide regions. Notwithstanding its success, very little with regard to the microscopic nature of clustering in closed shell nuclei is known about this potential model. For this reason, in the following sections two reliable microscopic approaches will be developed and the results compared.

### 3.3 Microscopic Nonrelativistic Nuclear Potential

The microscopic potential is constructing out of the global properties using nucleon-nucleon interaction. We will develop a multiple scattering formalism in order to derive the effective interaction for the bound cluster-core system.

#### 3.3.1 Multiple Scattering Formalism

Consider an interacting system consisting of projectile and target nuclei denoting the core and cluster with atomic numbers  $A_1$  and  $A_2$ . The Schrödinger equation describing the two-body system is written as

$$\left(\mathcal{E} - \hat{\mathcal{H}}_{A_1} - \hat{\mathcal{H}}_{A_2} - \hat{T}_0 - \hat{\mathcal{V}}\right) \Psi = 0, \quad (3.3.1)$$

where  $\mathcal{E}$  is the total relative energy.

$$\hat{\mathcal{V}} = \sum_{i=1}^{A_1} \sum_j^{A_2} v_{ij} \quad (3.3.2)$$

defining the pairwise interaction between the  $i$ -th nucleon in the core and  $j$ -th nucleon in the cluster; and summed over the total number of nucleons of both nuclei and  $\mathcal{E}$  defining the energy of the system.

The operator  $\hat{T}_0$  is the corresponding kinetic energy acting on the relative coordinates of the  $A_1 + A_2$  nucleons.

The intrinsic structures (shell structure) of  $A_1$  core nucleons, and  $A_2$  cluster nucleons are included in  $\hat{\mathcal{H}}_{A_1}$  and  $\hat{\mathcal{H}}_{A_2}$ .

These Hamiltonians are just the sum of the one-nucleon kinetic energy plus the sum of their pair interactions such that

$$\begin{aligned} \hat{\mathcal{H}}_{A_1} &= \sum_{i=1}^{A_1} h_i + \sum_{i<j}^{A_1} u_{ij} \\ \hat{\mathcal{H}}_{A_2} &= \sum_{l=1}^{A_2} h_l + \sum_{l<m}^{A_2} u_{lm}, \end{aligned} \quad (3.3.3)$$

with  $h_i = -(\hbar^2/2m_i) \nabla_i^2$  kinetic energy of nucleon in  $A_i$  nucleons and  $u_{ij} = u(\mathbf{r}_i - \mathbf{r}_j)$  their inter-nucleon interaction.

The antisymmetrization between these two nuclei is neglected for the moment. Thus, the total wave function is expanded according to

$$\Psi(\mathbf{r}_1, \dots, \mathbf{r}_{A_1}; \mathbf{r}'_1, \dots, \mathbf{r}'_{A_2}) = \sum_{\alpha\beta} \psi_{\alpha\beta}(\mathbf{r}) \varphi_{\alpha}(\mathbf{r}_1, \dots, \mathbf{r}_{A_1}) \phi_{\beta}(\mathbf{r}'_1, \dots, \mathbf{r}'_{A_2}). \quad (3.3.4)$$

$\psi_{\alpha\beta}(\mathbf{r})$  is the wave function describing the cluster-core relative motion.

The physical antisymmetric eigenstates of  $\hat{\mathcal{H}}_{A_1}$  and  $\hat{\mathcal{H}}_{A_2}$  are solutions of equations

$$\begin{aligned}\hat{\mathcal{H}}_{A_1}\varphi_{\alpha}(\mathbf{r}_1, \dots, \mathbf{r}_{A_1}) &= \varepsilon_{\alpha}\varphi_{\alpha}(\mathbf{r}_1, \dots, \mathbf{r}_{A_1}) \\ \hat{\mathcal{H}}_{A_2}\phi_{\beta}(\mathbf{r}'_1, \dots, \mathbf{r}'_{A_2}) &= \varepsilon_{\beta}\phi_{\beta}(\mathbf{r}'_1, \dots, \mathbf{r}'_{A_2}).\end{aligned}\quad (3.3.5)$$

Here  $\varepsilon_{\alpha}$  and  $\varepsilon_{\beta}$  are eigenenergies associated to eigenfunctions  $\varphi_{\alpha}$  and  $\phi_{\beta}$ .

The subscript  $\alpha$  and  $\beta$  represent the usual set of quantum numbers  $\{nlm_j; m_i\}$ ;  $m_i$  being the nucleon isospin projection.

The formal *Lippmann – Schwinger* solution of the equation 3.3.1 is

$$\Psi^+ = \Phi + \frac{1}{\mathcal{E} - \hat{\mathcal{H}}_0 + i\delta} \hat{\mathcal{V}}\Psi^+ \quad (3.3.6)$$

where  $\Phi$  is the solution of homogeneous equation

$$(\mathcal{E} - \hat{\mathcal{H}}_0) \Phi = 0. \quad (3.3.7)$$

With  $\hat{\mathcal{H}}_0 = \hat{\mathcal{H}}_{A_1} + \hat{\mathcal{H}}_{A_2} + \hat{T}_0$ , defining the non-interacting Hamiltonian of the cluster-core system.

The  $+i\delta$  insures the proper boundary conditions for scattering.

One may also expand the homogeneous solution according to

$$\Phi(\mathbf{r}_1, \dots, \mathbf{r}_{A_1}; \mathbf{r}'_1, \dots, \mathbf{r}'_{A_2}) = \sum_{\alpha\beta} \chi_{\alpha\beta}(\mathbf{r}) \varphi_{\alpha}(\mathbf{r}_1, \dots, \mathbf{r}_{A_1}) \phi_{\beta}(\mathbf{r}'_1, \dots, \mathbf{r}'_{A_2}). \quad (3.3.8)$$

$\chi_{\alpha\beta}(\mathbf{r})$  describes the free propagation in the relative cluster-core nuclear coordinates.

Now, we rewrite equation 3.3.6 as a series by repeatedly using the definition of  $\Psi^+$  on the right hand side

$$\Psi^+ = \Phi + \frac{1}{\mathcal{E} - \hat{\mathcal{H}}_0} \hat{\mathcal{V}}\Phi + \frac{1}{\mathcal{E} - \hat{\mathcal{H}}_0 + i\delta} \hat{\mathcal{V}} \frac{1}{\mathcal{E} - \hat{\mathcal{H}}_0 + i\delta} \hat{\mathcal{V}}\Phi \dots = \sum_{n=0}^{\infty} \left( \frac{1}{\mathcal{E} - \hat{\mathcal{H}}_0 + i\delta} \hat{\mathcal{V}} \right)^n \Phi \quad (3.3.9)$$

which defines the *Born series*.

From equation 3.3.9 we define the transition operator, the main ingredient for determining the potential, as

$$\hat{T} = \hat{\mathcal{V}} + \hat{\mathcal{V}}\hat{G}(\mathcal{E})\hat{T} \quad (3.3.10)$$

where

$$\hat{G}(\mathcal{E}) = \frac{1}{\mathcal{E} - \hat{\mathcal{H}}_0} \quad (3.3.11)$$

is the unperturbed Green function.

Equation 3.3.10 defines the *Lippmann – Schwinger* relation for the cluster-core transition operator. Next we would like to derive explicitly the multiple series of the cluster-core potential.

### 3.3.2 First Order Nuclear Cluster-Core Optical Potential

We consider the elastic channel in which both cluster and core remain in their respective ground states such that  $\alpha = \beta = 0$ . As a result, all the contributions from virtual excitation of the core and internal excitation of the cluster nuclei are included in an effective one-body potential. This is the so-called *optical potential* ("*passive medium*" in which both nuclei are treated as though they cannot be excited).

To proceed with this, one follows the projection technique of *Feshbach* [76, 77]. It is now convenient to introduce the ground state projector defined as

$$\hat{\mathcal{P}} = |\varphi_0\phi_0\rangle\langle\varphi_0\phi_0| \quad (3.3.12)$$

and the excited state projector

$$\hat{\mathcal{Q}} = \sum_{\alpha \neq 0, \beta \neq 0} |\varphi_\alpha\phi_\beta\rangle\langle\varphi_\alpha\phi_\beta|, \quad (3.3.13)$$

so that

$$\hat{\mathcal{P}} + \hat{\mathcal{Q}} = 1. \quad (3.3.14)$$

And noting that  $\hat{\mathcal{P}}^2 = \hat{\mathcal{P}}$ ,  $\hat{\mathcal{Q}}^2 = \hat{\mathcal{Q}}$ , and  $[\hat{\mathcal{P}}, \hat{\mathcal{Q}}] = [\hat{\mathcal{P}}, \hat{G}] = [\hat{\mathcal{Q}}, \hat{G}] = 0$ .

Starting from 3.3.10, after inserting the relation 3.3.14, we therefore obtain

$$\hat{T} = \hat{\mathcal{V}} + \hat{\mathcal{V}}\hat{G}\hat{\mathcal{P}}\hat{T} + \hat{\mathcal{V}}\hat{G}\hat{\mathcal{Q}}\hat{T}, \quad (3.3.15)$$

which can be rearranged as

$$(1 - \hat{\mathcal{V}}\hat{G}\hat{\mathcal{Q}})\hat{T} = \hat{\mathcal{V}} + \hat{\mathcal{V}}\hat{G}\hat{\mathcal{P}}\hat{T} \quad (3.3.16)$$

or by multiplying both sides by  $(1 - \hat{\mathcal{V}}\hat{G}\hat{\mathcal{Q}})^{-1}$ , one gets

$$\hat{T} = (1 - \hat{\mathcal{V}}\hat{G}\hat{\mathcal{Q}})^{-1}\hat{\mathcal{V}} + (1 - \hat{\mathcal{V}}\hat{G}\hat{\mathcal{Q}})^{-1}\hat{\mathcal{V}}\hat{G}\hat{\mathcal{P}}\hat{T}. \quad (3.3.17)$$

We define

$$\hat{U} = (1 - \hat{V}\hat{G}\hat{Q})^{-1}\hat{V}, \quad (3.3.18)$$

as an *effective interaction*.

Because both  $\hat{P}$  and  $\hat{Q}$  commute with  $\hat{G}$ , one may rewrite  $\hat{T}$  and  $\hat{U}$  as

$$\hat{T} = \hat{U} + \hat{U}\hat{P}\hat{G}\hat{P}\hat{T} \quad (3.3.19)$$

and

$$\hat{U} = \hat{V} + \hat{V}\hat{Q}\hat{G}\hat{Q}\hat{U}. \quad (3.3.20)$$

Both, equations 3.3.19 and 3.3.20 are equivalent to 3.3.10. The  $\hat{U}$  appearing defines the optical potential expressed in terms of the two-body interaction  $\hat{V}$ . This actual nucleon-nucleon interaction  $\hat{V}$  is highly singular. Indeed it possesses a strong repulsion at short range (hard core). This renders invalid to construct any perturbation theory based on such a potential. It will be more convenient to express  $\hat{U}$  in terms of the two-nucleon nonsingular operator, instead of  $\hat{V}$ .

Thus, one may express  $\hat{U}$  as [78],

$$\hat{U} = \sum_{j=1}^{A_2} U_j, \quad (3.3.21)$$

where

$$U_j = \sum_{i=1}^{A_1} U_{ij}. \quad (3.3.22)$$

We start by rewriting equation 3.3.20 as,

$$U_j = \mathcal{V}_j + \mathcal{V}_j\hat{Q}\hat{G}\hat{Q}\sum_{k=1}^{A_2} U_k = \mathcal{V}_j + \mathcal{V}_j\hat{Q}\hat{G}\hat{Q}U_j + \mathcal{V}_j\hat{Q}\hat{G}\hat{Q}\sum_{k \neq j}^{A_2} U_k. \quad (3.3.23)$$

Consequently, we are in the process of defining the nonsingular operator in terms of the singular two-body interaction  $\hat{V}$ , the so-called Watson operator  $\tau$  [79, 80], such that

$$\tau_j = \mathcal{V}_j + \mathcal{V}_j\hat{Q}\hat{G}\hat{Q}\tau_j = \mathcal{V}_j + \mathcal{V}_j\hat{Q}\hat{G}\hat{Q}\mathcal{V}_j + \mathcal{V}_j\hat{Q}\hat{G}\hat{Q}\mathcal{V}_j\hat{Q}\hat{G}\hat{Q}\mathcal{V}_j + \dots \quad (3.3.24)$$

Eventually, from equations 3.3.24 and 3.3.23,  $U_j$  can be expressed in terms of  $\tau$ ,

$$U_j = \tau_j + \tau_j\hat{Q}\hat{G}\hat{Q}\sum_{k \neq j}^{A_2} U_k. \quad (3.3.25)$$

Hence, summing over the index  $j$  in the last equation yields,

$$\hat{U} = \sum_j^{A_2} \tau_j + \sum_{j,j \neq k}^{A_2} \tau_j \hat{Q} \hat{G} \hat{Q} \tau_k \cdots \quad (3.3.26)$$

This is the analogue of the Watson multiple scattering series for the optical potential [81]. This series is a central key in nuclear physics. It expresses the many-body operator  $\hat{U}$  in terms of the sum of two-body operators  $\tau_{ij}$  rather than  $\mathcal{V}_{ij}$ . Hence each term in the series can be interpreted as single (single interaction between the  $i$ -th cluster nucleon and  $j$ -th core nucleon), double scattering (a double interaction between the  $i$ -th cluster nucleon and  $j$ -th core nucleon) of each bound nucleon in the cluster from the bound core nucleons which means .

Since the nucleus is assumed to be a dilute system, the likelihood that each nucleon inside the cluster will strike more than one different nucleon in the core remains negligible. Indeed , only the first term will be relevant in the series. This is the so-called *first – order Watson Optical Potential*,

$$\hat{U}^{1st} = \sum_{j=1}^{A_2} \tau_j = \sum_{i=1}^{A_1} \sum_{j=1}^{A_2} \tau_{ij}. \quad (3.3.27)$$

This expression is analogous to [80, 82] for the case of the proton-nucleus optical potential.

The complex  $\tau$ -matrix in this equation involves the two-body interaction  $\mathcal{V}_{ij}$  which is related to nuclear properties. In the next section we discuss the effective nucleon-nucleon interactions, the central key in determining the nucleus-nucleus potential.

### 3.3.3 Microscopic Effective Nucleon-Nucleon Interaction

The microscopic knowledge of interactions between complex nuclei consisting of nucleons, starting from the bare nucleon-nucleon interaction in free space is one of the most crucial subjects in nuclear physics. For the nucleus-nucleus potential constructed from the bare nucleon-nucleon interaction, one has to efficiently deal with the many-body effects due to the nuclear medium. Consequently, one has to introduce an effective nucleon-nucleon interaction that contains the medium effects in the multiple scattering framework developed before, such as the  $\hat{\tau}$ -matrix,  $\hat{\mathcal{R}}$ -matrix, and  $\hat{\mathcal{G}}$ -matrix interactions. These nuclear medium effects are induced by the Fermi motion, the binding energies and the Pauli blocking [58, 83–85]. Such effective interactions should be adjusted to

the scattering phase shifts and binding energies. They are in principle density and energy dependent. The basic approach to calculate the medium effects as discussed in refs. [84] is to substitute the complicated  $(A_1 + A_2)$ -body projector operator  $\hat{Q}\hat{G}\hat{Q}$  in the definition of  $\tau_{ij}$  by an appropriate operator which takes into account the nuclear medium effects as discussed above. One way is to replacing with the similar two-nucleons system operator in the infinite nuclear matter of well defined Fermi momentum. The application to finite nuclear matter being done through the local density approximation (LDA).

We will not make any attempt to derive the effective interaction due to medium effects here, but we rather give some insights that lead to the calculation of the  $\hat{G}$ -matrix.

Thus for low-energy cluster-core potential, the estimate full many-body propagator that takes into account the medium effect is defined as

$$\hat{Q}\hat{G}\hat{Q} \simeq \frac{\hat{Q}_F}{e}. \quad (3.3.28)$$

The projection operator  $\hat{Q}_F$  is the usual Pauli blocking operator that prevents the two nucleons in the cluster-core system from sitting in states already occupied by  $(A_1 + A_2)$ -2 nucleons. And  $e$  is the energy denominator of the two propagating nucleons in the infinite nuclear matter.

For the  $\hat{G}$ -matrix, resulting from bare nucleon-nucleon interaction, one has to solve, the two-body Schrödinger equation named Bethe-Goldstone's equation

$$\left(T_i + T_j + U_i + U_j - E\right)\psi = \hat{Q}_F \mathcal{V}_{ij}. \quad (3.3.29)$$

In order to define the matrix elements of the operator  $\hat{G}$ , we follow the approaches given in [58, 86–88]. We will slightly change the notation, but the formulation will remain the same.

We consider a pair of nucleons in momentum space, one propagating with momentum  $\mathbf{p}_i$ , and a bound nucleon with momentum  $\mathbf{p}_j$  in nuclear matter of Fermi momentum  $k_F$ . With  $\mathbf{K}_C = \mathbf{p}_i + \mathbf{p}_j$  and  $\mathbf{q} = \frac{\mathbf{p}_i - \mathbf{p}_j}{2}$ , defining respectively the centre-of-mass and relative momenta. The scattering of the nucleon pair in the nuclear medium is described by the  $\hat{G}$ -matrix, obtained by solving the Brückner's equation [89],

with

$$\hat{G}(\omega) = \mathcal{V}_{ij} + \sum_{\mathbf{q}_i, \mathbf{q}_j} \mathcal{V}_{ij} \frac{\hat{Q}_F(\mathbf{q}_i, \mathbf{q}_j)}{\omega - e(\mathbf{q}_i) - e(\mathbf{q}_j) + i\epsilon} \hat{G}(\omega). \quad (3.3.30)$$

Here  $\mathcal{V}_{ij}$  is the bare nucleon-nucleon interaction.

The Pauli blocking operator is defined by

$$Q_F(\mathbf{q}_i, \mathbf{q}_j)|\mathbf{q}_i, \mathbf{q}_j\rangle = \begin{cases} |\mathbf{q}_i, \mathbf{q}_j\rangle, & \mathbf{q}_i, \mathbf{q}_j > 0 \\ 0 & \text{otherwise} \end{cases}. \quad (3.331)$$

Here  $e(q_i)$ , represents a single-particle energy in an intermediate state with momentum  $q_i$ . The starting energy  $\omega$ , is the sum of energy of the incoming nucleon,  $E(p_i)$  and the single-particle energy,

$$E(p_i) = \frac{\hbar^2 p_i^2}{2m} + U(p_i, e(p_i)) \quad (3.332)$$

and

$$e(p_j) = \frac{\hbar^2 p_j^2}{2m} + U(p_j, e(p_j)), \quad (3.333)$$

where  $U(p_i, e(p_i))$ , represents the single particle potential.

The estimated  $\hat{\mathcal{G}}$ -matrix is achieved with the so-called continuous choice for intermediate nucleon spectra, crucial for its imaginary part coming from  $i\epsilon$ . Consequently, the single particle energies

$$e(q) = \frac{\hbar^2 q^2}{2m} + U(q, e(q)) \quad (3.334)$$

are calculated self-consistently for both bound ( $q \leq k_F$ ) and intermediate ( $q > k_F$ ) states where  $k_F$  is the Fermi momentum associated with the nuclear matter density  $\rho$ . However, the state of a nucleon pair is given by a set  $(T, S, L, J)$ , where  $T$ , denotes the relative isospin and  $S$ ,  $L$  and  $J$  are relative spin, orbital and total angular momenta. The corresponding relative scattering wave is obtained by solving the equation,

$$u_{LL'}^{TSJ}(r; q) = J_L(qr)\delta_{LL'} + 4\pi \sum_{L''} \int_0^\infty r'^2 dr' F_L(r, r'; q) \mathcal{V}_{L'L''}^{TSJ}(r') u_{LL''}^{TSJ}(r'', q). \quad (3.335)$$

And

$$F_L(r, r'; q) = \frac{1}{2\pi^2} \int_0^\infty q'^2 dq' \frac{\bar{Q}_F(q', \hat{K}_c; k_F) J_L(q'r) J_L(q'r')}{\omega - \left[ \frac{\hbar^2 q'^2}{m} + \frac{\hbar^2 \hat{K}_c^2}{4m} + U_R(\bar{q}'_+) + U_R(\bar{q}'_-) \right]} \quad (3.336)$$

where  $j_L(qr)$  is a spherical Bessel function.  $\bar{Q}_F$ ,  $\hat{K}_c$ , and  $\bar{q}_\pm$  are the angle-averaged expressions for the Pauli operator  $Q_F$ , the centre-of mass,  $K_c$  and



the relative,  $q$ , momenta. Here,  $U_R(q) = \text{Re}(U(q))$ . The  $\hat{\mathcal{G}}$ -matrix element and the single-particle potential are calculated as follows:

$$\langle q | G_{LL}^{TSJ} | q \rangle = 4\pi \int_0^\infty r^2 dr J_L(qr) \mathcal{V}_{LL''}^{TSJ}(r) u_{LL'}^{TSJ}(r; q) \quad (3.3.37)$$

and

$$U(p_i, E(p_i); k_F) = \frac{1}{2\pi} \int_0^\infty q^2 dq Z(q; p_i, k_F) \sum_{TSJT} \frac{1}{2} (2J+1)(2T+1) \langle q | G_{LL}^{TSJ} | q \rangle \quad (3.3.38)$$

where

$$Z(q; p_i, k_F) = \frac{1}{p_i q} \left[ k_F^2 - (p_i - 2q)^2 \right]. \quad (3.3.39)$$

The local form representation of the  $\hat{\mathcal{G}}$ -matrix in position space is [58, 86]

$$G_{LL'}^{TSJ}(r; k_F, E(p_i)) = \frac{\int q^2 dq Z(q; p_i, k_F) J_L'(qr) \sum_{L''} \mathcal{V}_{L'L''}^{TSJ}(r) u_{LL'}^{TSJ}(r; q)}{\int q^2 dq Z(q; p_i, k_F) J_L'(qr) J_L(qr)}. \quad (3.3.40)$$

### 3.3.4 Complex Effective Gaussian Form Factor: CEG

The estimated interaction  $G_{LL'}^{TSJ}(r)$  from equation 3.3.40, is parametrized as a linear three-range Gaussian form factor: the outer two ranges are determined by fitting the radial form of  $G_{LL'}^{TSJ}(r)$  in long- and intermediate-range regions, and the innermost part is fixed so as to reproduce the (LSJT)-state contribution of the single-particle potential  $U$ . We ignore the non central part since our model is geared for spin zero nuclei. In our model, we will test the first prototype, density-dependent *complex effective gaussian form factor* (CEG83), (developed by Yamaguchi in 1983) [58] whose functional form is given by

$$V^{ST}(r; k_F, \bar{E}) = \sum_{i=1}^3 v_i^{ST}(k_F; \bar{E}) \exp\left(-\frac{r}{\lambda_i}\right)^2 \quad (3.3.41)$$

and

$$v_i(k_F; \bar{E}) = v_{0i}(\bar{E}) \left( 1 + \alpha_i(\bar{E}) k_F + \beta_i(\bar{E}) k_F^2 \right). \quad (3.3.42)$$

Note that  $\bar{E} = E/A_2$ . The parameters for this interaction are given in chapter 4.

### 3.3.5 Semi-realistic Effective Interaction: M3Y

The M3Y (Michigan 3-range Yukawa) [23, 90–92] interaction is a kind of  $\hat{\mathcal{G}}$ -matrix. It is real and weakly energy dependent with zero imaginary part. It has the direct  $V_D$  and exchange  $V_{EX}$  parts. These parts are determined from

the singlet- and triplet even ( $V_{SE}, V_{TE}$ ) and odd ( $V_{SO}, V_{TO}$ ) components of the two-nucleon forces. The direct  $V_D$  and exchange  $V_{EX}$  parts of the central nucleon-nucleon forces which are of interest in our model, are expressed in terms of the spin-isospin dependent components as

$$V^{eff}(r) = \sum_{T=0}^1 \sum_{S=0}^1 V_{D(EX)}^{ST}(r) \boldsymbol{\sigma}_{A_1}^S \boldsymbol{\sigma}_{A_2}^S \mathcal{I}_{A_1}^T \mathcal{I}_{A_2}^T, \quad (3.3.43)$$

where  $\boldsymbol{\sigma}_{A_i}^0 = 1$ ,  $\boldsymbol{\sigma}_{A_i}^1 = \boldsymbol{\sigma}_{A_i}$ ,  $\mathcal{I}_{A_i}^0 = 1$ ,  $\mathcal{I}_{A_i}^1 = \mathcal{I}_{A_i}$  are two-dimensional unit, spin and isospin matrices.

The explicit radial dependences of the  $V_{D(EX)}^{ST}(r)$  interaction are written as a linear combination of the three-range Yukawa functions, for both the direct and exchange parts;

$$V_{D(EX)}^{ST}(r) = \sum_{n=1}^3 v_{D(EX)}^n \left[ \exp\left(-r/R_n\right) \right] / (r/R_n). \quad (3.3.44)$$

The exchange part which represents the single knock-on exchange is given by the zero-range interaction of the form

$$V_{EX}^{ST}(\mathbf{r}) = G_0(1 - E/A_1)\delta(\mathbf{r}). \quad (3.3.45)$$

There are two parametrizations of the M3Y interaction, Paris and Reid which are well known in the literature. The values of parameters,  $v_{D(EX)}^n$ ,  $G_0$  and  $R_n$  are listed in chapter 4.

### 3.3.6 Double-Folded Model for Nuclear Cluster-Core Potential

In the case of the cluster-core system, the double-folding model (DFM) in the lowest approximation is expressed as a Hartree-Fock type potential [93–95],

$$\begin{aligned} U &= U_D + U_{EX} \\ &= \sum_{i=1}^{A_1} \sum_{j=1}^{A_2} \left[ \langle \varphi_{A_1} \otimes \phi_{A_2} | V_{ij(D)} | \varphi_{A_1} \otimes \phi_{A_2} \rangle + \langle \varphi_{A_1} \otimes \phi_{A_2} | V_{ij(EX)} | \phi_{A_2} \otimes \varphi_{A_1} \rangle \right]. \end{aligned} \quad (3.3.46)$$

$V_{(D)}$  and  $V_{(EX)}$  are the two-body direct and exchange parts of the effective interaction  $\tau_{ij}$  defined in equation 3.3.24 or the  $\hat{\mathcal{G}}$ -matrix such that

$$V_{D(EX)} = \frac{1}{16} \left( 3V^{TE} + 3V^{SE} \pm 9V^{TO} \pm V^{SO} \right) \quad (3.3.47)$$

where the singlet and triplet even ( $V^{TE}, V^{SE}$ ) and odd ( $V^{TO}, V^{SO}$ ) components are obtained either from 3.3.41 or 3.3.44. Note that the upper and lower parts of the double-sign symbols correspond to the direct (D) and exchange (EX) parts of the effective interaction, respectively.

The exchange part is included because of the single-nucleon knock-on exchange due to the antisymmetry between cluster and core wave functions required by the Pauli exclusion.

The cluster and core many-body wave function is expanded in single particle state basis  $|\mathbf{r}\rangle = |\mathbf{x}, nlm_j m_i\rangle$ , such that

$$\begin{aligned} |\varphi_{A_1}\rangle &= \int d\mathbf{r}_1 \cdots d\mathbf{r}_{A_1} \varphi_{A_1}(\mathbf{r}_1 \cdots \mathbf{r}_{A_1}) |\mathbf{r}_1 \cdots \mathbf{r}_{A_1}\rangle \\ |\phi_{A_2}\rangle &= \int d\mathbf{r}'_1 \cdots d\mathbf{r}'_{A_2} \phi_{A_2}(\mathbf{r}'_1 \cdots \mathbf{r}'_{A_2}) |\mathbf{r}'_1 \cdots \mathbf{r}'_{A_2}\rangle \end{aligned} \quad (3.3.48)$$

$\varphi_{A_1}(\mathbf{r}_1, \cdots, \mathbf{r}_{A_1})$  and  $\phi_{A_2}(\mathbf{r}'_1, \cdots, \mathbf{r}'_{A_2})$  are the antisymmetrized product of independent particle wave functions represented by the Slater determinant:

$$\begin{aligned} \varphi_{A_1}(\mathbf{r}_1, \cdots, \mathbf{r}_{A_1}) &= \frac{1}{\sqrt{A_1!}} \sum_P (-1)^{P_1} \prod_{i=1}^{A_1} \varphi_{iP_1}(\mathbf{r}_i) \\ \phi_{A_2}(\mathbf{r}'_1, \cdots, \mathbf{r}'_{A_2}) &= \frac{1}{\sqrt{A_2!}} \sum_P (-1)^{P_2} \prod_{j=1}^{A_2} \phi_{jP_2}(\mathbf{r}'_j) \end{aligned} \quad (3.3.49)$$

The sum extends over all possible permutations with  $P_i$  being even or odd with respect to the type of permutation.

The antisymmetrized matrix element of the cluster-core microscopic interaction can be evaluated using these expansions as

$$\begin{aligned} U &= \sum_{i=1}^{A_1} \sum_{j=1}^{A_2} \left[ \int \int d\mathbf{r}_1 d\mathbf{r}'_2 \varphi_i^*(\mathbf{r}_1) \otimes \phi_j^*(\mathbf{r}'_2) V_D(\mathbf{r}_1, \mathbf{r}'_2) \varphi_i(\mathbf{r}_1) \otimes \phi_j(\mathbf{r}'_2) + \right. \\ &\quad \left. \int \int d\mathbf{r}_1 d\mathbf{r}'_2 \varphi_i^*(\mathbf{r}_1) \otimes \phi_j^*(\mathbf{r}'_2) V_{EX}(\mathbf{r}_1, \mathbf{r}'_2) \varphi_i(\mathbf{r}'_2) \otimes \phi_j(\mathbf{r}_1) \right] \end{aligned} \quad (3.3.50)$$

The direct part of the Hartree-Fock type potential in equation 3.3.50 is reduced to the double convolution integrals over nucleon densities of the interacting dinuclear system and the effective nucleon-nucleon interaction [92, 93],

$$U_D(\mathbf{r}) = \int \int \rho_{A_1}(\mathbf{r}_1) \rho_{A_2}(\mathbf{r}'_2) V_D(\mathbf{s}) d\mathbf{r}_1 d\mathbf{r}'_2. \quad (3.3.51)$$

Here,  $\mathbf{r}$  is the relative coordinate of the interacting nuclei between their centres of mass. And  $\mathbf{s} = \mathbf{r} + \mathbf{r}'_2 - \mathbf{r}_1$  is the relative coordinate between a nucleon

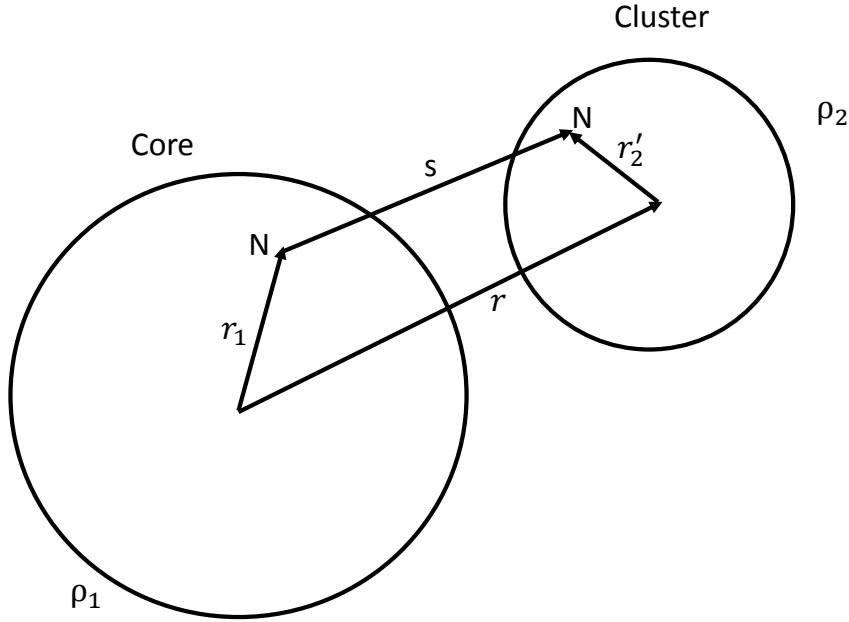


**Figure 3.1:** Cluster-Core coordinates used in the double folded model

at the spatial position  $\mathbf{r}_1$  with respect to the centre of mass (c.m.) of nucleus  $A_1$  and another nucleon at the spatial position  $\mathbf{r}'_1$  with respect to the c.m. of nucleus  $A_2$ , figure 3.1 taken from ref. [63].

However, the exchange potential which, in principle non-local, is approximated by a local form in the same way as in [94, 95],

$$U_{EX}(\mathbf{r}) = \int \int \rho_{A_1}(\mathbf{r}_1, +\mathbf{r}_1 + \mathbf{s}) \rho_{A_2}(\mathbf{r}'_2, \mathbf{r}'_2 - \mathbf{s}) V_{EX}(\mathbf{s}) d\mathbf{r}_1 d\mathbf{r}'_2 \exp\left[\frac{i\mathbf{k}(\mathbf{r}) \cdot \mathbf{s}}{\mu}\right]. \quad (3.3.52)$$

Here

$$k^2(\mathbf{r}) = \frac{2M\mu}{\hbar^2} \left[ E_c - \text{Re}(U(\mathbf{r})) - U_C(\mathbf{r}) \right] \quad (3.3.53)$$

is the local momentum defining the relative motion of the cluster-core system.  $E_c$  is the centre-of-mass energy,  $M$ , the nucleon mass while  $\mu = A_1 A_2 / (A_1 + A_2)$

is the reduced mass. And  $U_C$  is the Coulomb interaction.

The mixed densities  $\rho_{A_1}(\mathbf{r}_1, \mathbf{r}_1 + \mathbf{s})$  and  $\rho_{A_2}(\mathbf{r}'_2, \mathbf{r}'_2 - \mathbf{s})$  are approximated similarly to ref. [94] with the local densities

$$\begin{aligned}\rho_{A_1}(\mathbf{r}_1, \mathbf{r}_1 + \mathbf{s}) &\simeq \rho_{A_1}\left(\mathbf{r}_1 + \frac{\mathbf{s}}{2}\right)\hat{j}_1\left(K_{F_1}\left(\mathbf{r}_1 + \frac{\mathbf{s}}{2}\right)s\right) \\ \rho_{A_2}(\mathbf{r}'_2, \mathbf{r}'_2 - \mathbf{s}) &\simeq \rho_{A_2}\left(\mathbf{r}'_2 - \frac{\mathbf{s}}{2}\right)\hat{j}_1\left(K_{F_2}\left(\mathbf{r}'_2 - \frac{\mathbf{s}}{2}\right)s\right)\end{aligned}\quad (3.3.54)$$

where  $\hat{j}_1(x) = 3(\sin x - x \cos x)/x^3$ . In the extended Thomas-Fermi approximation [93, 94], the effective Fermi momentum is given by

$$K_F^2(\mathbf{r}) = \left[ \left(\frac{3\pi^2}{2}\rho(\mathbf{r})\right)^{2/3} + \frac{5C_s|\nabla\rho(\mathbf{r})|^2}{3\rho(\mathbf{r})^2} + \frac{5\nabla^2\rho(\mathbf{r})}{36\rho(\mathbf{r})} \right] \quad (3.3.55)$$

where  $C_s = 1/4$ .

In the case of a zero-range pseudo-interaction, the exchange potential is given by

$$U_{EX}(\mathbf{r}) = G_0(1 - E/A_2) \int \rho_{A_1}(\mathbf{r}_1)\rho_{A_2}(\mathbf{r}'_2)\delta(\mathbf{s})d\mathbf{r}_1d\mathbf{r}'_2. \quad (3.3.56)$$

The ground-state density distributions of the cluster and core are either Gaussian for the alpha particle,

$$\rho_A(r) = 0.4299\exp(-0.702r^2) \quad (3.3.57)$$

or the two-Fermi spherically symmetric form

$$\rho_A(r) = \frac{\rho_0}{1 + \exp\left(\frac{r-c}{a}\right)} \quad (3.3.58)$$

for either the core or cluster heavier than alpha.  $c = 1.07A^{1/3}$  and  $a$  is the diffuseness.  $\rho_0$  is fixed by normalizing the total density to the mass number  $A$ .

### 3.4 Microscopic Relativistic Nuclear Potential

Conventional wisdom suggests that for low-energy nuclear structure studies, relativistic effects are irrelevant. The fact that the largest kinetic energy of nucleons in the nucleus, being determined by the Fermi momentum

$K_F \approx 1.4fm^{-1}$  is  $T_{\max} = \frac{\hbar^2 K_F^2}{2M} \approx 38$  MeV which yields a velocity  $v \approx 0.29c$ , thus relativistic kinematics will induce minor modifications as one would expect. Nevertheless, in the past decades, relativistic nuclear structure models

have been proven to be significant for many reasons. The relativistic mean-field theory succeeded in describing the single particle model of nuclei and give a clear explanation of the spin-orbit interaction. The model of nucleons interacting through meson fields is related to a more fundamental theoretical field description of nuclear interactions. Relativistic Self-Consistent meson field theory of spherical nuclei properties in ref. [96] in extent of the non-relativistic case provides a good agreement between theoretical and experimental total binding energies and radial charge distributions. The list is not exhaustive.

In the spirit of this section, we aim to construct, firstly, a consistent cluster-core potential in the framework of the relativistic multiple scattering (RMS) formalism as suggested in [80, 82], and in a self-consistent relativistic Hartree approximation [96]. Secondly, investigate explicitly cluster aspects which are obviously present at higher deformations as reported in [32]. Here nucleon dynamics are described by the Dirac Hamiltonian with a two-body interaction [96, 97],

$$\hat{H} = \sum_{i=1}^A \left( c\boldsymbol{\alpha}_i \cdot \mathbf{p}_i + \beta m_N c^2 \right) + \sum_{i<j}^A V_{NN}(\mathbf{r}_i - \mathbf{r}_j) \quad (3.4.1)$$

where

$$\boldsymbol{\alpha}_i = \begin{pmatrix} \mathbf{0} & \boldsymbol{\sigma}_i \\ \boldsymbol{\sigma}_i & \mathbf{0} \end{pmatrix}, \quad \beta = \begin{pmatrix} \mathbf{1}_2 & \mathbf{0} \\ \mathbf{0} & -\mathbf{1}_2 \end{pmatrix} \quad (3.4.2)$$

are Dirac matrices. Next, the relativistic multiple scattering is formulated in the context of the relativistic meson exchange model.

### 3.4.1 Relativistic Multiple Scattering

We consider the interaction between an  $A_1$ -nucleon core and an  $A_2$ -nucleon cluster to be mediated by mesons. In the nonrelativistic multiple scattering (NRMS), we had the ability of separating the total Hamiltonian into an unperturbed Hamiltonian and residual interactions. However in the relativistic case, this is not straightforward because one cannot separate the total Hamiltonian defined in 3.4.1 as a sum of a Dirac Hamiltonian plus two-body interaction. Thus, the derivation of a multiple scattering series is still a remote problem for the field theoretical Lagrangian point of view. A RMS model for nucleon-nucleus scattering have been developed by Maung et al.[80, 82] in the context of boson exchange. We take the less ambitious route, but in the mould of NRMS as formulated by Charles M.Werneth and Khin M. Maung in [98] and assume that the relativistic cluster-core transition amplitude is described by Bethe-Salpeter's equation,

$$\hat{T} = \hat{K} + \hat{K}\hat{G}_0\hat{T} \quad (3.4.3)$$

where  $\hat{G}_0$  represents the four-dimensional propagator for the cluster-core system. In this equation, the kernel  $\hat{K}$  represents a key component which acts

realistically as two-body interaction, analogous to the nonrelativistic case. Therefore, the kernel can be expressed as

$$\hat{K} = \sum_{i=1}^{A_1} \sum_{j=1}^{A_2} (k_{ij} + \Lambda_{ij}) \quad (3.4.4)$$

where  $k_{ij}$  includes all the one-meson exchange diagrams. And the

$$\Lambda_{ij} = \sum_{ij} \sum_m R_{ijij}^{(m)} + \sum_{ij} \sum_m R_{iijj}^{(m)} + \dots \quad (3.4.5)$$

contains all multi-meson exchange terms between particles, as stated before. We adopt a one-boson-exchange (OBE) model by dropping out the multi-meson exchange terms  $\Lambda_{ij}$ .

We then define the  $\hat{K}$ -operator in terms of the driving term  $k_{ij}$  as

$$\hat{K} = \sum_{i=1}^{A_1} \sum_{j=1}^{A_2} k_{ij}. \quad (3.4.6)$$

### 3.4.2 Relativistic Optical Potential

Having defined our kernel, we then proceed by rewriting the Bethe-Salpeter equation for the transition operator  $\hat{T}$  as coupled equations between the elastic scattering and the defining optical potential, exactly like the nonrelativistic scheme given in equation 3.3.16. To this end we define the cluster-core ground state P and excited states Q projectors,

$$\hat{P} = \left| \phi_0^{A_1} \otimes \phi_0^{A_2} \right\rangle \left\langle \phi_0^{A_1} \otimes \phi_0^{A_2} \right|, \quad \hat{Q} = \sum_{n \neq 0} \left| \phi_n^{A_1} \otimes \phi_n^{A_2} \right\rangle \left\langle \phi_n^{A_1} \otimes \phi_n^{A_2} \right| \quad (3.4.7)$$

where

$$\hat{P} + \hat{Q} = 1. \quad (3.4.8)$$

From the procedure analogous to that developed in chapter 3 for the nonrelativistic case we obtain, the optical potential in a coupled equation

$$\hat{T} = \hat{U} + \hat{U} \hat{P} \hat{G}_0 \hat{P} \hat{T} \quad (3.4.9)$$

and

$$\hat{U} = \hat{K} + \hat{K} \hat{Q} \hat{G}_0 \hat{Q} \hat{U}. \quad (3.4.10)$$

We then write the relativistic multiple scattering series for the optical potential,

$$\hat{U} = \sum_{i=1}^{A_1} \sum_{j=1}^{A_2} k_{ij} + \sum_{i=1}^{A_1} \sum_{j=1}^{A_2} k_{ij} \hat{Q} \hat{G}_0 \hat{Q} \hat{U}. \quad (3.4.11)$$

We are at the stage of defining the pseudo relativistic two-body operator known as a two-body  $\tau$ -matrix in NRMS.

$$\tilde{\tau}_{ij} = k_{ij} + k_{ij} \hat{Q} \hat{G}_0 \hat{Q} \tilde{\tau}_{ij}. \quad (3.4.12)$$

The relativistic multiple scattering series of the optical potential then becomes,

$$\hat{U} = \sum_{i=1}^{A_1} \sum_{j=1}^{A_2} \tilde{\tau}_{ij} + \sum_{i=1}^{A_1} \sum_{j=1}^{A_2} \tilde{\tau}_{ij} \sum_{l \neq i}^{A_1} \sum_{m \neq j}^{A_2} \hat{Q} \hat{G}_0 \hat{Q} U_{lm}. \quad (3.4.13)$$

The evaluation of the operator  $\tilde{\tau}_{ij}$  defined in equation 3.4.12 is a very difficult task to perform. It contains in its kernel and propagator the effects of many-body interaction. One needs to approximate it with a free two-body amplitude (impulse approximation). This is a requirement since we have to assume that nucleons move independently in the nucleus and have enough momenta in such that they are not deflected and the scattering is nearly elastic. In this way, the free two-body amplitude has to be parametrized from the nucleon-nucleon experimental data (phase shifts), and corrections to medium effects have to be incorporated, as we shall see. Thus, the free nucleon-nucleon amplitude called  $\hat{t}$ -matrix is given by

$$\hat{t}_{ij}^{free} = k_{ij} + k_{ij} \hat{g} \hat{t}_{ij}^{free} \quad (3.4.14)$$

where  $\hat{g}$  is the free two-body propagator and  $k_{ij}$  retains the same definition of OBE diagrams as previously. We may express  $\tilde{\tau}$  in terms of  $\hat{t}^{free}$  and get

$$\tilde{\tau}_{ij} = \hat{t}_{ij}^{free} + \hat{t}_{ij}^{free} \left( \hat{Q} \hat{G}_0 \hat{Q} - \hat{g} \right) \tilde{\tau}_{ij}. \quad (3.4.15)$$

Inserting the two-body pseudo-operator  $\tilde{\tau}_{ij}$  in equation 3.4.15 into 3.4.10, yields the optical potential

$$\hat{U} = \sum_{i=1}^{A_1} \sum_{j=1}^{A_2} \hat{t}_{ij}^{free} + \sum_{i=1}^{A_1} \sum_{j=1}^{A_2} \hat{t}_{ij}^{free} \left( \hat{Q} \hat{G}_0 \hat{Q} \right) \sum_{l=1}^{A_1} \sum_{m=1}^{A_2} \hat{t}_{lm}^{free} + \dots \quad (3.4.16)$$

The first term is the single scattering between a nucleon in the cluster and a nucleon in the core. The remaining terms are double scattering of excited states and higher orders obtained through iteration which are neglected.

### 3.4.3 Relativistic Nucleon-Nucleon Amplitudes

The aim of this section is to express the general form of the relativistic  $\tilde{\tau}$ -matrix described in equation 3.4.15, consistent with rotational, parity, time-reversal and charge symmetry invariance for nucleon-nucleon elastic scattering which require 44 on-mass shell independent terms out of 256 for each isospin state. Only five of the 44 independent needed on-mass shell terms are determined



directly from phase shift analysis of nucleon-nucleon scattering data and thus the others must be predicted from a theoretical model [99–101].

The most general form of the Lorentz invariant nucleon-nucleon local amplitude that had been commonly used in nucleon-nucleus scattering, the so-called relativistic impulse approximation [60, 102], is given by

$$\tilde{\tau}_{NN}(E_c, |\mathbf{q}|) \equiv -\frac{4i\pi k_c}{M} \hat{\mathcal{F}}_{NN}(E_c, |\mathbf{q}|) \quad (3.4.17)$$

where

$$\hat{\mathcal{F}}_{NN}(E_c, |\mathbf{q}|) = \sum_{L=S}^T F^L(E_c, |\mathbf{q}|) \lambda_{(1)}^L \otimes \lambda_{(2)L}. \quad (3.4.18)$$

The  $L$ 's labelled the Dirac matrices outlined in table 3.1, while the subscript (1) and (2) refer to the cluster and core nucleons.

**Table 3.1:** *gamma matrices of the Dirac space*

$L$	$\lambda^L$
$S$ ( <i>scalar</i> )	$\mathbf{1}$
$V$ ( <i>vector</i> )	$\gamma^\mu$
$P$ ( <i>pseudoscalar</i> )	$\gamma^5$
$A$ ( <i>Axial – vector</i> )	$\gamma^5 \gamma^\mu$
$T$ ( <i>tensor</i> )	$\sigma^{\mu\nu}$

Clearly, the mapping between the  $\tau$  operator in Pauli spinor space, namely McNeil-Ray-Wallace (MRW) representation [102], the well known Wolfstein representation and the  $\tilde{\tau}$  operator in the Dirac spinor space yields the relation,

$$\chi_{s'_1}^\dagger \otimes \chi_{s'_2}^\dagger \tau_{NN}(E_c, |\mathbf{q}|) \chi_{s_1} \otimes \chi_{s_2} = \bar{U}(\mathbf{k}'_c, s'_1) \otimes \bar{U}(-\mathbf{k}'_c, s'_2) \times \tilde{\tau}_{NN}(E_c, |\mathbf{q}|) U(\mathbf{k}_c, s_1) \otimes U(-\mathbf{k}_c, s_2) \quad (3.4.19)$$

where  $\chi'$ s are different spin orientations of the Pauli spinor

$$\begin{aligned}\tau_{NN}(|\mathbf{q}|) &= (2ik_c)^{-1}f_{NN}(|\mathbf{q}|) \\ &= A(\mathbf{1}_1 \otimes \mathbf{1}_2) + B(\boldsymbol{\sigma}_1 \otimes \mathbf{1}_2) \cdot (\mathbf{1}_1 \otimes \boldsymbol{\sigma}_2) + E(\boldsymbol{\sigma}_1 \otimes \mathbf{1}_2) \cdot \hat{\mathbf{z}}(\mathbf{1}_1 \otimes \boldsymbol{\sigma}_2) \cdot \hat{\mathbf{z}} \\ &\quad + i|\mathbf{q}|C(\boldsymbol{\sigma}_1 \otimes \mathbf{1}_2 + \mathbf{1}_1 \otimes \boldsymbol{\sigma}_2) \cdot \hat{\mathbf{n}} + |\mathbf{q}|^2D(\boldsymbol{\sigma}_1 \otimes \mathbf{1}_2) \cdot \hat{\mathbf{q}}(\mathbf{1}_1 \otimes \boldsymbol{\sigma}_2) \cdot \hat{\mathbf{q}}.\end{aligned}\tag{3.4.20}$$

The orthonormal directions  $\hat{\mathbf{q}}$ ,  $\hat{\mathbf{z}}$  and  $\hat{\mathbf{n}}$  are defined in terms of initial and final centre of mass momenta,  $\mathbf{k}_c$  and  $\mathbf{k}'_c$  of a nucleons,

$$\begin{aligned}\hat{\mathbf{q}} &= \frac{\mathbf{k}'_c - \mathbf{k}_c}{|\mathbf{k}'_c - \mathbf{k}_c|}, \\ \hat{\mathbf{z}} &= \frac{\mathbf{k}_c + \mathbf{k}'_c}{|\mathbf{k}_c + \mathbf{k}'_c|}\end{aligned}\tag{3.4.21}$$

and

$$\hat{\mathbf{n}} = \frac{\mathbf{k}'_c \times \mathbf{k}_c}{|\mathbf{k}'_c \times \mathbf{k}_c|}.\tag{3.4.22}$$

The amplitudes A, B, C, D and E are each complex functions of the three momenta transfer  $|\mathbf{q}| = |\mathbf{k}'_c - \mathbf{k}_c|$  and the collisional energy  $E_c = \sqrt{|\mathbf{k}_c|^2 + M^2}$ . These coefficients are calculated from nucleon-nucleon phase shift analyses [102].

It is well known that the nucleon-nucleon interaction is charge independent, i.e. isoscalar (isospin invariant). We require the  $\tau$ -operator to be isospin dependent constructed out of isospin operators  $\mathcal{I}_1$  and  $\mathcal{I}_2$ . Then it follows the substitution of isospin dependence of amplitudes,

$$A = A_0 + A_1\mathcal{I}_1 \cdot \mathcal{I}_2, \quad B = B_0 + B_1\mathcal{I}_1 \cdot \mathcal{I}_2, \dots\tag{3.4.23}$$

The  $U$ 's are the free-particle four-component positive-energy of the Dirac spinor, normalized such that  $\bar{U}U=1$ ;

$$\bar{U}(\mathbf{k}_c, s) = U^\dagger(\mathbf{k}_c, s)\gamma^0, \quad \gamma^0 = \begin{pmatrix} \mathbf{1} & 0 \\ 0 & -\mathbf{1} \end{pmatrix},\tag{3.4.24}$$

$$U(\mathbf{k}_c, s) = \mathcal{M}(\mathbf{k}_c, s) \begin{pmatrix} \chi^s \\ 0 \end{pmatrix}\tag{3.4.25}$$

and

$$\mathcal{M}(\mathbf{k}_c, s) = \left[ \frac{E_c + M}{2M} \right]^{1/2} \begin{pmatrix} \mathbf{1} & \frac{\boldsymbol{\sigma} \cdot \mathbf{k}_c}{E_c + M} \\ \frac{\boldsymbol{\sigma} \cdot \mathbf{k}_c}{E_c + M} & \mathbf{1} \end{pmatrix}.\tag{3.4.26}$$

With this choice of the amplitudes  $F^{Ll}$ s, we are allowed to write the right hand side of equation 3.4.19 as a sum of five terms:

$$\chi_{s'_1}^\dagger \otimes \chi_{s'_2}^\dagger \tau_{NN}(E_c, |\mathbf{q}|) \chi_{s_1} \otimes \chi_{s_2} = \sum_L F^L(E_c, |\mathbf{q}|) \left( \bar{U}_{s'_1} \lambda_{(1)L}^L U_{s_1} \right) \otimes \left( \bar{U}_{s'_2} \lambda_{(2)L} U_{s_2} \right). \quad (3.4.27)$$

In this way, the amplitudes  $\{F^S, F^V, F^P, F^A, F^T\}$  are expressed as linear combinations of the Wolfenstein amplitudes  $\{A, B, C, D, E\}$  or vice versa. We conclude that there is a non-singular  $5 \times 5$  matrix,  $\mathcal{O}(E_c, |\mathbf{k}_c|, |\mathbf{q}|)$  which transforms the Wolfenstein amplitudes (centre-of-mass) into invariants  $F^L$  [102],

$$\begin{pmatrix} A \\ B \\ C \\ D \\ E \end{pmatrix} = \begin{pmatrix} & & & & \\ & \mathcal{O}(E_c, |\mathbf{k}_c|, |\mathbf{q}|) & & & \\ & & & & \\ & & & & \\ & & & & \end{pmatrix} \begin{pmatrix} F^S \\ F^V \\ F^T \\ F^P \\ F^A \end{pmatrix}. \quad (3.4.28)$$

In the original RIA, the interaction is considered to be between free nucleons. This will be valid for intermediate and higher energies. For the sake of a successful relativistic cluster-core potential, we will propose a model of interaction applied over a wide range of energies. We have to emphasize that the parametrization addressed above, (*MRW*) does not include the non-localities due to exchange behaviour in the nuclear medium. The following section will be devoted to the analyses of these shortcomings.

It has been realized that the exchange effects induced by non-localities are predominant at lower energies. In contrast to the original Relativistic Impulse Approximation (RIA) introduced before, an alternative invariant nucleon-nucleon  $\tilde{\tau}$ -operator, based on the relativistic meson-exchange diagrams referred to as the **Relativistic, Love, Franey (RLF)** model [59, 60] has been proposed. This parametrization contains a complex phenomenological coupling constant with  $p\nu\pi N$  coupling, including direct and exchange terms explicitly which may be worth sketching in figure 3.2. The attempt to parametrize in terms of one-meson-exchange of various Lorentz types (**S**, **V**, **P**, **A**, **T**) and isospins is to

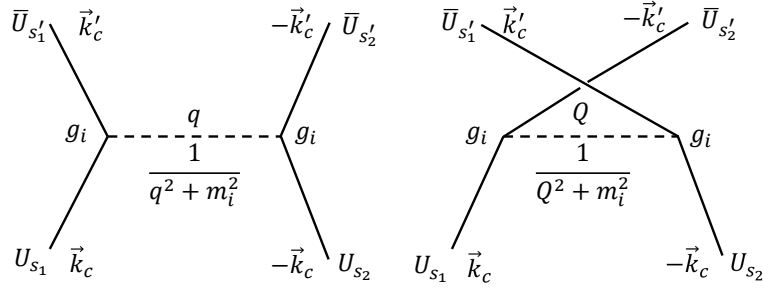


**Figure 3.2:** Relativistic direct and exchange one-meson diagrams for the Love-Franey model.

write down the right hand side of equation 3.4.27 as

$$\begin{aligned}
 & \sum_L F^L(E_c, |\mathbf{q}|) \left( \bar{U}_{s_1'} \lambda_{(1)}^L U_{s_1} \right) \otimes \left( \bar{U}_{s_2'} \lambda_{(2)L} U_{s_2} \right) \\
 &= \sum_L F_D^L(E_c, |\mathbf{q}|) \left( \bar{U}_{s_1'} \lambda_{(1)}^L U_{s_1} \right) \otimes \left( \bar{U}_{s_2'} \lambda_{(2)L} U_{s_2} \right) \\
 &+ \sum_L F_{EX}^L(E_c, |\mathbf{q}|) \left( \bar{U}_{s_2'} \lambda_{(2)L} U_{s_1} \right) \otimes \left( \bar{U}_{s_1'} \lambda_{(1)}^L U_{s_2} \right)
 \end{aligned} \tag{3.4.29}$$

where  $F_D^L$  and  $F_{EX}^L$  are direct and exchange nucleon-nucleon one-meson-exchange terms.

The exchange matrix element in equation 3.4.29 is transformed following the Fiertz transformation [59, 60],

$$\begin{aligned}
 F_{EX}^L(E_c, |\mathbf{q}|) \left( \bar{U}_{s_2'} \lambda_{(2)L} U_{s_1} \right) \otimes \left( \bar{U}_{s_1'} \lambda_{(1)}^L U_{s_2} \right) &= \sum_{L'} F_{EX}^{L'}(E_c, |\mathbf{q}|) \times \\
 & C_{LL'} \left( \bar{U}_{s_1'} \lambda_{(1)}^{L'} U_{s_1} \right) \otimes \left( \bar{U}_{s_2'} \lambda_{(2)L'} U_{s_2} \right).
 \end{aligned} \tag{3.4.30}$$

Using this equation, we obtain the L's type amplitude from equation 3.4.29,

$$F^L(E_c, |\mathbf{q}|) = F_D^L(E_c, |\mathbf{q}|) + \sum_{L'} C_{LL'} F_{EX}^L(E_c, |\mathbf{Q}|) \tag{3.4.31}$$

where  $C_{LL'}$  is a  $5 \times 5$  Fiertz's matrix ,

$$C_{LL'} = \frac{1}{8} \begin{pmatrix} 2 & 2 & 1 & -2 & 2 \\ 8 & -4 & 0 & -4 & -8 \\ 24 & 0 & -4 & 0 & 24 \\ -8 & -4 & 0 & -4 & 8 \\ 2 & -2 & 1 & 2 & 2 \end{pmatrix} \quad (3.4.32)$$

with rows and columns labelled in the order  $(\mathbf{S}, \mathbf{V}, \mathbf{T}, \mathbf{A}, \mathbf{P})$ .

Next we would like to give an explicit form of the direct and the exchange terms,  $F_D^L$  and  $F_{EX}^L$  involved in the total amplitude  $F^L(E_{cm}, |\mathbf{q}|)$ .

In the nonrelativistic limit of the free spinors, the mesons have a propagator of the form,

$$\frac{1}{|\mathbf{q}|^2 + m^2}. \quad (3.4.33)$$

For the meson-nucleon vertices, the form factors are of the form

$$\left(1 + \frac{|\mathbf{q}|^2}{\Lambda^2}\right)^{-1}. \quad (3.4.34)$$

Finally, using the Feynmann rules within the diagrams given in figure 3.2, the nucleon-nucleon-meson vertex factor is assumed to be

$$g_i \left(1 + \frac{|\mathbf{q}|^2}{\Lambda^2}\right)^{-1} \lambda^{L(i)}(\mathcal{I})^{T_i}. \quad (3.4.35)$$

This takes into account the isospin states of the two nucleons system ( $\mathcal{I} = 0, 1$ ). Here  $L(i)$  stands for the Lorentz type of the  $i$ th meson  $(\mathbf{S}, \mathbf{V}, \mathbf{P}, \mathbf{A}, \mathbf{T})$  and  $T_i = (0, 1)$  is the meson's isospin.

Thus the contribution of the meson  $i$  to the amplitude  $F^i$  up to an overall kinetic factor will read

$$\begin{aligned} (\bar{U}_{s'_1} \otimes \bar{U}_{s'_2}) F^i (U_{s_1} \otimes U_{s_2}) &\propto \frac{g_i^2}{m_i^2 + q^2} \left(1 + \frac{q^2}{\Delta_i^2}\right)^{-2} (\bar{U}_{s'_1} \lambda_{(1)}^{L(i)} U_{s_1}) \otimes (\bar{U}_{s'_2} \lambda_{(2)L(i)} U_{s_2}) \{\mathcal{I}_1 \cdot \mathcal{I}_2\}^{T_i} + \\ &(-1)^{\mathcal{I}} \frac{g_i^2}{m_i^2 + Q^2} \left(1 + \frac{Q^2}{\Delta_i^2}\right)^{-2} \sum_{L'} C_{L(i), L'} (\bar{U}_{s'_1} \lambda_{(1)}^{L'} U_{s_1}) \otimes (\bar{U}_{s'_2} \lambda_{(2)L'} U_{s_2}) \\ &\quad \times \{\mathcal{I}_1 \cdot \mathcal{I}_2\}^{T_i} \end{aligned} \quad (3.4.36)$$

Following the ansatz described in [59], the amplitude  $F^L$  is expressed as

$$F^L = i \frac{M^2}{2k_c E_c} \left[ F_D^L(q) + F_{EX}^L(Q) \right]; \quad (3.4.37)$$

where  $q = |\mathbf{q}|$  and  $Q = |\mathbf{Q}|$  are the direct and exchange momenta transfer in the centre of mass for the scattering angle  $\theta_c$

$$q = 2k_c \sin\left(\frac{\theta_c}{2}\right), \quad Q = 2k_c \sin\left(\pi - \frac{\theta_c}{2}\right). \quad (3.4.38)$$

The direct and exchange terms,  $F_D^L$  and  $F_{EX}^L$  are given by

$$F_D^L(q) = \sum_{i=1}^N \delta_{L,L(i)} \{\mathcal{I}_1 \cdot \mathcal{I}_2\}^{T_i} f^i(q) \quad (3.4.39)$$

and

$$F_{EX}^L(Q) = (-1)^{\mathcal{I}} \sum_{i=1}^N C_{L(i),L} \{\mathcal{I}_1 \cdot \mathcal{I}_2\}^{T_i} f^i(Q). \quad (3.4.40)$$

In these cases  $N$  represents the number of mesons used in the fit, and  $\mathcal{I}$  is the nucleon-nucleon total isospin.

The Lorentz invariants amplitudes for  $pp$ ,  $nn$ ,  $pn$  and  $np$  are:

$$\begin{aligned} F_i(pp) &\equiv F_i(nn) = F_i(\mathcal{I} = 1) \\ F_i(pn) &\equiv F_i(np) = \frac{1}{2} [F_i(\mathcal{I} = 1) + F_i(\mathcal{I} = 0)] \end{aligned} \quad (3.4.41)$$

The contribution to amplitudes brought by  $\{\mathcal{I}_1 \cdot \mathcal{I}_2\}^{T_i}$  for each nucleon-nucleon isospin is:

for  $\mathcal{I} = 0$

$$\{\mathcal{I}_1 \cdot \mathcal{I}_2\}^{T_i} = \begin{cases} 1 & \text{for the exchange of } T_i = 0 \text{ (isoscalar) mesons} \\ -3 & \text{for the exchange of } T_i = 1 \text{ (isoscalar) mesons} \end{cases} \quad (3.4.42)$$

and for  $\mathcal{I} = 1$

$$\{\mathcal{I}_1 \cdot \mathcal{I}_2\}^{T_i} = \begin{cases} 1 & \text{for the exchange of } T_i = 0 \text{ (isoscalar) mesons} \\ 1 & \text{for the exchange of } T_i = 1 \text{ (isoscalar) mesons} \end{cases}. \quad (3.4.43)$$

The function  $f^i(q)$ 's or  $f^i(Q)$ 's are written as a sum of real and imaginary terms,

$$f^i(q) = f_R^i(q) - i f_I^i(q), \quad f^i(Q) = f_R^i(Q) - i f_I^i(Q) \quad (3.4.44)$$

$$f_R^i(q) = \frac{g_i^2}{q^2 + m_i^2} \left(1 + \frac{q^2}{2\Lambda_i^2}\right)^{-2}, \quad f_R^i(Q) = \frac{g_i^2}{Q^2 + m_i^2} \left(1 + \frac{Q^2}{2\Lambda_i^2}\right)^{-2} \quad (3.4.45)$$

$$f_I^i(q) = \frac{\bar{g}_i^2}{q^2 + \bar{m}_i^2} \left(1 + \frac{q^2}{2\bar{\Lambda}_i^2}\right)^{-2}, \quad f_I^i(Q) = \frac{\bar{g}_i^2}{Q^2 + \bar{m}_i^2} \left(1 + \frac{Q^2}{2\bar{\Lambda}_i^2}\right)^{-2}. \quad (3.4.46)$$

The real and imaginary meson masses  $m_i$ ,  $\bar{m}_i$ , coupling constants  $g_i^2$ ,  $\bar{g}_i^2$  and cut-off parameters  $\Lambda_i$ ,  $\bar{\Lambda}_i$  are calculated from fitting methods [59, 60].

Furthermore, we require a set of new (**RLF**) parameters consistent with the one-meson exchange model for the lower energies [103]. This will include the energy-dependent Maxwell parametrization [104].

### 3.4.4 Effective Nucleon and Meson Masses

In the **Relativistic Mean Field Theory (RMFT)** of the Walecka model [105], the mass of a nucleon embedded in the nucleus differs from its mass in free space. This yields the concept of effective masses for both cluster and core nucleons,  $M_1^*$  and  $M_2^*$  respectively. These effective masses arise from the interactions of nucleons with the surrounding nucleons in the nuclear medium. This interaction is through an attractive scalar potential  $S$ . However from the **RMFT**, the effective nucleon mass is related to its free mass by

$$M^* = M + \langle S \rangle, \quad (3.4.47)$$

where  $\langle S \rangle$  is the mean value of scalar field experienced by either a nucleon in the cluster or in the core as it propagates through the nuclear medium.

In our cluster model, we will use the scaling law developed by Brown *et al* [106]. The inclusion of medium effects to the nucleon-nucleon interaction is done by replacing the free nucleon and real meson masses along with meson coupling constants by their respective medium modified values according to

$$\frac{M^*}{M} = \frac{m_\sigma^*}{m_\sigma} = \frac{m_\rho^*}{m_\rho} = \frac{m_\omega^*}{m_\omega} = \dots = \xi \quad (3.4.48)$$

and

$$\frac{g_{\sigma NN}^*}{g_{\sigma NN}} = \frac{g_{\omega NN}^*}{g_{\omega NN}} = \chi. \quad (3.4.49)$$

The approximative values of  $\xi$  and  $\chi$  are taken from [107], which are 0.70 and 0.75, respectively.

### 3.4.5 Construction of the Potential

Throughout this thesis, we have adopted the first order potential in agreement with the single scattering approximation. The relativistic cluster-core potential is evaluated starting from equation 3.4.15. This is constructed by taking the dual ground state expectation value of  $\tilde{\tau}$  between the initial and final internal

wave function of the cluster and core. We make an assumption that the cluster and core nucleons are identical particles so that

$$\hat{U} = A_1 A_2 \left\langle \bar{\phi}_0^{A_1} \otimes \bar{\phi}_0^{A_2} \left| \tilde{\tau} \right| \phi_0^{A_1} \otimes \phi_0^{A_2} \right\rangle \quad (3.4.50)$$

where the operator  $\tilde{\tau}$  is any one of the  $\tilde{\tau}_{ij}$  parametrized either by the RIA, equations 3.4.18 or the RLF models 3.4.31. Basically, our model requires the Love-Franey amplitude described above. Since the model contains both direct and exchange parts, the cluster-core potential is the sum of the direct term which looks like

$$\hat{U}_D = A_1 A_2 \left\langle \bar{\phi}_0^{A_1} \otimes \bar{\phi}_0^{A_2} \left| \tilde{\tau}_D \right| \phi_0^{A_1} \otimes \phi_0^{A_2} \right\rangle \quad (3.4.51)$$

and the exchange term, which is the antisymmetrized matrix element

$$\hat{U}_{EX} = A_1 A_2 \left\langle \bar{\phi}_0^{A_1} \otimes \bar{\phi}_0^{A_2} \left| \tilde{\tau}_{EX} \right| \phi_0^{A_2} \otimes \phi_0^{A_1} \right\rangle. \quad (3.4.52)$$

However, compared with the non-relativistic double folded potential described in chapter 3, here more details should be given when deriving the relativistic nucleus-nucleus potential and yet the principle remains similar.

Hence, to this end, the relativistic ground state vector  $|\phi_0^A\rangle$  can be expanded in terms of the basis vectors formed from the eigenstate of an individual particle. This is constructed out of the direct product basis,  $|r_1, \dots, r_A\rangle = |r_1\rangle \otimes \dots \otimes |r_A\rangle$ ;

$$|\phi_0^A\rangle = \int d\mathbf{r}_1 \dots \int d\mathbf{r}_A |\mathbf{r}_1; \dots; \mathbf{r}_A\rangle \langle \mathbf{r}_1; \dots; \mathbf{r}_A | \phi_0^A \rangle. \quad (3.4.53)$$

Here  $|\mathbf{r}\rangle \equiv |\mathbf{x}, \alpha\rangle$ , where  $\alpha$  is a set of quantum numbers characterizing a Dirac single particle orbital such that

$$\alpha = \{n, l, j, m_j, m_{\mathcal{I}}\} \quad (3.4.54)$$

with  $n$  (radial),  $l$  (orbital angular momentum),  $j$  (total angular momentum),  $m_j$  (z component of the total angular momentum), and  $m_{\mathcal{I}}$  (isospin projection). The wave function  $\langle \mathbf{r}_1, \dots, \mathbf{r}_A | \phi_0^A \rangle$  is taken to be a relativistic antisymmetrized nuclear wave function in the independent particle model and it is represented by a Slater determinant

$$\begin{aligned} \langle \mathbf{r}_1, \dots, \mathbf{r}_A | \phi_0^A \rangle &= \Phi_0^A(\mathbf{r}_1 \dots \mathbf{r}_A) \\ &= \frac{1}{\sqrt{A!}} \sum_P (-1)^P \prod_i^A \psi_{\alpha_i}(\mathbf{r}_{Pi}) \end{aligned} \quad (3.4.55)$$



where  $P$  summes over all permutations. And

$$\psi_\alpha(\mathbf{r}) = i \begin{pmatrix} G_{nljm_\mathcal{I}}(r) \\ -i\boldsymbol{\sigma} \cdot \hat{\mathbf{r}} F_{nljm_\mathcal{I}}(r) \end{pmatrix} \mathcal{Y}_{l_j}^{m_j}(\hat{\mathbf{r}}) \quad (3.4.56)$$

is a four-component single particle orbital solution of the Dirac equation with scalar and vector potentials as we shall see later.

If we make use of the completeness relation defined in equation 3.4.53, the cluster-core direct potential, which is defined in equation 3.4.51, becomes,

$$\begin{aligned} \hat{U}_D = A_1 A_2 \int d\mathbf{r}_1 \cdots \int d\mathbf{r}_{A_1} \int d\mathbf{r}'_1 \cdots \int d\mathbf{r}'_{A_1} \int d\mathbf{r}'_{1'} \cdots \int d\mathbf{r}'_{A_2} \int d\mathbf{r}'_{1'} \cdots \int d\mathbf{r}'_{A_2} \\ \langle \bar{\phi}_0^{A_1} | \mathbf{r}_1 \cdots \mathbf{r}_{A_1} \rangle \otimes \langle \bar{\phi}_0^{A_2} | \mathbf{r}'_1 \cdots \mathbf{r}'_{A_2} \rangle \\ \langle \mathbf{r}_1 \cdots \mathbf{r}_{A_1} \otimes \mathbf{r}'_1 \cdots \mathbf{r}'_{A_1} | \tilde{\tau}_D | \mathbf{r}'_{1'} \cdots \mathbf{r}'_{A_1} \otimes \mathbf{r}'_{1'} \cdots \mathbf{r}'_{A_2} \rangle \\ \langle \mathbf{r}'_{1'} \cdots \mathbf{r}'_{A_1} | \phi_0^{A_1} \rangle \otimes \langle \mathbf{r}'_{1'} \cdots \mathbf{r}'_{A_2} | \phi_0^{A_2} \rangle \end{aligned} \quad (3.4.57)$$

We use the orthonormality condition to write the matrix elements representation of the operator  $\tilde{\tau}$ ,

$$\begin{aligned} \langle \mathbf{r}_1 \cdots \mathbf{r}_{A_1} \otimes \mathbf{r}'_1 \cdots \mathbf{r}'_{A_1} | \tilde{\tau} | \mathbf{r}'_{1'} \cdots \mathbf{r}'_{A_1} \otimes \mathbf{r}'_{1'} \cdots \mathbf{r}'_{A_2} \rangle = \\ \tilde{\tau}_D(\mathbf{r}_1, \mathbf{r}'_1) \delta(\mathbf{r}_1 - \mathbf{r}'_{1'}) \cdots \delta(\mathbf{r}_{A_1} - \mathbf{r}'_{A_1}) \otimes \\ \delta(\mathbf{r}'_1 - \mathbf{r}'_{1'}) \cdots \delta(\mathbf{r}'_{A_2} - \mathbf{r}'_{A_2}). \end{aligned} \quad (3.4.58)$$

Hence, the equation 3.4.57 becomes

$$\begin{aligned} \hat{U}_D = A_1 A_2 \int d\mathbf{r}_1 \cdots \int d\mathbf{r}_{A_1} \int d\mathbf{r}'_1 \cdots \int d\mathbf{r}'_{A_2} \times \\ \bar{\Phi}^{A_1}(\mathbf{r}_1 \cdots \mathbf{r}_{A_1}) \otimes \bar{\Phi}^{A_2}(\mathbf{r}'_1 \cdots \mathbf{r}'_{A_2}) \tilde{\tau}_D(\mathbf{r}_1, \mathbf{r}'_1) \times \\ \Phi^{A_1}(\mathbf{r}_1 \cdots \mathbf{r}_{A_1}) \otimes \Phi^{A_2}(\mathbf{r}'_1 \cdots \mathbf{r}'_{A_2}). \end{aligned} \quad (3.4.59)$$

Substituting either the direct part of the RLF amplitude or the RIA, equation 3.4.59 becomes

$$\begin{aligned} \hat{U}_D = A_1 A_2 \int d\mathbf{r}_1 \cdots \int d\mathbf{r}_{A_1} \int d\mathbf{r}'_1 \cdots \int d\mathbf{r}'_{A_2} \times \\ \bar{\Phi}^{A_1}(\mathbf{r}_1 \cdots \mathbf{r}_{A_1}) \otimes \bar{\Phi}^{A_2}(\mathbf{r}'_1 \cdots \mathbf{r}'_{A_2}) \left( \sum_{L=S}^T \mathcal{T}_D^L(\mathbf{r}_1, \mathbf{r}'_1) \lambda_{(1)}^L \otimes \lambda_{(2)L} \right) \times \\ \Phi^{A_1}(\mathbf{r}_1 \cdots \mathbf{r}_{A_1}) \otimes \Phi^{A_2}(\mathbf{r}'_1 \cdots \mathbf{r}'_{A_2}). \end{aligned} \quad (3.4.60)$$

And using the identity  $(A \otimes B)(C \otimes D) = (AC) \otimes (BD)$ , we obtain

$$\hat{U}_D = A_1 A_2 \int d\mathbf{r}_1 \cdots \int d\mathbf{r}_{A_1} \int d\mathbf{r}'_1 \cdots \int d\mathbf{r}'_{A_2} \sum_{L=S}^T \mathcal{T}_D^L(\mathbf{r}_1, \mathbf{r}'_1) \times \left[ \bar{\Phi}^{A_1}(\mathbf{r}_1 \cdots \mathbf{r}_{A_1}) \lambda_{(1)}^L \Phi^{A_1}(\mathbf{r}_1 \cdots \mathbf{r}_{A_1}) \right] \otimes \left[ \bar{\Phi}^{A_2}(\mathbf{r}'_1 \cdots \mathbf{r}'_{A_2}) \lambda_{(2)L} \Phi^{A_2}(\mathbf{r}'_1 \cdots \mathbf{r}'_{A_2}) \right] \quad (3.4.61)$$

We therefore insert the antisymmetrized nuclear wave function defined in equation 3.4.55 into 3.4.61, to obtain the direct double folded potential similar to the nonrelativistic case

$$U_D(\mathbf{r}) = A_1 A_2 \sum_L \int \int \tau_D^L(\mathbf{s}) \left( \sum_{i=1}^{A_1} \frac{(A_1 - 1)!}{A_1!} \bar{\psi}_{\alpha_i}(\mathbf{r}_1) \lambda_{(1)}^L \psi_{\alpha_i}(\mathbf{r}_1) \right) \otimes \left( \sum_{j=1}^{A_2} \frac{(A_2 - 1)!}{A_2!} \bar{\psi}_{\beta_j}(\mathbf{r}'_2) \lambda_{(2)L} \psi_{\beta_j}(\mathbf{r}'_2) \right) d\mathbf{r}_1 d\mathbf{r}'_2 \quad (3.4.62)$$

$$= \sum_L \int \int \mathcal{T}_D^L(\mathbf{s}) \rho_{(1)}^L(\mathbf{r}_1) \otimes \rho_{(2)L}(\mathbf{r}'_2) d\mathbf{r}_1 d\mathbf{r}'_2,$$

where  $\mathbf{s} = \mathbf{r} - \mathbf{r}_1 + \mathbf{r}'_2$ .

The densities  $\rho^L(\mathbf{r}_1) \propto \bar{\psi}_{\alpha_i}(\mathbf{r}_1) \lambda_{(1)}^L \psi_{\alpha_i}(\mathbf{r}_1)$  are complex numbers, so one may write

$$U_D(\mathbf{r}) = \sum_L U_D^L(\mathbf{r}) \quad (3.4.63)$$

where,

$$U_D^L(\mathbf{r}) = \int \int \mathcal{T}_D^L(\mathbf{s}) \rho_{(1)}^L(\mathbf{r}_1) \rho_{(2)L}(\mathbf{r}'_2) d\mathbf{r}_1 d\mathbf{r}'_2. \quad (3.4.64)$$

For the exchange term, we apply to the antisymmetrized matrix element of equation 3.4.52 the same closure relation as done before with the direct term.

We end up with the non-local term,

$$U_{EX}(\mathbf{r}) = \sum_L \int \int \mathcal{T}_{EX}^L(\mathbf{s}) \left( \sum_{i=1}^{A_1} \bar{\psi}_{\alpha_i}(\mathbf{r}_1) \lambda_{(1)}^L \psi_{\alpha_i}(\mathbf{r}'_2) \right) \otimes \left( \sum_{j=1}^{A_2} \bar{\psi}_{\beta_j}(\mathbf{r}'_2) \lambda_{(2)L} \psi_{\beta_j}(\mathbf{r}_1) \right) d\mathbf{r}_1 d\mathbf{r}'_2 \quad (3.4.65)$$

$$= \sum_L \int \int \mathcal{T}_{EX}^L(\mathbf{s}) \rho_{(1)}^L(\mathbf{r}_1, \mathbf{r}'_2) \rho_{(2)L}(\mathbf{r}'_2, \mathbf{r}_1) d\mathbf{r}_1 d\mathbf{r}'_2.$$

This exchange term which has a form  $\mathcal{T}_{EX}^L(\mathbf{s})\rho_{(1)}^L(\mathbf{r}_1, \mathbf{r}'_2)\rho_{(2)L}(\mathbf{r}'_2, \mathbf{r}_1)$  has to be approximated with a suitable local potential form. In essence, the local potential had been achieved by using a plane wave approximation method of refs. [83, 93, 95, 108] in the nonrelativistic case. a similar approach can be applied to the relativistic cluster-core potential of interest which results to

$$U_{EX}(\mathbf{r}) = \sum_L \int \int \mathcal{T}_{EX}^L(\mathbf{s})\rho_{(1)}^L(\mathbf{r}_1, \mathbf{r}_1 + \mathbf{s})\rho_{(2)L}(\mathbf{r}'_2, \mathbf{r}'_2 - \mathbf{s}) \text{Exp}\left(\frac{i\mathbf{K}(\mathbf{r}) \cdot \mathbf{s}}{\mu}\right) d\mathbf{r}_1 d\mathbf{r}'_2 \quad (3.4.66)$$

where  $\mathbf{K}(\mathbf{r})$  is the local wave number that has to be approximated into the momentum P, calculated in the centre of mass system rather than taking the calculated value at the midpoint between  $\mathbf{r}_1$  and  $\mathbf{r}'_1$ , i.e. at  $\mathbf{R} = (\mathbf{r}_1 + \mathbf{r}'_2)/2$  as in the non-relativistic case.

The remaining thing to do is to find a local relativistic nuclear matter approximation for the mixed densities  $\rho^L(\mathbf{r}_1, \mathbf{r}_1 + \mathbf{s})$ . We have to choose the realistic local expression for the density matrix suggested by [95] which is equivalent to its relativistic counterpart,

$$\begin{aligned} \rho_{(1)}^L(\mathbf{r}_1, \mathbf{r}_1 + \mathbf{s}) &\simeq \rho_{(1)}^L\left(\mathbf{r}_1 + \frac{\mathbf{s}}{2}\right)\hat{j}_1\left(K_{F_1}\left(\mathbf{r}_1 + \frac{\mathbf{s}}{2}\right)s\right) \\ \rho_{2L}(\mathbf{r}'_2, \mathbf{r}'_2 - \mathbf{s}) &\simeq \rho_{(2)L}\left(\mathbf{r}'_2 - \frac{\mathbf{s}}{2}\right)\hat{j}_1\left(K_{F_2}\left(\mathbf{r}'_2 - \frac{\mathbf{s}}{2}\right)s\right) \end{aligned} \quad (3.4.67)$$

where  $\hat{j}_1(x) = 3(\sin x - x \cos x)/x^3$ . The Fermi momentum  $K_F$  is related to the diagonal element of the baryon density  $\rho^B(\mathbf{r})$  in the Slater approximation for the infinite nuclear matter [94, 95], by

$$K_F^2(\mathbf{r}) = \left[\frac{3\pi^2}{2}\rho^B(\mathbf{r})\right]^{2/3}. \quad (3.4.68)$$

However, it should be noted that in the extended Thomas-Fermi approximation [94], we have

$$K_{eff}^2(\mathbf{r}) = \left[\left(\frac{3\pi^2}{2}\rho^B(\mathbf{r})\right)^{2/3} + \frac{5C_s|\nabla\rho^B(\mathbf{r})|^2}{3(\rho^B(\mathbf{r}))^2} + \frac{5\nabla^2\rho^B(\mathbf{r})}{36\rho^B(\mathbf{r})}\right]. \quad (3.4.69)$$

An appropriate coordinates transformation along with the local approximation defined above in equation 3.4.67 will allow us to write the exchange potential

as

$$\begin{aligned}
 U_{EX}(\mathbf{r}) &= \sum_L \int \int \mathcal{T}_{EX}^L(s) \rho_{(1)}^L(\mathbf{r}) \hat{j}_1(K_{F_1}(\mathbf{r})s) \rho_{(2)L}(\mathbf{r} - \mathbf{r}') \hat{j}_1(K_{F_2}(\mathbf{r} - \mathbf{r}')s) \\
 &\quad \text{Exp}\left(\frac{i\mathbf{K}(\mathbf{r}) \cdot \mathbf{s}}{\mu}\right) d\mathbf{s} d\mathbf{r}' \\
 &= \sum_L \int \int \mathcal{T}_{EX}^L(s) \rho_{(1)}^L(\mathbf{r}') \hat{j}_1(K_{F_1}(\mathbf{r}')s) \rho_{(2)L}(\mathbf{r}' - \mathbf{r}) \hat{j}_1(K_{F_2}(\mathbf{r}' - \mathbf{r})s) \times \\
 &\quad j_0\left(\frac{K(\mathbf{r})s}{\mu}\right) d\mathbf{s} d\mathbf{r}'.
 \end{aligned} \tag{3.4.70}$$

Finally, by taking into account the isospin dependence of the system, the coordinate space position of the cluster-core potential is calculated from

$$\begin{aligned}
 U(\mathbf{r}) &= \sum_L \left( U_D^L(\mathbf{r}) + U_{EX}^L(\mathbf{r}) \right) \\
 &= \sum_{i=n_1, p_1} \sum_{j=n_2, p_2} \sum_L \int \int \mathcal{T}_{D,ij}^L(\mathbf{s}) \rho_{(i)}^L(\mathbf{r}_1) \rho_{(j)L}(\mathbf{r}'_2) d\mathbf{r}_1 d\mathbf{r}'_2 + \\
 &\quad \sum_{i=n_1, p_1} \sum_{j=n_2, p_2} \sum_{L, L'} \int \int \mathcal{T}_{EX,ij}^{L'}(s) C_{L',L} h_i^L(\mathbf{r}, s) h_{(j)L}(\mathbf{r}' - \mathbf{r}, s) \times \\
 &\quad j_0\left(\frac{K(\mathbf{r})s}{\mu}\right) d\mathbf{s} d\mathbf{r}'
 \end{aligned} \tag{3.4.71}$$

with

$$\mathcal{T}_{D,(EX)}^L(s) = -i \frac{4\pi P c}{\mu c^2} \left( \frac{iM^2 c^4}{2E_c P c c} \right) \int_0^\infty \frac{d^3 \mathbf{q}}{(2\pi)^3} e^{i\mathbf{q} \cdot \mathbf{s}} F_{D(EX)}^L(\mathbf{q}), \tag{3.4.72}$$

$$h_i^L(\mathbf{r}, s) = \rho_{(i)}^L(\mathbf{r}) \hat{j}_1(K_{F_i}(\mathbf{r})s) \tag{3.4.73}$$

and

$$h_{(j)L}(\mathbf{r} - \mathbf{r}', s) = \rho_{(j)L}(\mathbf{r} - \mathbf{r}') \hat{j}_1(K_{F_j}(\mathbf{r} - \mathbf{r}')s). \tag{3.4.74}$$

$\mu$ ,  $M$  and  $P$  are the reduced mass, nucleon masses and the cluster's momentum calculated in the centre of mass of the system.

In the last step of equation 3.4.71, we have used the Fierz transformation.

We follow the kinematics described in [60]. Here we have a single composite particle cluster instead of a proton. This is an intuitive way we have taken in order to adjust the depth of the potential.

## 3.5 Relativistic Nuclear Densities

In order to construct the cluster-core potential, nuclear densities calculated from relativistic quantum field theory are needed. The model is based on the Relativistic Mean Field Theory (RMFT) developed by Walecka [105], the so-called QHD-I model, the extended QHD-II introduced by Serot [109–112], and other extensions such as NL3 [113] and FSU [114–116]. These models provide a very successful tool for a covariant description of nuclear matter. The theory is able to give a quantitative description of ground-state properties for spherical and deformed nuclei.

### 3.5.1 Relativistic Mean Field Theory

The relativistic nuclear many-body problem is studied using quantum hydrodynamics in the framework of quantum field theory. A particular renormalizable Lagrangian density has to be considered in order to include medium effects in more fundamental way. This means, imposing constraints that ensure a well-defined computational and the dynamics procedure to all orders in the coupling strengths and meson masses.

The starting point is the Lagrangian density where nucleons are described as Dirac particles which interact via the exchange of various mesons. It is expressed as a sum of non-interacting and interacting terms such that

$$\mathcal{L} = \mathcal{L}_0 + \mathcal{L}_{int}. \quad (3.5.1)$$

The Lagrangian density  $\mathcal{L}_0$ , describing particles in free space, is given by

$$\begin{aligned} \mathcal{L}_0 = & \bar{\Psi} \left( i\gamma_\mu \partial^\mu - M \right) \Psi + \frac{1}{2} \left( \partial_\mu \phi \partial^\mu \phi - m_s^2 \phi^2 \right) - \frac{1}{4} V_{\mu\nu} V^{\mu\nu} + \frac{1}{2} m_v^2 V_\mu V^\mu \\ & - \frac{1}{4} \mathbf{b}_{\mu\nu} \cdot \mathbf{b}^{\mu\nu} + \frac{1}{2} m_\rho^2 \mathbf{b}_\mu \cdot \mathbf{b}^\mu - \frac{1}{4} F_{\mu\nu} F^{\mu\nu}. \end{aligned} \quad (3.5.2)$$

Here  $\Psi$  is the isodoublet-nucleon field.  $\phi$ ,  $V_\mu$  and  $b_\mu$  represent the isoscalar-scalar  $\sigma$ -meson, isoscalar-vector  $\omega$ -meson, and isovector-vector  $\rho$ -meson fields respectively. The parameters  $M$ ,  $m_s$ ,  $m_v$  and  $m_\rho$  are the baryon, neutral scalar, neutral and charged vector meson masses respectively. The following terms

$$\begin{aligned} V_{\mu\nu} &= \partial_\mu V_\nu - \partial_\nu V_\mu \\ \mathbf{b}_{\mu\nu} &= \partial_\mu \mathbf{b}_\nu - \partial_\nu \mathbf{b}_\mu \\ F_{\mu\nu} &= \partial_\mu A_\nu - \partial_\nu A_\mu. \end{aligned} \quad (3.5.3)$$

are neutral, charged vector meson and photon field tensors.  $A_\mu$  is the massless photon field.

We have to specify that neutrons and protons interact identically with isoscalar

mesons but differently with isovector mesons.

The effective interaction among particles is given by

$$\mathcal{L}_{int} = \bar{\Psi} \left[ g_s \phi - \left( g_v V^\mu + \frac{1}{2} g_\rho \boldsymbol{\mathcal{I}} \cdot \mathbf{b}^\mu + e \frac{1 + \mathcal{I}_3}{2} A^\mu \right) \right] \Psi - U_{eff}(\phi, V_\mu, \mathbf{b}_\mu). \quad (3.5.4)$$

$g_s$ ,  $g_v$ ,  $g_\rho$  and  $e^2/(4\pi)$  are scalar, vector, charged vector and photon coupling constants.

$U_{eff}(\phi, V_\mu, \mathbf{b}_\mu)$  defines the nonlinear  $\sigma$ -meson self-interaction,  $\sigma - \rho$  and  $\omega - \rho$  couplings,

$$\begin{aligned} U_{eff}(\phi, V_\mu, \mathbf{b}_\mu) = & \frac{\kappa}{3!} (g_s \phi)^3 + \frac{\lambda}{4!} (g_s \phi)^4 - \frac{\zeta}{4!} g_v^4 (V_\mu V^\mu)^2 - \frac{\xi}{4!} g_\rho^4 (\mathbf{b}_\mu \cdot \mathbf{b}^\mu)^2 \\ & - g_\rho^2 (\mathbf{b}_\mu \cdot \mathbf{b}^\mu)^2 \left[ \Lambda_4 g_s^2 \phi^2 + \Lambda_v g_v^2 V_\mu V^\mu \right]. \end{aligned} \quad (3.5.5)$$

For simplicity, we set  $\xi$  and  $\Lambda_4$  to 0 in all parameters in the Lagrangian density.

### 3.5.2 Dirac-Hartree Approximation

In principle, the full quantum field theory is highly complex, and practically a convenient approximate starting point is needed. This results in the mean-field theory that has to be solved consistently. In such an approach, all quantum fluctuations are neglected and the meson fields are replaced by constant classical fields while those for baryons are quantized. We restrict ourselves to static, spherically symmetric nuclei with total angular momentum zero where the meson fields are radial dependent. Only the  $V_0(r)$ ,  $b_0(r)$  and  $A_0(r)$  components of the vector, charged vector and photon fields contribute as a result of current conservation. Therefore, in the mean-field approximation,

$$\begin{aligned} \phi(\mathbf{x}) & \rightarrow \langle \phi(\mathbf{x}) \rangle = \phi_0(r) \\ V^\mu(\mathbf{x}) & \rightarrow \langle V^\mu(\mathbf{x}) \rangle = V_0(r) \\ b^\mu(\mathbf{x}) & \rightarrow \langle b^\mu(\mathbf{x}) \rangle = b_0(r) \\ A^\mu(\mathbf{x}) & \rightarrow \langle A^\mu(\mathbf{x}) \rangle = A_0(r). \end{aligned} \quad (3.5.6)$$

The mean-field equations are deduced from the Euler-Lagrange equation,

$$\partial_\mu \frac{\partial \mathcal{L}}{\partial (\partial_\mu q)} - \frac{\partial \mathcal{L}}{\partial q} = 0 \quad (3.5.7)$$

which yields the Dirac equation for the baryon field

$$\left\{ i\gamma_\mu \partial^\mu - V(r) - \left( M - g_s \phi(r) \right) \right\} \Psi(x) = 0. \quad (3.5.8)$$

With the vector potential,  $V(r)$  given by

$$V(r) = \gamma^0 \left( g_v V_0(r) + \frac{1}{2} \mathcal{I}_3 b_0(r) + e \frac{1}{2} (1 + \mathcal{I}_3) A_0(r) \right). \quad (3.5.9)$$

The inhomogeneous part of the Klein-Gordon equation for meson fields are

$$\left( \frac{d^2}{dr^2} + \frac{2}{r} \frac{d}{dr} - m_i^2 - \partial_i U_{eff}(\phi_0, V_0, b_0) \right) U(r) = -S(r). \quad (3.5.10)$$

where  $m_i = m_s, m_v, m_\rho$ ,  $U(r) = (\phi_0(r), V_0(r), b_0(r))$  and the source term is expressed as

$$S(r) = \begin{cases} g_s \rho_s(r) & \text{for the } \sigma\text{-field,} \\ g_v \rho_v(r) & \text{for the V-field,} \\ g_\rho \rho_3 & \text{for the } \rho\text{-field,} \\ e \rho_p(r) & \text{for the Coulomb-field.} \end{cases} \quad (3.5.11)$$

The baryon field is an operator (quantized field) though, nevertheless one may seek normal-mode solutions for the linear equation 3.5.8 of the form

$\Psi(x) = \Psi(\mathbf{x}) \exp(-iEt)$ . This leads to the eigenvalue problem

$$\hat{h}\Psi(\mathbf{x}) \equiv \left\{ -i\boldsymbol{\alpha} \cdot \boldsymbol{\nabla} + V(r) + \beta [M - g_s \phi(r)] \right\} \Psi(\mathbf{x}) = E\Psi(\mathbf{x}) \quad (3.5.12)$$

where  $\hat{h}$  is the single-particle Dirac Hamiltonian. The eigenvalue equation 3.5.12 above has both positive- and negative-energy solutions  $\psi_\alpha(\mathbf{x})^\pm$ . The eigenfunction  $\Psi(\mathbf{x})$  can be expanded as

$$\Psi(\mathbf{x}) = \sum_{\alpha} \left[ A_{\alpha} \psi_{\alpha}^{+}(\mathbf{x}) + B_{\alpha}^{\dagger} \psi_{\alpha}^{-}(\mathbf{x}) \right]. \quad (3.5.13)$$

Here  $A_{\alpha}$  and  $B_{\alpha}^{\dagger}$  are baryon and antibaryon annihilation and creation operators obeying the standard anticommutation relations. So the positive-energy spinors take the form given in 3.4.56

$$\psi_{\alpha}(\mathbf{r}) = i \begin{pmatrix} G_{nljm_{\mathcal{I}}}(r) \\ -i\boldsymbol{\sigma} \cdot \hat{\mathbf{r}} F_{nljm_{\mathcal{I}}}(r) \end{pmatrix} \mathcal{Y}_{lj}^{m_j}(\hat{\mathbf{r}}) \quad (3.5.14)$$

where the angular eigenfunctions of good quantum number related to the quantum number  $k$  is given by

$$j = |k| - \frac{1}{2}, \quad l = \begin{cases} k & \text{if } k > 0 \\ -(k+1) & \text{if } k < 0 \end{cases} \quad (3.5.15)$$

are built up of the spherical harmonics,  $\mathcal{Y}_{lj}^{m_j}(\hat{\mathbf{r}})$ , Pauli spinors,  $\chi_{m_s}$ , and Clebsch-Gordon coefficients [117]

$$\mathcal{Y}_{lj}^{m_j}(\hat{\mathbf{r}}) = \sum_{m_l, m_s} \langle lm_l \frac{1}{2} m_s | j m_j \rangle Y_{lm_l}(\hat{\mathbf{r}}) \chi_{m_s}. \quad (3.5.16)$$

The sums over  $m_s$  range from  $-\frac{1}{2}$  to  $+\frac{1}{2}$  and the sums over  $m_l$  range from  $-l$  to  $+l$ . We take  $m_{\mathcal{I}} = \frac{1}{2}$  for the protons and  $m_{\mathcal{I}} = -\frac{1}{2}$  for the neutrons.

The normalization which defines the probability of finding each single particle (matter) somewhere in space is given by

$$\int_0^\infty r^2 dr \left( |G_{nljm_{\mathcal{I}}}(r)|^2 + |F_{nljm_{\mathcal{I}}}(r)|^2 \right) = 1. \quad (3.5.17)$$

It follows the normalization of spin spherical harmonics,

$$\sum_{m_j=-j}^j \mathcal{Y}_{lj}^{m_j}(\hat{\mathbf{r}}) \mathcal{Y}_{lj}^{m_j}(\hat{\mathbf{r}})^\dagger = \frac{j + \frac{1}{2}}{4\pi} \mathbf{1}_2. \quad (3.5.18)$$

For a closed-shell nucleus with each of  $2j + 1$  occupied magnetic substates, three non-vanishing ground state densities are found out of five which are scalar, vector (matter), tensor, axial-vector and pseudoscalar. We have the vector (baryon) and scalar densities given by

$$\begin{pmatrix} \rho_v(\mathbf{r}) \\ \rho_s(\mathbf{r}) \end{pmatrix} = \sum_{njl m_{\mathcal{I}}} \sum_{m_j=-j}^j \bar{\psi}_{njl m_j m_{\mathcal{I}}}(\mathbf{r}) \begin{pmatrix} \gamma^0 \\ \mathbf{1}_4 \end{pmatrix} \psi_{njl m_j m_{\mathcal{I}}}(\mathbf{r}) \quad (3.5.19)$$

and the tensor density

$$\rho_T^{0i}(\mathbf{r}) = \sum_{njl m_{\mathcal{I}}} \sum_{m_j=-j}^j \bar{\psi}_{njl m_j m_{\mathcal{I}}}(\mathbf{r}) \sigma^{0i} \psi_{njl m_j m_{\mathcal{I}}}(\mathbf{r}). \quad (3.5.20)$$

Finally we obtain the radial dependent scalar, vector and tensor densities for each isospin state  $m_{\mathcal{I}} = \pm \frac{1}{2}$

$$\rho_s(r) = \sum_{njl} \frac{2j+1}{4\pi} \left[ G_{njl m_{\mathcal{I}}}^2(r) - F_{njl m_{\mathcal{I}}}^2(r) \right], \quad (3.5.21)$$

$$\rho_v(r) = \sum_{njl} \frac{2j+1}{4\pi} \left[ G_{njl m_{\mathcal{I}}}^2(r) + F_{njl m_{\mathcal{I}}}^2(r) \right], \quad (3.5.22)$$

$$\rho_T(r) = 2 \sum_{njl} \frac{2j+1}{4\pi} \left[ G_{njl m_{\mathcal{I}}}(r) F_{njl m_{\mathcal{I}}}(r) \right] \quad (3.5.23)$$



where we have used the relation 3.5.18. The radial functions  $G_{njl m_{\mathcal{I}}}(r)$  and  $F_{njl m_{\mathcal{I}}}(r)$  are bound state solutions of the Dirac equation. It follows after substitution of 3.5.14 into equation 3.5.12, that

$$\frac{d}{dr}G_a(r) + \frac{k}{r}G_a(r) - \left[ E_a - V(r) + M - g_s\phi(r) \right] F_a(r) = 0 \quad (3.5.24)$$

$$\frac{d}{dr}F_a(r) - \frac{k}{r}F_a(r) + \left[ E_a - V(r) - M + g_s\phi(r) \right] G_a(r) = 0. \quad (3.5.25)$$

$a$  denotes a set of quantum numbers,  $\{a\} = \{n, j, l, m_{\mathcal{I}}\}$ .

The time-independent spherically-symmetric fields  $\phi_0(r)$ ,  $V_0(r)$ ,  $b_0(r)$  and  $A_0(r)$  obey the Klein-Gordon nonlinear equations

$$\frac{d^2}{dr^2}\phi_0(r) + \frac{2}{r}\frac{d}{dr}\phi_0(r) - m_s^2\phi_0(r) - \partial_{\phi_0}U_{eff}(\phi_0, V_0, b_0) = -g_s\rho_s(r) \quad (3.5.26)$$

$$\frac{d^2}{dr^2}V_0(r) + \frac{2}{r}\frac{d}{dr}V_0(r) - m_v^2V_0(r) + \partial_{V_0}U_{eff}(\phi_0, V_0, b_0) = -g_v\rho_v(r) \quad (3.5.27)$$

$$\frac{d^2}{dr^2}b_0(r) + \frac{2}{r}\frac{d}{dr}b_0(r) - m_p^2b_0(r) + \partial_{b_0}U_{eff}(\phi_0, V_0, b_0) = -\frac{1}{2}g_\rho\rho_3(r) \quad (3.5.28)$$

$$\frac{d^2}{dr^2}A_0(r) + \frac{2}{r}\frac{d}{dr}A_0(r) = -e\rho_p(r). \quad (3.5.29)$$

The spherical isovector  $\rho_3$  and charged  $\rho_p$  densities for each isospin are expressed as

$$\rho_3(r) = \sum_{njl} \mathcal{I}_3 \frac{2j+1}{4\pi} \left[ G_{njl m_{\mathcal{I}}}^2(r) + F_{njl m_{\mathcal{I}}}^2(r) \right], \quad (3.5.30)$$

$$\rho_p(r) = \sum_{njl} \frac{1 + \mathcal{I}_3}{2} \frac{2j+1}{4\pi} \left[ G_{njl m_{\mathcal{I}}}^2(r) + F_{njl m_{\mathcal{I}}}^2(r) \right]. \quad (3.5.31)$$

This set of coupled differential equations are solved iteratively and the procedure is described in the code provided by Professor Van der Ventel [118]. Once the solutions are found; the scalar, vector and tensor densities are computed from equations 3.5.19 and 3.5.20. The resulting densities are then inserted into the computation of the cluster-core potential 3.4.71. Two Lagrangian parametrizations are used in this thesis which values are given in table 3.2 taken from ref. [116] where the nucleon's mass has been fixed to 930 MeV.

**Table 3.2:** Parameters used for different QHD models given in MeV

QHD Models	NL3	FSU
$g_s^2$	104.3871	112.1996
$g_v^2$	165.5854	204.5469
$g_\rho^2$	79.6000	138.4701
$\kappa$	3.8599	1.4203
$\lambda$	-0.0159	0.0238
$\zeta$	0.0000	0.0600
$\Lambda_v$	0.0000	0.0300
$m_s$	508.1940	491.5000
$m_v$	782.5010	782.5010
$m_\rho$	763.0000	763.0000

# Chapter 4

## Numerical Analysis and Observables

### 4.1 Introduction

After describing the necessary tools that indicate clear evidence of cluster states and discuss cluster-core different potential models, we next test our predictions against measurements in binary model configurations given in table 2.1. Note that at first the phenomenological (SW + SW<sup>3</sup>) is used as a benchmark to other microscopic potentials. The double folding potential are calculated with the M3Y, the CEG83 inter-nucleon interactions and the relativistic Love Franey model. Observables of interest will be calculated with different potential models.

### 4.2 Double Folding Potential Calculation

The double folding potentials are calculated using the modified computer code DFM obtained from [119].

#### 4.2.1 Michigan Three-range Yukawa Interaction (M3Y)

The direct part of cluster-core nuclear potential, equation 3.3.51 is calculated with the direct part of M3Y, equation 3.3.44 whose parameters are given in table 4.1. For the exchange part, we use instead the zero-range interaction defined in equation 3.3.45. Hence, performing the momentum analysis [92], the zero order multiple component of the nuclear potential reads

$$U(r) = \frac{\lambda}{2\pi^2} \int_0^\infty \rho_1(q)\rho_2(q)V_{eff}(q)J_0(qr)q^2dq \quad (4.2.1)$$

where  $\lambda$  is the normalization factor which accounts for medium effects. Here the Fourier transform of the densities and the effective interaction  $V_{eff}(s, E)$

**Table 4.1:** The parameters of the Reid M3Y interactions

Coefficients	Reid
$v_D^1$	7999.0000
$v_D^2$	-2134.0000
$v_D^3$	0.0000
$G_0$	-276.0000
$R_1$	4.0000
$R_2$	2.5000
$R_3$	0.7072

are expressed as

$$\rho_i(q) = 4\pi \int_0^\infty \rho_i(r) J_0(qr) r^2 dr \quad (4.2.2)$$

and

$$V_{eff}(q) = 4\pi \int_0^\infty V_{eff}(r) J_0(qr) r^2 dr \quad (4.2.3)$$

with

$$V_{eff}(r) = 7999 \frac{\exp(-4r)}{4r} - 2134 \frac{\exp(-2.5r)}{2.5r} - 276 \left( 1 - 0.005 \frac{E}{A_2} \right) \quad (4.2.4)$$

The nuclear matter densities appearing in equation 4.2.1, as stated in Section 3.3, have a Gaussian form, 3.3.57 for the alpha cluster. And two-Fermi parameters, 3.3.58, with diffuseness  $a = 0.52$  fm for  $^{10}\text{Be}$  cluster or  $a = 0.54$  fm for more massive clusters and  $^{208}\text{Pb}$  core.

## 4.2.2 Complex Effective Gaussian interaction: CEG83

We have to emphasize that the CEG whose parameters are given in table 4.2 was designed for nucleon-nucleus scattering in its origin, here one would like to taste the influence of many-body effects by setting the value of Fermi momentum to its maximum,  $k_f = 1.4 \text{ fm}^{-1}$ . In principle, this value depends on the nuclear density calculated in the centre of mass for the nuclear matter.

Unlike in the case of M3Y, here we step through two doors when dealing with the single nucleon knock-on exchange. Firstly, the zero-range exchange given in equation 3.3.45 is used for the exchange potential (CEG83a). This typical situation is analogue to the double folding potential obtained with M3Y interaction in equation 4.2.1. And secondly a consistent treatment of finite range exchange (CEG83b) is handled in Thomas-Fermi approximation explained early in 3.3.52.

**Table 4.2:** Parameters of the central part for the CEG83 in the range (fm);  $\lambda_1 = 2.500$ ,  $\lambda_2 = 0.8900$ ,  $\lambda_3 = 0.5000$ .

State	i	$v_0(MeV)$	$\alpha(fm)$	$\beta(fm^2)$
SO	1	7.5400	0.0000	0.0000
	2	120.4000	-0.5583	0.5062
	3	49.4800	-0.8833	1.6140
TE	1	-5.0340	-0.3716	0.1840
	2	-829.4000	-0.6721	0.2233
	3	1359.0000	-0.2171	0.1349
SE	1	-3.9280	0.1839	-0.1414
	2	-490.9000	-0.3386	0.1079
	3	1293.0000	-0.0362	0.0179
T0	1	0.6390	0.0000	0.0000
	2	-109.7000	0.1447	-0.2068
	3	349.1000	1.1440	-0.3268

Consequently, the direct part is expressed as in equation 4.2.1.

However the exchange part defined in equation 3.3.52 involving non diagonal elements of the density matrix are treated consistently. Because it contains the finite-range exchange effects arising from Pauli principal in the local density approximation. An iterative procedure is handled when evaluating this potential. Hence in momentum space [92], this exchange potential is written as [120],

$$U_{EX}(r) = \lambda 4\pi \int_0^\infty G(r, s) J_0\left(\frac{K(r)s}{\mu}\right) V_{EX}(s) s^2 ds \quad (4.2.5)$$

where

$$G(r, s) = \frac{1}{2\pi^2} \int_0^\infty f_1(q, s) f_2(q, s) J_0(qr) q^2 dq \quad (4.2.6)$$

and

$$f_i(q, s) = 4\pi \int_0^\infty f_1(r, s) f_2(r, s) J_0(qr) r^2 dr \quad (4.2.7)$$

with

$$f_i(r, s) = \rho_i(r) \hat{j}_1(K_{F_i}(r)s). \quad (4.2.8)$$

The plots in figures 4.1, 4.2, 4.3 and 4.4 represent different potential models including the Saxon-Woods potential whose parameters are taken from [27]. The curves of potentials for  ${}^4\text{He}+{}^{208}\text{Pb}$  configuration calculated with the zero-range exchange term are indeed much deeper in the interior region and diffused

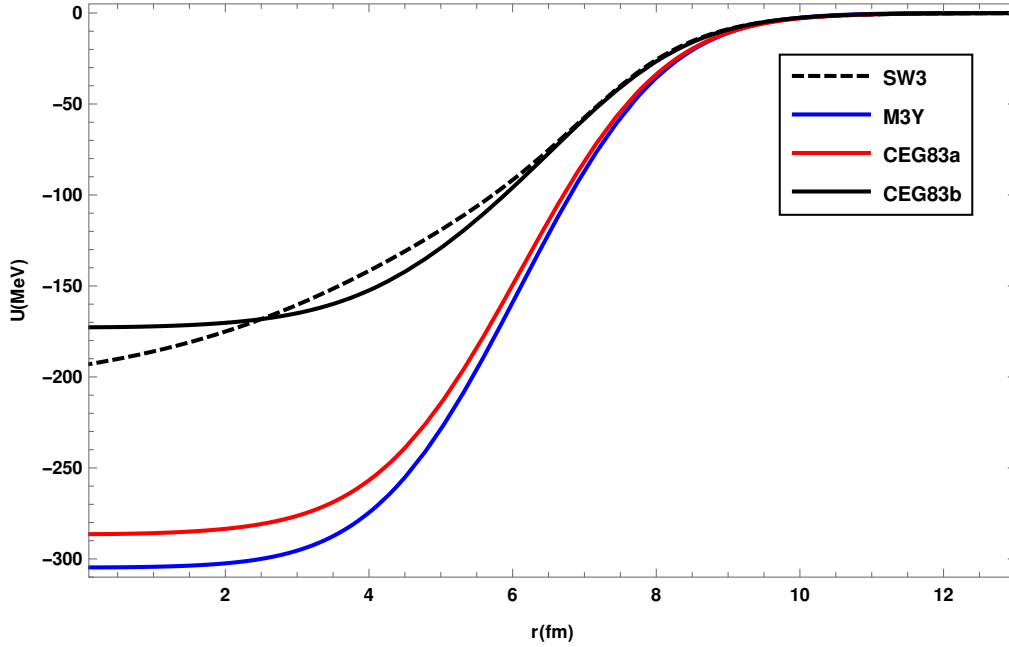


**Figure 4.1:** Plots of cluster-core local potential for  ${}^4\text{He} + {}^{208}\text{Pb}$ . *CEG83a* (zero-range exchange interaction) and *CEG83b* (finite-range exchange interaction) along with the phenomenological Saxon-Woods potential, *SW3* (black dashed line)

at the surface compared with modified Woods-Saxon potential for both effective interactions, M3Y and CEG83. However there is a shift in CEG83 with regard to M3Y and both are flattened in the interior region. However, the CEG83 finite-range exchange which takes into account the medium effects looks much shallower and flattened as well in the interior region compared to the SW3. Eventually, for the heavier cluster although deep in the interior region but are slightly rounded compared to  ${}^4\text{He} + {}^{208}\text{Pb}$  curve. The finite-range exchange mimics the shape of SW3 but more shallow in the interior and little bit diffused at the surface. Ultimately, we notice that the more is larger the cluster, more is deeper the potential and diffused near the surface region. The consequences of such remarks are traced from the observables that will be calculated.

### 4.2.3 Relativistic-Mean-Field Results and Potential

The relativistic cluster-core potential defined in equation 3.4.71, is calculated for each cluster configuration. Here we add the real part of the nucleon-nucleon amplitudes, since we are describing the ground state properties only.

The results obtained from the RMF will allow us to extract proton and neutron vector, and scalar densities to be folded with the RLF scattering amplitudes expressed in equation 3.4.72. We employ the two Lagrangian densities parametrizations, FSU and NL3 since it was realised that they are efficient for

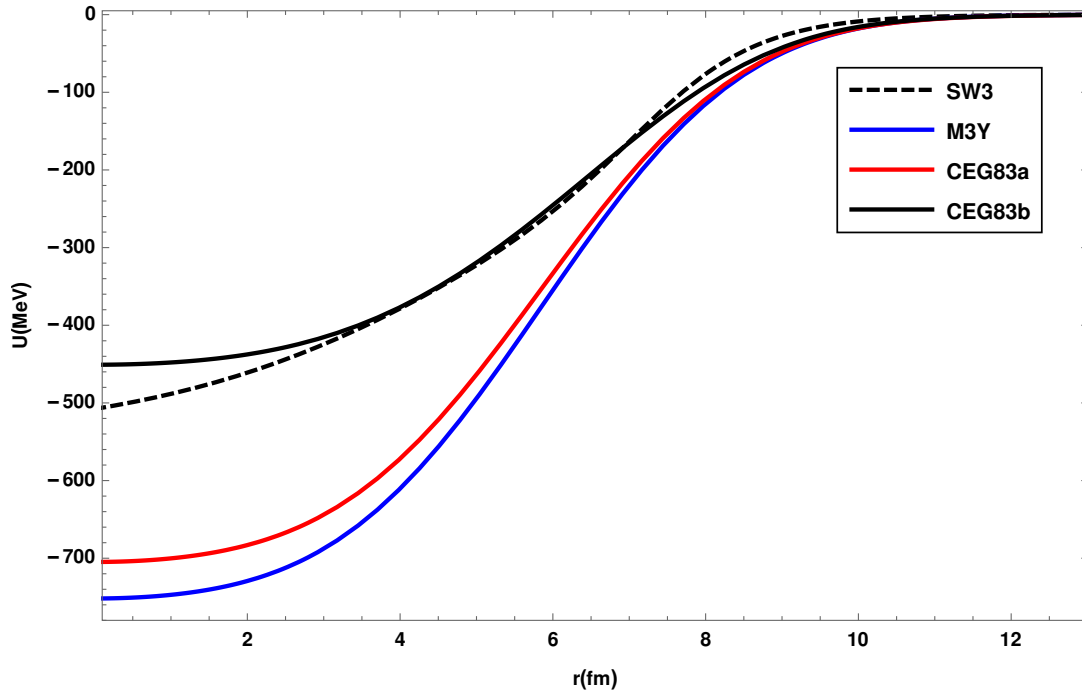


**Figure 4.2:** Plots of cluster-core local potential for  $^{10}\text{Be} + ^{208}\text{Pb}$ . *CEG83a* (zero-range exchange interaction) and *CEG83b* (finite-range exchange interaction) along with the phenomenological Saxon-Woods potential, *SW3* (black dashed line)

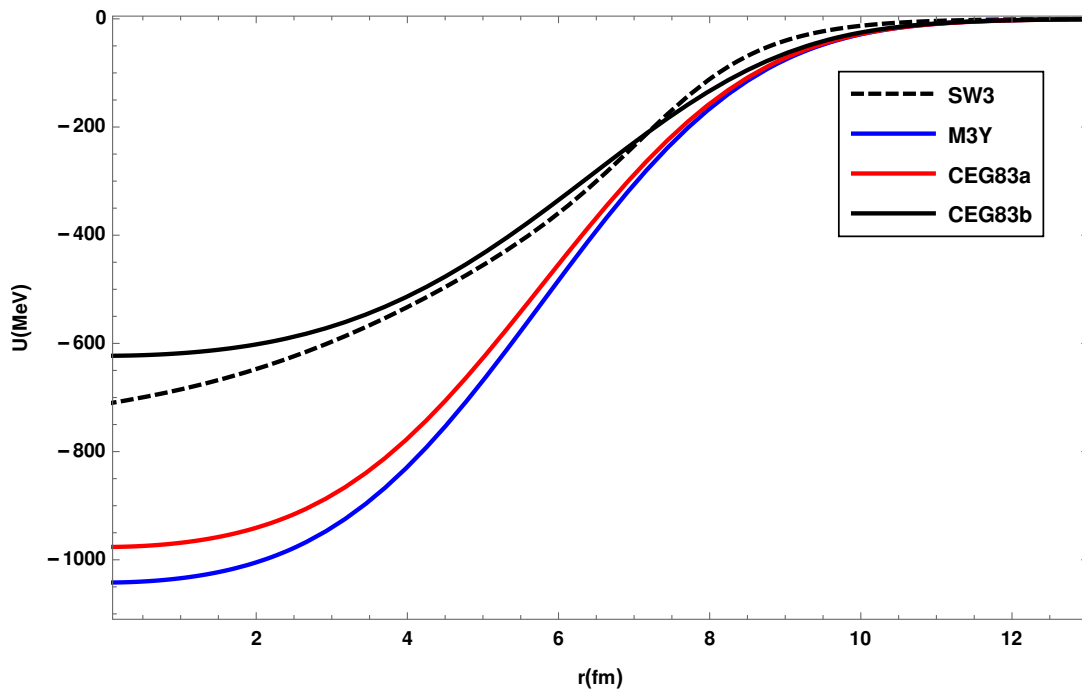


**Figure 4.3:** Plots of cluster-core local potential for  $^{14}\text{C} + ^{208}\text{Pb}$ . *CEG83a* (zero-range exchange interaction) and *CEG83b* (finite-range exchange interaction) along with the phenomenological Saxon-Woods potential, *SW3* (black dashed line)

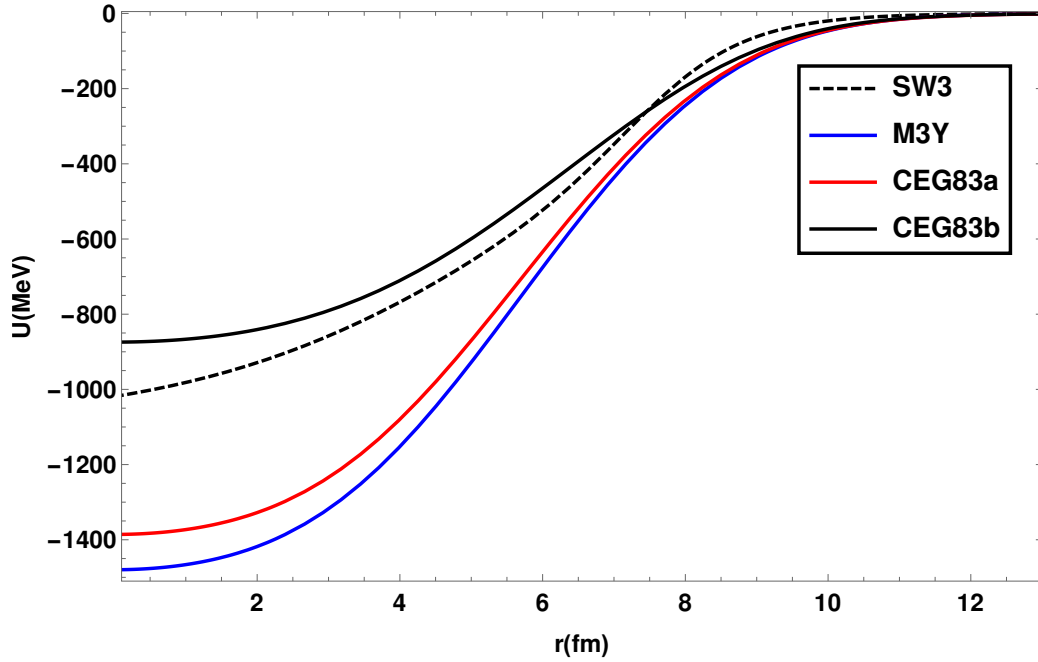


**Figure 4.4:** Plots of cluster-core local potential for  $^{20}\text{O} + ^{208}\text{Pb}$ . *CEG83a* (zero-range exchange interaction) and *CEG83b* (finite-range exchange interaction) along with the phenomenological Saxon-Woods potential, *SW3* (black dashed line)

describing the properties of stable nuclei as well for those far from the valley of beta stability including features of neutron stars. They include three mesons, and the photon with different coupling compared to the QHDI and QHDII models.

In figures 4.5, 4.6, 4.7, 4.8 and 4.9, the scalar and vector(baryon) densities obtained from the RMF calculations are plotted against the radial distance for both models NL3 and FSU. The first two classes of cluster exhibit central peaks that are more pronounced for NL3 compared to the FSU effective interactions. The scalar and vector densities for neutrons and protons are identical in NL3 and FSU for doubly magic nucleus,  $^4\text{He}$ . Nevertheless, the scalar and vector densities for neutrons are shifted in  $^{10}\text{Be}$  compared to protons densities. For  $^{14}\text{C}$  and  $^{20}\text{O}$ , the peak is now de-localised with densities more pronounced for NL3 than FSU.

The doubly closed shell  $^{208}\text{Pb}$ , there are moderate shell oscillations in the interior region for both scalar and vector densities. The tensor density is nearly zero inside the nuclear matter. Consequently, the tensor contribution of the interaction will be irrelevant in our description. Therefore the potential has only scalar and vector parts.

The Relativistic Love-Franey (RLF) form factors for meson-exchange vertex in equation 3.4.37 are used as an input for deriving the relativistic nucleon-



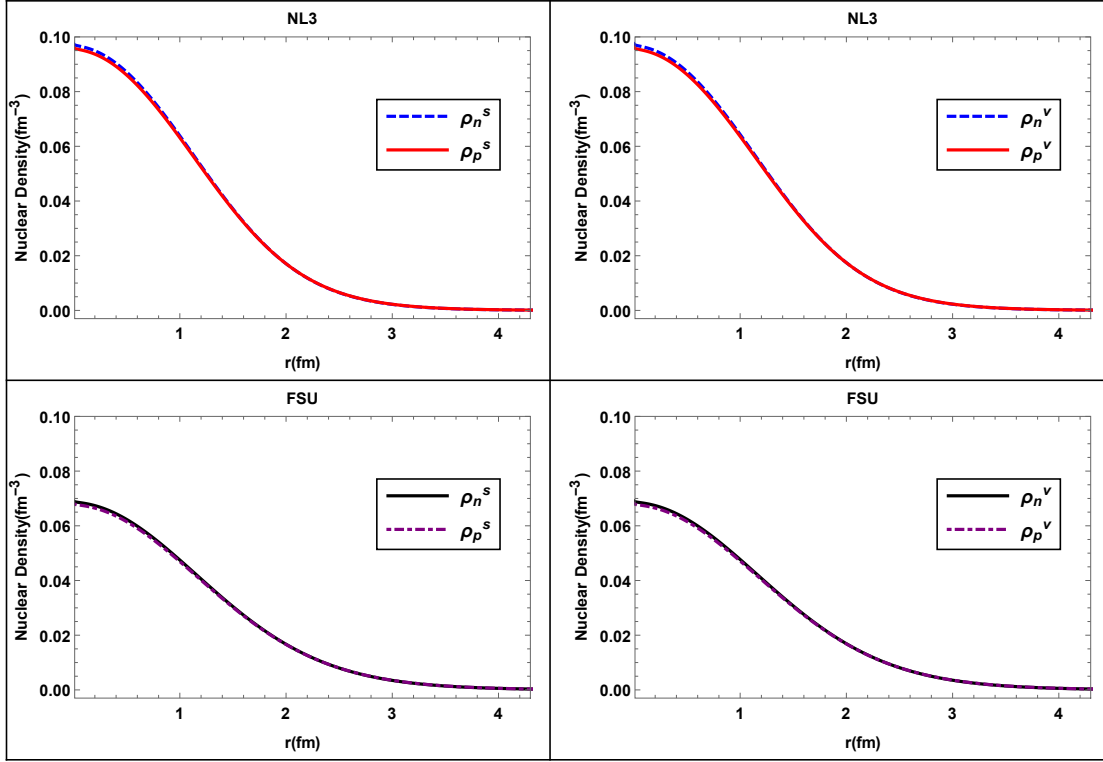


**Figure 4.5:** Scalar and vector  ${}^4\text{He}$  nucleons densities distribution. Top and bottom panels are results calculated with NL3 and FSU Lagrangian densities

nucleon interaction which are Yukawa functions. However this Lorentz covariant on-shell nucleon-nucleon scattering amplitude is energy-dependent. And for lack of parameters at lower energies, we are going to make use of real parameters generated in the range of 50 to 200 MeV and that can be extrapolated to energies between 40 and 300 MeV [103]. Table 4.3 lists values of RLF parameters to be tested in our model in which the coupling constant follows the exponential energy-dependence such as

$$g^2(E) = g_0^2 \left[ 1 + a_g \left( e^{a_T T_{rel}} - 1 \right) \right], \quad (4.2.9)$$

where

$$T_{rel} \equiv \frac{T_0 - T_{lab}}{T_0}. \quad (4.2.10)$$

$g_0^2$ ,  $a_g$  and  $a_T$  are dimensionless constants which values are given in table 4.3 with  $T_0$  fixed to 200 MeV and  $T_{rel}$  in the range of 50 to 200 MeV.

The cluster-core relativistic potential is now calculated by folding the RLF  $\mathcal{T}_{D(EX)}^L$ , amplitude with the relevant neutron and proton densities generated

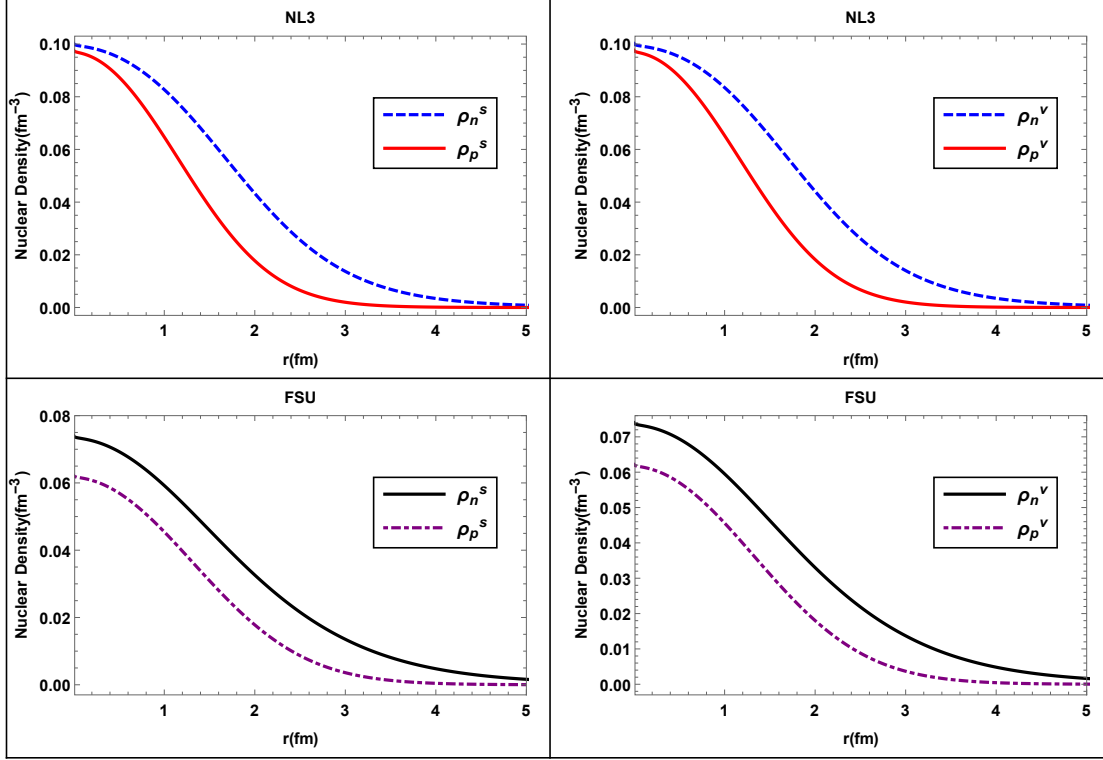


**Figure 4.6:** Scalar and vector  $^{10}\text{Be}$  nucleons densities distribution. Top and bottom panels are results calculated with NL3 and FSU Lagrangian densities

from RMF, scalar and vector. Hence performing the momentum analysis, the zero order multipole component of the relativistic potential is given by

$$U(r) = \lambda \left( U^S(r) + U^V(r) \right) \quad (4.2.11)$$

where the direct potential reads

$$U^S(r) = U_D^S(r) + U_{EX}^S(r) \quad (4.2.12)$$

and

$$U^V(r) = U_D^V(r) + U_{EX}^V(r) \quad (4.2.13)$$

$$U_D^{(S,V)}(r) = \sum_{i=n_1,p_1} \sum_{j=n_2,p_2} \frac{1}{2\pi^2} \int_0^\infty \tau_{D,ij}^{(S,V)}(q) \rho_i^{(S,V)}(q) \rho_j^{(S,V)}(q) J_0(qr) q^2 dq. \quad (4.2.14)$$

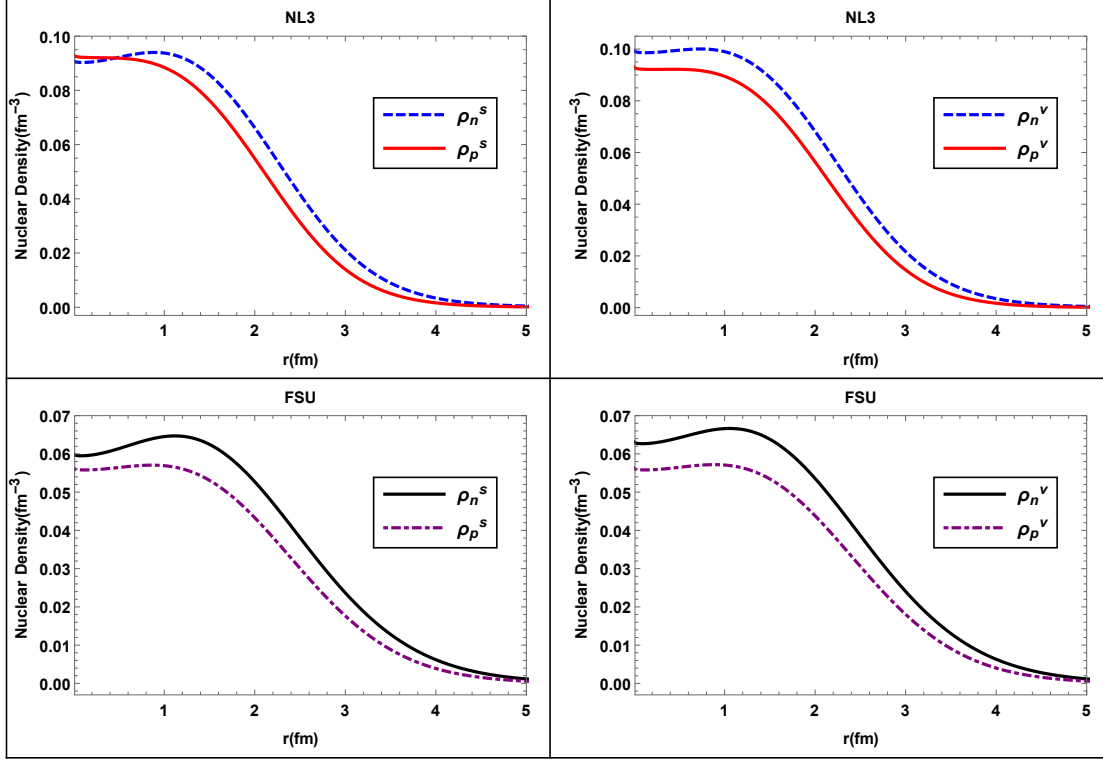


**Figure 4.7:** Scalar and vector  $^{14}\text{C}$  nucleons densities distribution. Top and bottom panels are results calculated with NL3 and FSU Lagrangian densities

Notice that the normalization constant,  $\lambda$  is added for medium effects as we have mentioned early. The exchange potential is written as

$$U_{EX}^S(r) = 4\pi \sum_{i=n_1,p_1} \sum_{j=n_2,p_2} \sum_L \int_0^\infty \tau_{EX,ij}^L(s) C_{L,S} H_{ij}^S(r,s) J_0\left(\frac{Ps}{\mu}\right) s^2 ds \quad (4.2.15)$$

$$U_{EX}^V(r) = 4\pi \sum_{i=n_1,p_1} \sum_{j=n_2,p_2} \sum_L \int_0^\infty \tau_{EX,ij}^L(s) C_{L,V} H_{ij}^V(r,s) J_0\left(\frac{Ps}{\mu}\right) s^2 ds \quad (4.2.16)$$

where

$$H_{i,j}^{S,V}(r) = \frac{1}{2\pi^2} \int_0^\infty h_i^{S,V}(q,s) h_j^{S,V}(q,s) J_0(qr) q^2 dq \quad (4.2.17)$$

with

$$h_i^{S,V}(q,s) = 4\pi \int_0^\infty h_i(r,s) h_j(r,s) J_0(qr) r^2 dr. \quad (4.2.18)$$

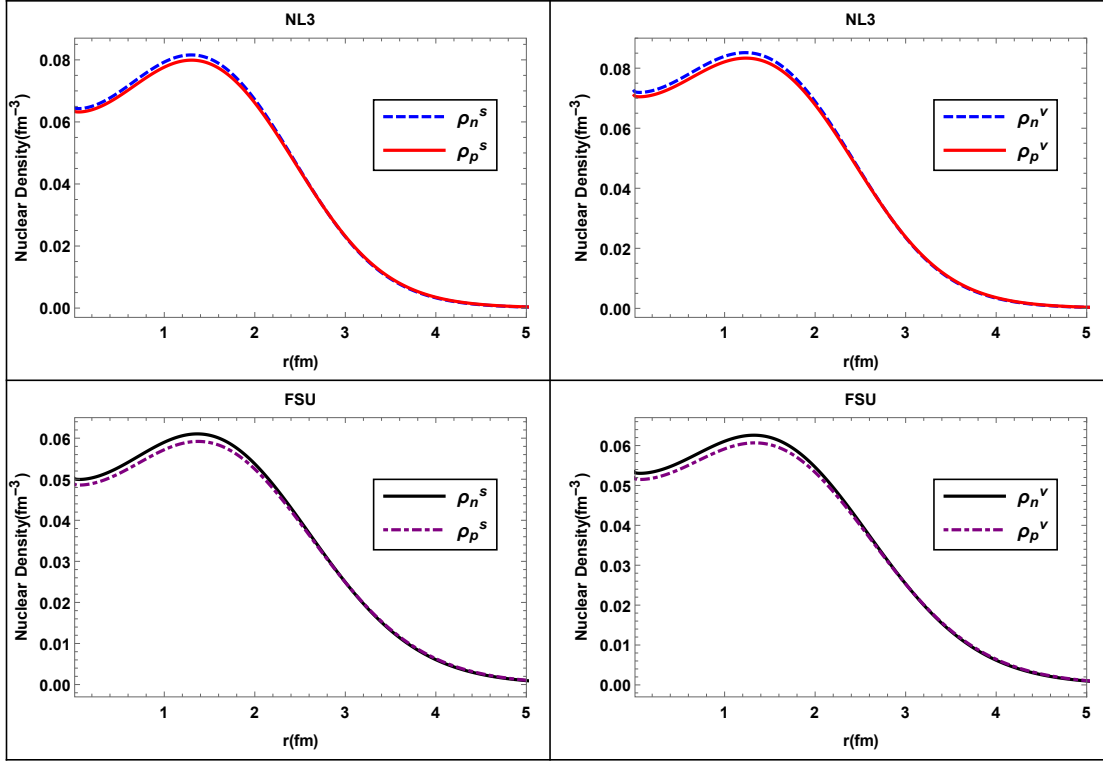


**Figure 4.8:** Scalar and vector  $^{20}\text{O}$  nucleons densities distribution. Top and bottom panels are results calculated with NL3 and FSU Lagrangian densities

Note that the Fourier transform of the functions defined on 3.4.45 and 3.4.46 are given by

$$\begin{aligned}
 f(r) &= \int_0^\infty \frac{d^3\mathbf{q}}{(2\pi)^3} e^{i\mathbf{q}\cdot\mathbf{r}} f(\mathbf{q}) \\
 &= \frac{g^2}{4\pi} \frac{\Lambda^2}{\Lambda^2 - m^2} \left( \frac{\Lambda^2}{\Lambda^2 - m^2} \left( \frac{e^{-mr}}{r} - \frac{e^{-\Lambda r}}{r} \right) - \frac{\Lambda}{2} e^{-\Lambda r} \right).
 \end{aligned} \tag{4.2.19}$$

In figure 4.10, 4.11, 4.12 and 4.13 we show in left panel the plots for individual potentials scalar and vector for NL3 and FSU Lagrangian densities. On the right panel are plotted the global potential with Saxon-Woods modified as guidance toward our realistic cluster-core potential. We notice a flat shape in the interior region and more diffused surface as a consequence of the densities distributions yielded by the relativistic-mean-field approach.

Our calculations indicate clearly that the exchange energies for both scalar

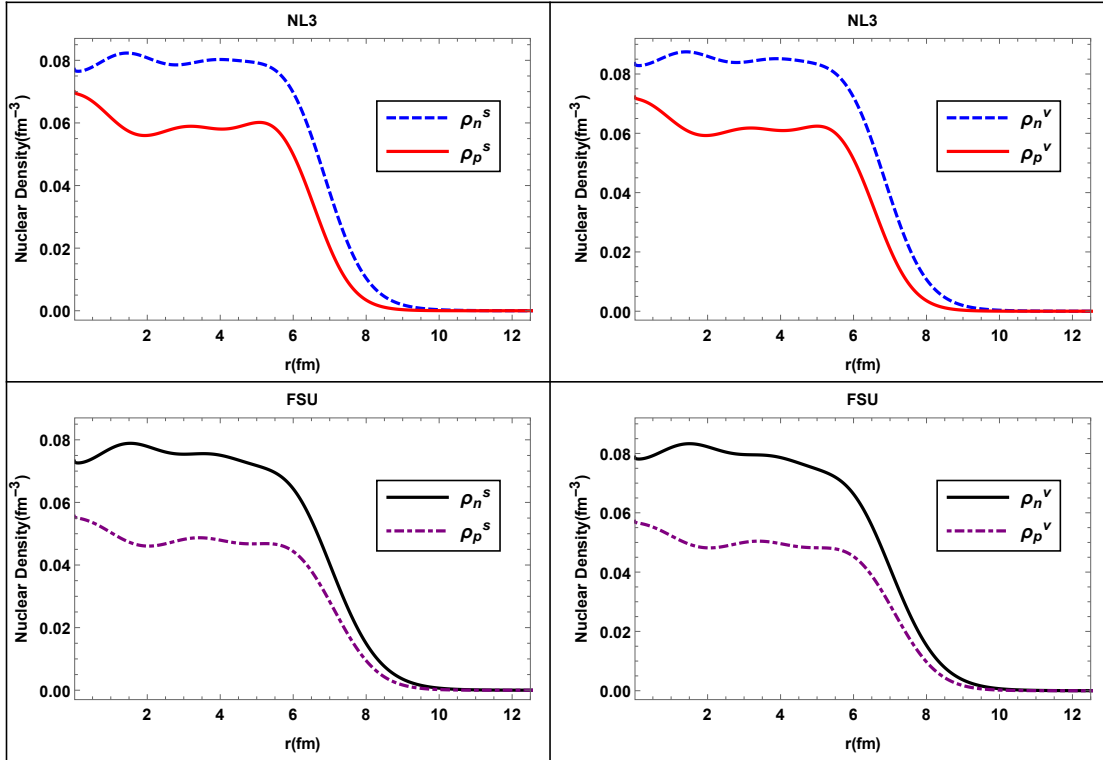


**Figure 4.9:** Scalar and vector  $^{208}\text{Pb}$  nucleons densities distribution. Top and bottom panels are results calculated with NL3 and FSU Lagrangian densities

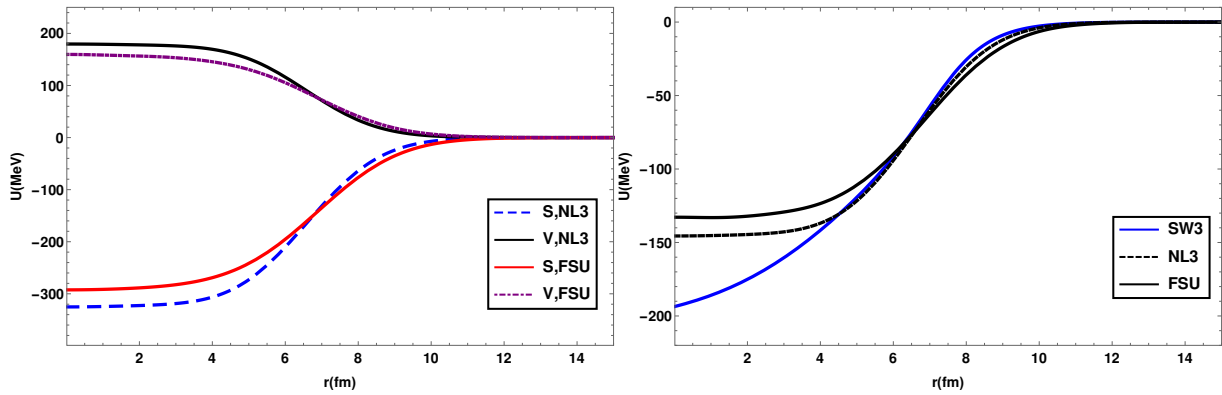


**Figure 4.10:** Plot of the individual scalar and vector potentials (left panel) for a typical parameter set, NL3 and FSU Lagrangian densities. The right panel is the total potential resulting from the near-cancellation of scalar and vector terms for  $^4\text{He} + ^{208}\text{Pb}$ , and the phenomenological Saxon-Woods potential, SW3 (blue line)

**Table 4.3:** Real RLF parameters. The last parameters are dimensionless except the masses and cutoff parameters which are in MeV

Meson	Isospin	$m$	$\Lambda$	$g_0^2$	$a_g$	$a_T$
$\sigma$ , Scalar(S)	0	600	965.23	-8.379	$-5.581 \times 10^{-1}$	$2.364 \times 10^{-1}$
$\delta$ , Scalar(S)	1	500	3000.00	$6.233 \times 10^{-3}$	5.675	3.521
$\omega$ , Vector(V)	0	782	1158.74	10.14	$-2.219 \times 10^{-2}$	3.793
$\rho$ , Vector(V)	1	770	3000.00	$-1.535 \times 10^{-1}$	3.429	$1.825 \times 10^{-1}$
$t_0$ , Tensor(T)	0	550	1955.59	$2.783 \times 10^{-1}$	1.331	$3.074 \times 10^{-1}$
$t_1$ , Tensor(T)	1	600	1290.72	$-2.497 \times 10^{-1}$	$5.508 \times 10^{-1}$	3.959
$\eta$ , Pseudoscalar(P)	0	950	980.99	10.89	1.553	1.956
$\pi$ , Pseudoscalar(P)	1	138	678.44	11.95	$-1.671 \times 10^{-1}$	$3.216 \times 10^{-1}$
$a_0$ , Axial vector(A)	0	500	1577.53	$4.842 \times 10^{-1}$	1.440	2.847
$a_1$ , Axial vector(A)	1	650	745.19	-1.355	$2.480 \times 10^{-1}$	3.623

and vector are relatively small. This is in accordance with the relativistic Hartree-Fock calculations in spherical nuclei as stated in [96] which reduced the potential to Hartree type.

#### 4.2.4 Decay half-lives

To account for the many-body effects, we normalize the potential to its ground state using the quantization rule defined in equation 2.4.31 in order also to adjust the depth of each potential. A convenient way is also applied by tuning the values of the different parameters contained in the nucleon-nucleon interaction of the RLF model expressed in equation 3.4.45 until the normalization constant is close unity. This means by rescaling the couplings strength, the masses of the nucleons and the mesons such that

$$g^* = a g, m^* = b m, M^* = c M ; a = 0.18, b = 0.6, c = 0.6 \quad (4.2.20)$$

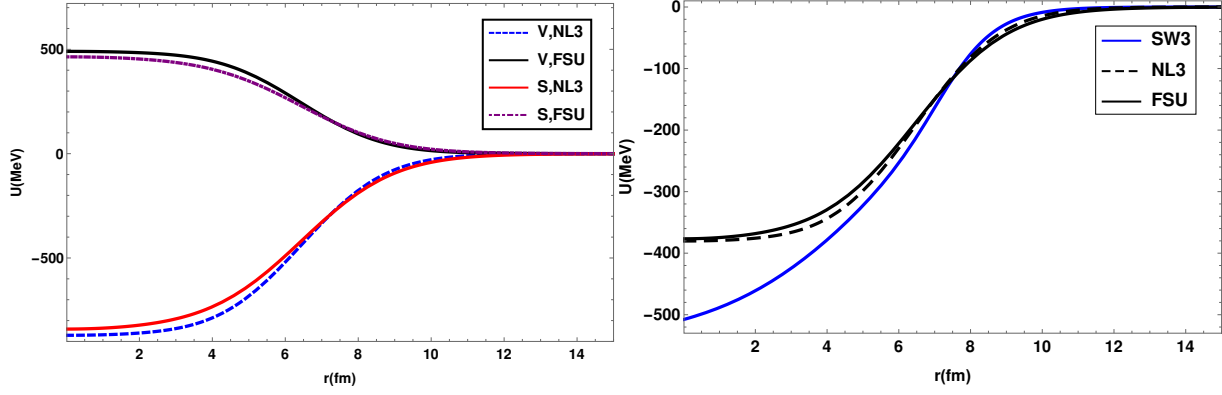


**Figure 4.11:** Plot of the individual scalar and vector potentials (left panel) for a typical parameter set, NL3 and FSU Lagrangian densities. The right panel is the total potential resulting from the near-cancellation of scalar and vector terms for  $^{10}\text{Be} + ^{208}\text{Pb}$ , and the phenomenological Saxon-Woods potential, SW3 (blue line)

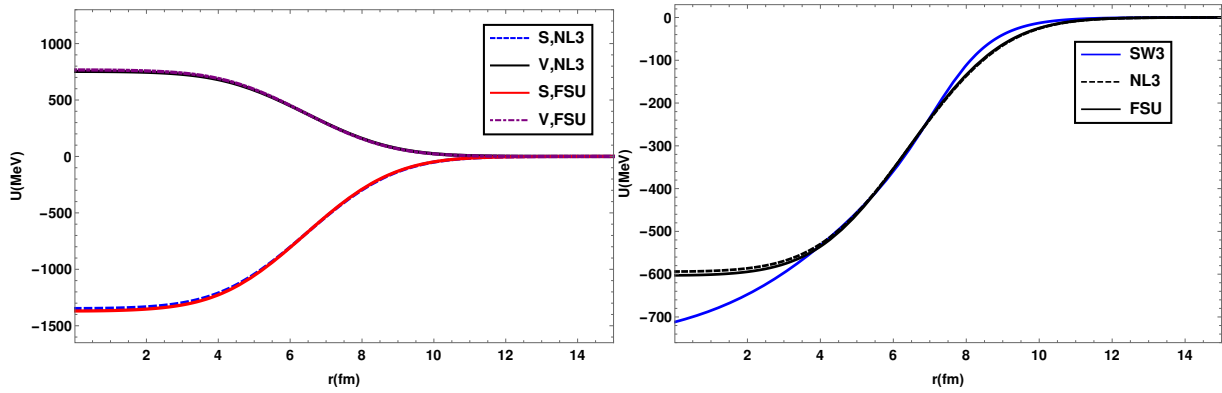


**Figure 4.12:** Plot of the individual scalar and vector potentials (left panel) for a typical parameter set, NL3 and FSU Lagrangian densities. The right panel is the total potential resulting from the near-cancellation of scalar and vector terms for  $^{14}\text{C} + ^{208}\text{Pb}$ , and the phenomenological Saxon-Woods potential, SW3 (blue line)

This allowed to overcome the diffuseness on the nuclear surface as seen from curves in figure 4.10, 4.11, 4.12 and 4.13 . The different values of normalization constants are given in table 4.4.

Table 4.6 gives the calculated decay half-lives using equation 2.3.13; and their experimental values for selected cluster configurations [121–123] except for  $^{218}\text{Rn}$  that has never been measured. The calculated ground state decay half-life of  $^{212}\text{Po}$  is half of the measured value for the two potentials, M3Y and CEG83 plus zero-range while the finite-range underestimated the experimental value. For heavy cluster emissions, such as  $^{222}\text{Ra}$  to  $^{14}\text{C}$ , the estimated half-lives are 100 times smaller for M3Y and CEG83 plus zero-range. 2000 times less than the experimental value for the finite-range. Whereas in the case of

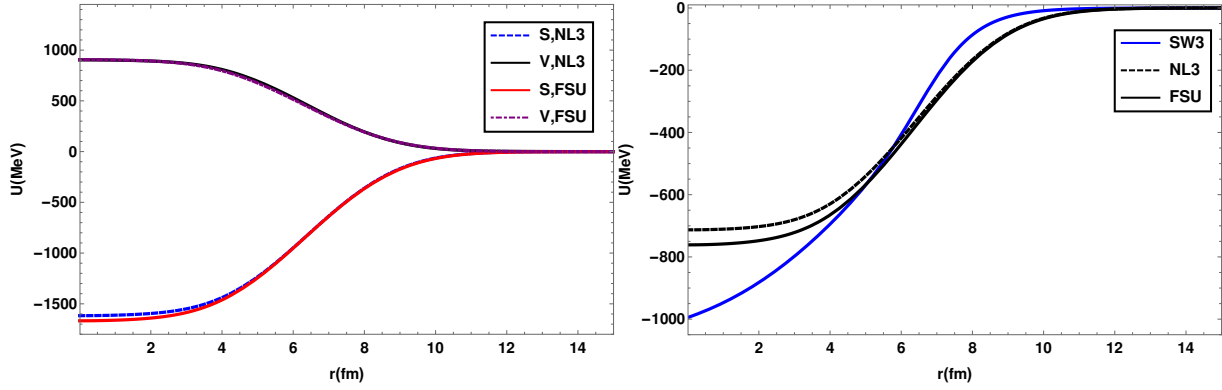


**Figure 4.13:** Plot of the individual scalar and vector potentials (left panel) for a typical parameter set, NL3 and FSU Lagrangian densities. The right panel is the total potential resulting from the near-cancellation of scalar and vector terms for  $^{20}\text{O} + ^{208}\text{Pb}$ , and the phenomenological Saxon-Woods potential, SW3 (blue line)

**Table 4.4:** Normalization constant for different potential models

Cluster-core	$\lambda_{M3Y}$	$\lambda_{CEG83a}$	$\lambda_{CEG83b}$	$\lambda_{NL3}$	$\lambda_{FSU}$	G
$^4\text{He} + ^{208}\text{Pb}$	0.53	0.56	0.90	0.97	1.00	18
$^{10}\text{Be} + ^{208}\text{Pb}$	0.54	0.57	0.82	0.93	0.93	50
$^{14}\text{C} + ^{208}\text{Pb}$	0.53	0.56	0.80	0.79	0.79	70
$^{20}\text{O} + ^{208}\text{Pb}$	0.52	0.56	0.80	0.93	0.88	100

$^{228}\text{Th}$  to  $^{20}\text{O}$ , this values also are smaller compared to the experiment. The same conclusions are drawn also for the relativistic mean field potential. The poor results for decay half-lives can be traced to the diffused surface of the nuclear potential resulting in large decay widths compared to values obtained from the experimental decay half-lives as shown in the table 4.5.

### 4.2.5 Energy Spectra with Microscopic Models Potential

The spectra are calculated using equation 2.4.31. Table 4.7, 4.8, 4.9 and 4.10 give the energy levels obtained with different double folding potentials. A clear analysis of the level obtained with the M3Y and CEG83 zero-range shows an inverted for the  $^{212}\text{Po}$  with highly bounded higher spin states. The finite-range



**Table 4.5:** Decay widths calculated with different potential models and their corresponding values extracted from experimental decay half – lives

$\Gamma(\text{MeV})$	${}^4_2\text{He}+{}^{208}_{82}\text{Pb}$	${}^{10}_4\text{Be}+{}^{208}_{82}\text{Pb}$	${}^{14}_6\text{C}+{}^{208}_{82}\text{Pb}$	${}^{20}_8\text{O}+{}^{208}_{82}\text{Pb}$
$\Gamma_{EXP}$	$1.521 \times 10^{-15}$	-	$1.369 \times 10^{-31}$	$8.550 \times 10^{-41}$
$\Gamma_{M3Y}$	$2.925 \times 10^{-15}$	$1.167 \times 10^{-41}$	$1.048 \times 10^{-29}$	$7.381 \times 10^{-38}$
$\Gamma_{CEG83a}$	$3.306 \times 10^{-15}$	$1.618 \times 10^{-41}$	$1.663 \times 10^{-29}$	$1.327 \times 10^{-37}$
$\Gamma_{CEG83b}$	$9.407 \times 10^{-15}$	$2.453 \times 10^{-40}$	$3.617 \times 10^{-28}$	$9.645 \times 10^{-36}$
$\Gamma_{NL3}$	$3.236 \times 10^{-14}$	$1.874 \times 10^{-40}$	$7.234 \times 10^{-27}$	$3.237 \times 10^{-36}$
$\Gamma_{FSU}$	$1.573 \times 10^{-13}$	$3.886 \times 10^{-39}$	$3.617 \times 10^{-27}$	$3.947 \times 10^{-36}$

exchange with CEG83 yields an inverted spectrum but less bounded almost for all spin states. Nevertheless we notice a good agreement between the spectra of  ${}^{218}\text{Rn}$ ,  ${}^{222}\text{Ra}$  and  ${}^{228}\text{Th}$  calculated with the non-relativistic potential, M3Y, CEG83a and CEG83b compared to experimental values. The measured band structure levels for  ${}^{212}\text{Po}$ ,  ${}^{218}\text{Rn}$  are taken from Mathematica package "IsotopeData", while for  ${}^{222}\text{Ra}$  and  ${}^{228}\text{Th}$ , they are obtained from [122, 123]. Ultimately, we notice all estimated levels are strongly compressed mostly for low spin states.

These necessitate an improvement of the mean-field double folding. We disregard the spectrum yielded by the relativistic potential since this will result probably to an inverted of highly compressed spectra due to the flat shape in the inner part of the potential for all cluster-core configurations that we selected. The reason why a hybrid potential is constructed and will be explained in the next section.

### 4.3 Hybrid Potential Construction

As we have seen before, despite all types of nucleon-nucleon effective interaction used, to obtain reasonable results, one requires to improve our model potentials. In this section we are going to construct hybrid potentials related to the realistic nuclear potential, the phenomenological modified Saxon-Woods. Here we shall investigate only the band structure and energy levels with electromagnetic properties of cluster states. We follow the scheme described in

**Table 4.6:** Decay half – lives obtained with different potential models

Cluster-core	${}^4_2\text{He}+{}^{208}_{82}\text{Pb}$	${}^{10}_4\text{Be}+{}^{208}_{82}\text{Pb}$	${}^{14}_6\text{C}+{}^{208}_{82}\text{Pb}$	${}^{20}_8\text{O}+{}^{208}_{82}\text{Pb}$
	(ns)	(s)	(yr)	(yr)
$T_{\frac{1}{2}}^{expt}$	300.000	-	105.700	$1.692 \times 10^{13}$
$T_{\frac{1}{2}}^{M3Y}$	156.000	$3.880 \times 10^{19}$	1.390	$1.980 \times 10^8$
$T_{\frac{1}{2}}^{CEG83a}$	138.000	$2.840 \times 10^{19}$	0.870	$1.100 \times 10^8$
$T_{\frac{1}{2}}^{CEG83b}$	48.400	$1.860 \times 10^{18}$	0.040	$1.510 \times 10^6$
$T_{\frac{1}{2}}^{NL3}$	14.100	$2.430 \times 10^{18}$	0.002	$4.470 \times 10^6$
$T_{\frac{1}{2}}^{FSU}$	2.900	$1.180 \times 10^{17}$	0.004	$3.950 \times 10^6$

[57]. This is achieved from fit near the surface region of the double folding by stepping through different values of the mixing parameter using the mathematica package NonLinearModelFit. Here we define the surface part of each microscopic potential as the asymptotic region starting from a radial position  $r$  where the potential falls to half of its maximum value to large  $r$ . The potential is then discretized in steps of 0.01 fm within this range. Therefore, for generating relevant bands of positive low-lying states from equation 2.4.31, a convenient handled scheme have been undertaken in order to include all levels belonging to the ground states band. This is achieved by normalizing the depth of the resulting potential until the quantity,

$$\chi^2 = \sum_L \left( E_L^{ext} - E_L^{calc} \right)^2 \quad (4.3.1)$$

is minimized.

Moreover as explained in [57], for light cluster such as  ${}^4\text{He}$  and  ${}^{10}\text{Be}$ , one requires a more attractive potential near the origin to overcome the shortcoming of the SW3 arising from the strong underbinded  $0^+$  ground state due to the effect of nuclear potential between  $r_1(0)$  and  $r_1(2)$  for the first turning point at  $0^+$  and  $2^+$  states. There is an additional correction term to the potential

**Table 4.7:** Spectrum of positive parity for  ${}^4_2\text{He} + {}^{208}_{82}\text{Pb}$  in MeV calculated with different potential models and their experimental values in MeV

$J^\pi$	$E_{\text{exp}}$	$E_{\text{M3Y}}$	$E_{\text{CEG83a}}$	$E_{\text{CEG83b}}$
$0^+$	0.000	-0.009	-0.007	0.000
$2^+$	0.727	-0.075	-0.065	-0.043
$4^+$	1.132	-0.236	-0.210	-0.148
$6^+$	1.355	-0.515	-0.466	-0.332
$8^+$	1.476	-0.939	-0.863	-0.612
$10^+$	1.834	-1.541	-1.442	-1.007
$12^+$	2.702	-2.359	-2.246	-1.526
$14^+$	2.885	-3.435	-3.329	-2.168
$16^+$	-	-4.798	-4.729	-2.925
$18^+$	2.921	-6.465	-6.474	-3.759

defined as

$$V_{\text{corr}}(r) = \begin{cases} -V_\delta & \text{for } r \leq r_0 \\ 0 & \text{for } r > r_0. \end{cases} \quad (4.3.2)$$

The value of  $r_0$  has been estimated to be [57]

$$r_0 \approx 1.132A_2^{-1}.$$

Tables 4.11, 4.12, 4.13 and 4.14, lists the optimized values of the hybrid potential resulting from different double folding potentials.

The tables 4.15, 4.16, 4.17 and 4.18 give numerical values of spectra for the positive low-lying states calculated with different hybrid potential models included their experimental values.

**Table 4.8:** Spectrum of positive parity for  ${}^4_2\text{Be} + {}^{208}_{82}\text{Pb}$  in MeV calculated with different potential models and their experimental values in MeV.

$J^\pi$	$E_{\text{exp}}$	$E_{\text{M3Y}}$	$E_{\text{CEG83a}}$	$E_{\text{CEG83b}}$
$0^+$	0.000	0.000	0.000	0.000
$2^+$	0.324	0.031	0.032	0.022
$4^+$	0.653	0.105	0.108	0.076
$6^+$	1.014	0.221	0.228	0.160
$8^+$	1.393	0.379	0.390	0.274
$10^+$	1.775	0.578	0.596	0.417
$12^+$	2.169	0.818	0.843	0.587
$14^+$	2.577	1.099	1.132	0.785
$16^+$	3.002	1.421	1.462	1.009
$18^+$	3.438	1.781	1.832	1.257
$20^+$	3.859	2.182	2.241	1.528
$22^+$	4.287	2.620	2.689	1.820
$24^+$	4.725	3.098	3.176	2.133
$26^+$	5.168	3.613	3.701	2.464

Note that these level structures are indeed in fair agreement with the observed values. We see the evident success of constructed the hybrid potential to reproduce the spectrum.

### 4.3.1 Electromagnetic Transitions

The transition Probabilities strength are calculated using equations [2.4.48](#) and [2.4.47](#)

**Table 4.9:** Spectrum of positive parity for  ${}^{14}_6\text{C} + {}^{208}_{82}\text{Pb}$  in MeV calculated with different potential models and their experimental values in MeV.

$J^\pi$	$E_{\text{exp}}$	$E_{\text{M3Y}}$	$E_{\text{CEG83a}}$	$E_{\text{CEG83b}}$
$0^+$	0.000	0.000	0.000	0.000
$2^+$	0.111	0.031	0.032	0.024
$4^+$	0.301	0.105	0.107	0.081
$6^+$	0.550	0.222	0.226	0.171
$8^+$	0.843	0.382	0.388	0.294
$10^+$	1.173	0.584	0.594	0.450
$12^+$	1.537	0.829	0.842	0.637
$14^+$	1.933	1.115	1.134	0.856
$16^+$	2.359	1.445	1.468	1.107
$18^+$	2.811	1.816	1.845	1.387
$20^+$	3.288	2.229	2.265	1.698

The table 4.19, 4.20, 4.21, and 4.22, list the relevant Weisskopf estimated probability transition strengths obtained from different potential models. We note that excellent agreement is obtained with few exceptions between the experimental [121–123] and calculated values. For exotic decay, we have used an effective charge expressed as

$$Z_i \longrightarrow Z_i + 0.17A_i. \quad (4.3.3)$$

The radial wave functions associated to each state are calculated by solving the radial Schrödinger equation 2.4.1. In average the trend show a kind of increase in the calculated when comparing different potential models. In particular, the computed value of the transition strengths for  ${}^{212}_{84}\text{Po}$  are twice or three times compared to the measured values. Eventually, for  ${}^{218}_{86}\text{Rn}$ , in table 4.20, the predicted transition  $B(E2; 2^+ \longrightarrow 0^+)$  is a reasonable agreement for almost all potential models.

**Table 4.10:** Spectrum of positive parity for  ${}^{20}_8\text{O} + {}^{208}_{82}\text{Pb}$  in MeV calculated with different potential models and their experimental values in MeV.

$J^\pi$	$E_{\text{exp}}$	$E_{\text{M3Y}}$	$E_{\text{CEG83a}}$	$E_{\text{CEG83b}}$
$0^+$	0.000	0.000	0.000	0.000
$2^+$	0.058	0.025	0.025	0.019
$4^+$	0.187	0.088	0.089	0.069
$6^+$	0.378	0.188	0.189	0.147
$8^+$	0.623	0.323	0.326	0.253
$10^+$	0.912	0.496	0.500	0.388
$12^+$	1.239	0.704	0.711	0.551
$14^+$	1.600	0.949	0.958	0.742
$16^+$	1.988	1.231	1.241	0.961
$18^+$	2.408	1.549	1.562	1.208

For  ${}^{228}_{90}\text{Th}$ , the reduced transitions  $B(E2; 2^+ \rightarrow 0^+)$  and  $B(E2; 4^+ \rightarrow 2^+)$  calculated are almost twice the measured value which is also a good agreement. For  ${}^{222}_{88}\text{Ra}$ , the experimental value  $B(E2; 2^+ \rightarrow 0^+)$ , although large but it is still a good estimation. However the unresolved mystery for  $B(E2; 4^+ \rightarrow 2^+)$  measured, which we expected to be higher, could not be predicted in our model as we can see in table 4.21.

### 4.3.2 Charge Radii Estimations

The mean square charge radius, which is an observable directly related to the proton density distribution is calculated using equation 2.5.1.

Table 4.23 summarizes the ground state root mean square radii of parent nuclei selected for different potential models. These calculated values are in excellent agreement with their measurable count part [124]. These significant values point out that a cluster description with maximum separation from the core give a good account of the size of the parent nucleus.

**Table 4.11:** Optimized parameters for SW3 potential for  ${}^{212}_{84}\text{Po}$ 

Parameters	$V_0(\text{Mev})$	a (fm)	x	R (fm)
M3Y	208.182	0.73	0.33	6.792
CEG83a	210.60	0.75	0.35	6.726
CEG83b	191.00	0.74	0.32	7.112
NL3	184.43	0.80	0.33	7.288
FSU	170.50	0.84	0.33	7.622

**Table 4.12:** Optimized parameters for SW3 potential for  ${}^{218}_{86}\text{Rn}$ 

Parameters	$V_0(\text{Mev})$	a (fm)	x	R (fm)
M3Y	506.54	0.976	0.51	6.717
CEG83a	506.56	0.99	0.52	6.701
CEG83b	466.28	0.918	0.41	7.299
NL3	484.78	0.95	0.43	7.11
FSU	479.14	1.100	0.51	6.961

Next in the same table are presented different deformation parameters calculated from static moments in equations 2.6.1 and 2.6.2 obtained from nuclear densities resulting from the relativistic mean field are taken from [125]. The values obtained are serve as benchmark to explain the cluster structures in nuclei. Starting from the deformation parameter of  ${}^{212}_{84}\text{Po}$  described as  ${}^4_2\text{He}+{}^{208}_{82}\text{Pb}$ , the deformation parameters increase gradually with the cluster size for the inert core taken as  ${}^{208}_{82}\text{Pb}$  for all even-even parent nuclei we have selected. These deformations are seen as a good probe which support strong evidence of clustering phenomena in nuclei.

**Table 4.13:** Optimized parameters for SW3 potential for  $^{222}_{88}\text{Ra}$ 

Parameters	$V_0(\text{Mev})$	a (fm)	x	R (fm)
M3Y	701.53	1.012	0.49	6.754
CEG83a	704.88	1.027	0.5	6.729
CEG83b	645.62	0.94	0.37	7.387
NL3	686.200	1.062	0.48	6.874
FSU	694.520	1.058	0.48	6.822

**Table 4.14:** Optimized parameters for SW3 potential for  $^{228}_{90}\text{Th}$ 

Parameters	$V_0(\text{Mev})$	a (fm)	x	R (fm)
M3Y	1010.31	1.040	0.45	6.804
CEG83a	1007.50	1.055	0.46	6.783
CEG83b	929.16	0.95	0.3	7.53
NL3	990.54	1.074	0.44	6.914
FSU	999.20	1.098	0.46	6.822



**Table 4.15:** Spectrum of positive parity for  ${}^4_2\text{He} + {}^{208}_{82}\text{Pb}$  in MeV calculated with different potential models and their experimental values in MeV.

$J^\pi$	$E_{\text{exp}}$	$E_{\text{M3Y}}$	$E_{\text{CEG83a}}$	$E_{\text{CEG83b}}$	$E_{\text{NL3}}$	$E_{\text{FSU}}$
$0^+$	0.000	0.061	0.003	0.002	0.005	0.060
$2^+$	0.727	0.727	0.727	0.727	0.728	0.736
$4^+$	1.132	1.036	1.065	1.023	1.033	1.027
$6^+$	1.355	1.448	1.507	1.405	1.429	1.403
$8^+$	1.476	1.914	2.002	1.833	1.875	1.828
$10^+$	1.834	2.384	2.496	2.267	2.330	2.261
$12^+$	2.702	2.803	2.926	2.659	2.744	2.653
$14^+$	2.885	3.101	3.212	2.951	3.057	2.947
$16^+$	-	3.188	3.250	3.067	3.188	3.063
$18^+$	2.921	2.917	2.872	2.884	3.001	2.870
$\chi^2$		10.67	11.46	9.76	10.61	9.711

**Table 4.16:** Spectrum of positive parity for  ${}^4_4\text{Be} + {}^{208}_{82}\text{Pb}$  in MeV calculated with hybrid potential models and their experimental values in MeV.

$J^\pi$	$E_{\text{exp}}$	$E_{\text{M3Y}}$	$E_{\text{CEG83a}}$	$E_{\text{CEG83b}}$	$E_{\text{NL3}}$	$E_{\text{FSU}}$
$0^+$	0.000	0.069	0.009	0.0009	-0.0029	-0.009
$2^+$	0.324	0.480	0.485	0.485	0.326	0.325
$4^+$	0.653	0.654	0.653	0.653	0.505	0.500
$6^+$	1.014	0.896	0.893	0.888	0.755	0.743
$8^+$	1.393	1.196	1.191	1.180	1.065	1.047
$10^+$	1.775	1.545	1.539	1.520	1.428	1.404
$12^+$	2.169	1.936	1.929	1.903	1.836	1.805
$14^+$	2.577	2.361	2.353	2.321	2.282	2.246
$16^+$	3.002	2.812	2.805	2.768	2.760	2.720
$18^+$	3.438	3.283	3.276	3.236	3.261	3.220
$20^+$	3.859	3.763	3.758	3.720	3.779	3.740
$22^+$	4.287	4.244	4.242	4.209	4.305	4.271
$24^+$	4.725	4.717	4.718	4.697	4.830	4.807
$26^+$	5.168	5.169	5.175	5.173	5.344	5.339
$\chi^2$		0.31	0.32	0.41	0.65	0.77

**Table 4.17:** Spectrum of positive parity for  ${}^6_6\text{C} + {}^{208}_{82}\text{Pb}$  in MeV calculated with hybrid potential models and their experimental values in MeV.

$J^\pi$	$E_{\text{exp}}$	$E_{\text{M3Y}}$	$E_{\text{CEG83a}}$	$E_{\text{CEG83b}}$	$E_{\text{NL3}}$	$E_{\text{FSU}}$
$0^+$	0.000	0.039	0.037	0.038	0.004	0.001
$2^+$	0.111	0.112	0.111	0.111	0.114	0.121
$4^+$	0.301	0.264	0.263	0.260	0.259	0.283
$6^+$	0.55	0.481	0.479	0.473	0.473	0.502
$8^+$	0.843	0.755	0.752	0.744	0.748	0.776
$10^+$	1.173	1.083	1.078	1.067	1.077	1.120
$12^+$	1.537	1.458	1.453	1.439	1.457	1.501
$14^+$	1.933	1.877	1.871	1.855	1.882	1.937
$16^+$	2.359	2.336	2.329	2.313	2.349	2.407
$18^+$	2.811	2.832	2.824	2.809	2.855	2.926
$20^+$	3.288	3.361	3.353	3.340	3.397	3.227
$\chi^2$		0.040	0.040	0.050	0.05	0.031

**Table 4.18:** Spectrum of positive parity for  ${}^{20}_8\text{O} + {}^{208}_{82}\text{Pb}$  in MeV calculated with hybrid potential models and their experimental values in MeV.

$J^\pi$	$E_{\text{exp}}$	$E_{\text{M3Y}}$	$E_{\text{CEG83a}}$	$E_{\text{CEG83b}}$	$E_{\text{NL3}}$	$E_{\text{FSU}}$
$0^+$	0.000	0.000	0.000	0.000	0.000	0.000
$2^+$	0.058	0.060	0.049	0.049	0.061	0.060
$4^+$	0.187	0.185	0.172	0.172	1.173	0.173
$6^+$	0.378	0.365	0.354	0.353	0.350	0.350
$8^+$	0.623	0.597	0.587	0.587	0.580	0.579
$10^+$	0.912	0.876	0.869	0.870	0.861	0.859
$12^+$	1.239	1.200	1.195	1.199	1.187	1.185
$14^+$	1.600	1.566	1.565	1.573	1.557	1.555
$16^+$	1.988	1.971	1.975	1.988	1.968	1.966
$18^+$	2.408	2.415	2.424	2.444	2.419	2.417
$\chi^2$		0.005	0.007	0.008	0.011	0.011

**Table 4.19:** Electromagnetic transitions calculated for different hybrid potentials along with experimental values in Weisskopf unit (W.u.), for  ${}^{212}_{84}\text{Po}$ 

Transitions	Exp	M3Y	CEG83a	CEG83b	NL3	FSU
$2^+ \longrightarrow 0^+$	-	4.5	4.5	5.2	6.0	7.2
$4^+ \longrightarrow 2^+$	-	6.2	6.3	7.3	8.4	10.0
$6^+ \longrightarrow 4^+$	$3.9 \pm 1$	6.4	6.5	7.5	8.6	10.3
$8^+ \longrightarrow 6^+$	$2.3 \pm 1$	6.0	6.1	7.0	8.2	9.7
$10^+ \longrightarrow 8^+$	$2.2 \pm 0.6$	5.3	5.4	6.2	7.2	8.6
$12^+ \longrightarrow 10^+$	-	4.4	4.5	5.2	5.9	7.1

**Table 4.20:** Electromagnetic transitions calculated for different hybrid potentials along with experimental values in Weisskopf unit (W.u.), for  ${}^{218}_{84}\text{Rn}$ 

Transitions	Exp	M3Y	CEG83a	CEG83b	NL3	FSU
$2^+ \longrightarrow 0^+$	$> 24.9$	27.2	27.7	30.4	30.0	34.9
$4^+ \longrightarrow 2^+$	-	38.6	39.3	43.2	42.6	49.5
$6^+ \longrightarrow 4^+$	-	42.1	42.8	47.1	46.4	53.9
$8^+ \longrightarrow 6^+$	-	43.4	44.1	48.5	47.8	48.5
$10^+ \longrightarrow 8^+$	-	43.6	44.3	48.8	48.1	51.3
$12^+ \longrightarrow 10^+$	-	43.2	43.8	48.5	47.6	55.6

**Table 4.21:** Electromagnetic transitions calculated for different hybrid potentials along with experimental values in Weisskopf unit (W.u.), for  $^{222}_{88}\text{Ra}$ 

Transitions	Exp	M3Y	CEG83a	CEG83b	NL3	FSU
$2^+ \rightarrow 0^+$	111	139	142	156	157	154
$4^+ \rightarrow 2^+$	11.83	198	202	222	224	219
$6^+ \rightarrow 4^+$	-	217	220	243	245	240
$8^+ \rightarrow 6^+$	-	225	228	252	254	249
$10^+ \rightarrow 8^+$	-	228	231	255	257	252
$12^+ \rightarrow 10^+$	-	228	232	256	258	253

**Table 4.22:** Electromagnetic transitions calculated for different hybrid potentials along with experimental values in Weisskopf unit (W.u.), for  $^{228}_{90}\text{Th}$ 

Transitions	Exp	M3Y	CEG83a	CEG83b	NL3	FSU
$2^+ \rightarrow 0^+$	$167 \pm 6$	300	303	328	326	332
$4^+ \rightarrow 2^+$	242	428	433	470	467	473
$6^+ \rightarrow 4^+$	-	469	474	515	512	517
$8^+ \rightarrow 6^+$	-	485	493	537	533	537
$10^+ \rightarrow 8^+$	-	493	501	545	540	545
$12^+ \rightarrow 10^+$	-	497	504	548	544	549

**Table 4.23:** The deformation parameters  $\beta_2$  calculated with NL3 Lagrangian, and cluster model predictions for the root mean square charge radii,  $\langle r_{ch}^2 \rangle^{1/2}$  in fm along with the measured values.

Nuclei	Exp	M3Y	CEG83a	CEG83b	NL3	FSU	$\beta_2$
${}_{84}^{212}\text{Po}$	-	5.5567	5.5572	5.5674	5.5673	5.5737	0.02
${}_{86}^{218}\text{Rn}$	5.6540	5.6461	5.6472	5.6542	5.6533	5.6649	0.046
${}_{88}^{222}\text{Ra}$	5.6874	5.7380	5.7398	5.7502	5.777	5.7491	0.066
${}_{90}^{228}\text{Th}$	5.7488	5.8544	5.8559	5.8676	5.8893	5.8908	0.158

## Chapter 5

# Conclusions and Outlook

We have shown that the binary cluster model gives a very good description of the ground state properties for  ${}_{84}^{212}\text{Po}$ ,  ${}_{86}^{218}\text{Rn}$ ,  ${}_{88}^{222}\text{Ra}$  and  ${}_{90}^{228}\text{Th}$ . We have defined these nuclei as a single composite particle orbiting an inert core characterized by its orbital angular momentum and number of nodes,  $L$  and  $n$ . We have outlined a technique of selecting the likely cluster-core configuration developed by Buck. We have made an assumption in which the correlated nucleons that build up the cluster structure have no internal excitation energy. The cluster states assigned to this binary cluster model are described as bound states and single-particle resonances of a local cluster-core potential. The two-body problem was solved by constructing various cluster-core potential models transcending from microscopic nonrelativistic, with different nucleon-nucleon interactions to the relativistic RLF amplitudes by the means of double folding. We have tested the new nucleon-nucleon density dependent effective interaction, the so-called Complex Effective Gaussian Form Factor (CEG) including the zero-range and the finite-range terms. Despite that this effective inter-nucleon interaction was designed for nucleon-nucleus optical potential, we have fixed the value of the Fermi momentum to calculate the cluster-core potential. We have found that the potential calculated with the zero-range looks similar to the M3Y. The finite-range exchange which is shallower seems to follow the shape of the phenomenological Saxon-Woods+Saxon-Woods cubed potential for almost all cluster-core decompositions we have described. Potentials calculated with the RLF are more diffused on the surface, but are shallower and exhibit a flat shape in the internal region compared to the Saxon-Woods cubed potential. Thus, the decay widths estimated are very large resulting in a small half-life except for  ${}^4_2\text{He}$  emitted from  ${}_{84}^{212}\text{Po}$  with M3Y and CEG83 plus zero-range effective interactions. The spectra obtained are negative with  ${}_{84}^{212}\text{Po}$  and highly compressed for  ${}_{86}^{218}\text{Rn}$ ,  ${}_{88}^{222}\text{Ra}$  and  ${}_{90}^{228}\text{Th}$ . These unsuccessful results led to the construction of a Saxon-Woods type hybrid potential for various potential models. The band structure and energy level ordering explaining the positive low-lying states are well reproduced. The electromagnetic



properties of cluster states such as transition probabilities and the root mean square charge radii are well described. The relativistic mean-field besides in explaining the structural properties of a number of nuclei provided also a reasonable benchmark for exploring the clustering phenomenon and particularly the shape of the nuclei. This is achieved by extracting the deformation parameters calculated from static moments. Future directions of this projects suggest a more improve nucleon-nucleon effective interaction which contains three-body correlations. In fact the three-body forces play important roles in probing the shape and strength of nucleus-nucleus potential at short relative distances. Else, an alternative way is to add a proximity potential around the spatial region where the two interacting nuclei just touch their surfaces. This could probably enhance both the level structure and dynamic properties such as the decay process. New suggestions for the density dependent (meson coupling constant), effective Lagrangian are needed. This should take into account the pairing when investigating clustering shape since the parents nuclei are even-even open-shell. The nuclear densities obtained from relativistic mean field should be less diffused at the surface.

# List of References

- [1] Carl Friedrich von Weizsäcker. Newer model demonstrations about the construction of atomic nuclei. conclusion. *Naturwissenschaften*, 26:209–217, April 1938.
- [2] Vijay R. Pandharipande, Ingo Sick, and Peter K. A. de Witt Huberts. Independent particle motion and correlations in fermion systems. *Rev. Mod. Phys.*, 69:981–991, Jul 1997.
- [3] A. Bohr and B. R. Mottelson. *Nuclear Structure*. World Scientific, 1998.
- [4] E. N. Da and C. Andrade. *Rutherford and the Nature of the Atom*. 1965.
- [5] John A. Wheeler. On the mathematical description of light nuclei by the method of resonating group structure. *Phys. Rev.*, 52:1107–1122, Dec 1937.
- [6] A. Sandulescu and W. Greiner. Mass asymmetry in fission, fusion and mass transfer due to the fragmentation in valleys. *Journal of Physics G: Nuclear Physics*, 3(8):L189, 1977.
- [7] H. J. Rose and G. A. Jones. A new kind of natural radioactivity. *Nature*, 307:245–247, Jan 1984.
- [8] S. Gales, E. Hourani, M. Hussonnois, J. P. Schapira, L. Stab, and M. Vergnes. Exotic nuclear decay of  $^{223}\text{Ra}$  by emission of  $^{14}\text{C}$  nuclei. *Phys. Rev. Lett.*, 53:759–762, Aug 1984.
- [9] P. B. Price, J. D. Stevenson, S. W. Barwick, and H. L. Ravn. Discovery of radioactive decay of  $^{222}\text{Ra}$  and  $^{224}\text{Ra}$  by  $^{14}\text{C}$  emission. *Phys. Rev. Lett.*, 54:297–299, Jan 1985.
- [10] W. Kutschera, I. Ahmad, S. G. Armato, A. M. Friedman, J. E. Gindler, W. Henning, T. Ishii, M. Paul, and K. E. Rehm. Spontaneous  $^{14}\text{C}$  emission from  $^{223}\text{Ra}$ . *Phys. Rev. C*, 32:2036–2042, Dec 1985.
- [11] E. Hourani, M. Hussonnois, L. Stab, L. Brillard, S. Gales, and J. P. Schapira. Evidence for the radioactive decay of  $^{226}\text{Ra}$  by  $^{14}\text{C}$  emission. *Physics Letters B*, 160(6):375 – 379, 1985.
- [12] M. Greiner and W. Scheid. Radioactive decay into excited states via heavy ion emission. *Journal of Physics G: Nuclear Physics*, 12(10):L229, 1986.

- [13] Yi-Jin Shi and W. J. Swiatecki. Theoretical estimates of the rates of radioactive decay of radium isotopes by  $^{14}\text{C}$  emission. *Phys. Rev. Lett.*, 54:300–301, Jan 1985.
- [14] Satish Kumar and Raj K. Gupta. Measurable decay modes of barium isotopes via exotic cluster emissions. *Phys. Rev. C*, 49:1922–1926, Apr 1994.
- [15] Mihai Horoi. Scaling behaviour in cluster decay. *Journal of Physics G: Nuclear and Particle Physics*, 30(7):945, 2004.
- [16] K. P. Santhosh, R. K. Biju, and Antony Joseph. A semi-empirical model for  $\alpha$  and cluster radioactivity. *Journal of Physics G: Nuclear and Particle Physics*, 35(8):085102, 2008.
- [17] A. I. Budaca, R. Budaca, and I. Silisteanu. Extended systematics of alpha decay half lives for exotic superheavy nuclei. *Nuclear Physics A*, 951:60 – 74, 2016.
- [18] S. W. Barwick, P. B. Price, and J. D. Stevenson. Radioactive decay of  $^{232}\text{U}$  by  $^{24}\text{Ne}$  emission. *Phys. Rev. C*, 31:1984–1986, May 1985.
- [19] L. M. COOK & A. MARKERT P. B. PRICE. Phosphate glasses for identification of heavy ions. *Nature*, 325:137 – 138, Jan 1987.
- [20] G. Audi, O. Bersillon, J. Blachot, and A. H. Wapstra. The nubase evaluation of nuclear and decay properties. *Nuclear Physics A*, 729(1):3 – 128, 2003. The 2003 NUBASE and Atomic Mass Evaluations.
- [21] R. G. Lovas, R. J. Liotta, A. Insolia, K. Varga, and D. S. Delion. Microscopic theory of cluster radioactivity. *Physics Reports*, 294(5):265 – 362, 1998.
- [22] D. N. Basu. Role of effective interaction in nuclear disintegration processes. *Physics Letters B*, 566(2):90 – 97, 2003.
- [23] D. N. Basu. Folding model analysis of alpha radioactivity. *Journal of Physics G: Nuclear and Particle Physics*, 29(9):2079, 2003.
- [24] S. S. Malik and Raj K. Gupta. Theory of cluster radioactive decay and of cluster formation in nuclei. *Phys. Rev. C*, 39:1992–2000, May 1989.
- [25] W. von Oertzen, Martin Freer, and Yoshiko Kanada-En'yo. Nuclear clusters and nuclear molecules. *Physics Reports*, 432(2):43 – 113, 2006.
- [26] W. Greiner, J. Y. Park, and W. Scheid. *Nuclear Molecules*. 1995.
- [27] B. Buck, A. C. Merchant, M. J. Horner, and S. M. Perez. Choosing cluster and core in cluster models of nuclei. *Phys. Rev. C*, 61:024314, Jan 2000.
- [28] G. Royer and R. Moustabchir. Light nucleus emission within a generalized liquid-drop model and quasimolecular shapes. *Nuclear Physics A*, 683(1):182 – 206, 2001.

- [29] B. Buck, A. C. Merchant, and S. M. Perez. Coexistence of very dissimilar cluster bands in  $^{212}\text{Po}$ . *Journal of Physics G: Nuclear and Particle Physics*, 30(2):65, 2004.
- [30] B. Buck, A. C. Merchant, V. A. McBride, and S. M. Perez. Cluster model analysis of yb spectra. *Journal of Physics G: Nuclear and Particle Physics*, 30(10):1371, 2004.
- [31] C. Beck. *Clusters in Nuclei, volume 3*. Lecture Notes in Physics. Springer International Publishing, 2013.
- [32] P. Arumugam, B. K. Sharma, S. K. Patra, and Raj K. Gupta. Relativistic mean field study of clustering in light nuclei. *Phys. Rev. C*, 71:064308, Jun 2005.
- [33] J. A. Maruhn, Masaaki Kimura, S. Schramm, P. G. Reinhard, H. Horiuchi, and A. Tohsaki.  $\alpha$ -cluster structure and exotic states in a self-consistent model for light nuclei. *Phys. Rev. C*, 74:044311, Oct 2006.
- [34] P. G. Reinhard, J. A. Maruhn, A. S. Umar, and V. E. Oberacker. Localization in light nuclei. *Phys. Rev. C*, 83:034312, Mar 2011.
- [35] B. Buck, A. C. Merchant, and S. M. Perez. Systematics of alpha-cluster states above double shell closures. *Phys. Rev. C*, 51:559–565, Feb 1995.
- [36] B. Buck, C. B. Dover, and J. P. Vary. Simple potential model for cluster states in light nuclei. *Phys. Rev. C*, 11:1803–1821, May 1975.
- [37] B. Buck and A. C. Merchant. Cluster-model calculations of exotic decays from heavy nuclei. *Phys. Rev. C*, 39:2097–2100, May 1989.
- [38] B. Buck, A. C. Merchant, and S. M. Perez. New look at  $\alpha$  decay of heavy nuclei. *Phys. Rev. Lett.*, 65:2975–2977, Dec 1990.
- [39] B. Buck, A. C. Merchant, and S. M. Perez. Ground state to ground state alpha decays of heavy even-even nuclei. *Journal of Physics G: Nuclear and Particle Physics*, 17(8):1223, 1991.
- [40] Shigeo Ohkubo. Alpha clustering and structure of  $^{94}\text{Mo}$  and  $^{212}\text{Po}$ . *Phys. Rev. Lett.*, 74:2176–2179, Mar 1995.
- [41] B. Buck, A. C. Merchant, and S. M. Perez. Exotic cluster states in actinide nuclei. *Phys. Rev. Lett.*, 76:380–383, Jan 1996.
- [42] B. Buck, A. C. Merchant, and S. M. Perez. Exotic cluster states in actinide nuclei. *Phys. Rev. Lett.*, 76:380–383, Jan 1996.
- [43] B. Buck, A. C. Merchant, and S. M. Perez. Alternative view of collective bands in actinide nuclei. *Phys. Rev. C*, 57:R2095–R2098, May 1998.
- [44] B. Buck, A. C. Merchant, and S. M. Perez. Systematic study of exotic clustering in even-even actinide nuclei. *Phys. Rev. C*, 58:2049–2060, Oct 1998.

- [45] B. Buck, A. C. Merchant, and S. M. Perez. Cluster model interpretation of normal and superdeformed bands in  $^{60}\text{Zn}$ . *Phys. Rev. C*, 61:014310, Dec 1999.
- [46] B. Buck, A. C. Merchant, and S. M. Perez. Cluster structure and  $\gamma$  transitions in actinide nuclei. *Phys. Rev. C*, 59:750–754, Feb 1999.
- [47] B. Buck, A. C. Merchant, S. M. Perez, and H. E. Seals. The exotic structure of heavy nuclei. *Journal of Physics G: Nuclear and Particle Physics*, 31(12):1499, 2005.
- [48] F. R. Xu, S. M. Wang, Z. J. Lin, and J. C. Pei. Alpha-decay quantum-tunnelling calculations based on a folded woods-saxon potential. *Journal of Physics: Conference Series*, 436(1):012064, 2013.
- [49] Dongdong Ni and Zhongzhou Ren. Microscopic calculation of  $\alpha$ -decay half-lives within the cluster model. *Nuclear Physics A*, 825(3):145 – 158, 2009.
- [50] Zhongzhou Ren, Chang Xu, and Zaijun Wang. New perspective on complex cluster radioactivity of heavy nuclei. *Phys. Rev. C*, 70:034304, Sep 2004.
- [51] Chang Xu and Zhongzhou Ren. Systematical calculation of  $\alpha$  decay half-lives by density-dependent cluster model. *Nuclear Physics A*, 753(1):174 – 185, 2005.
- [52] Chang Xu and Zhongzhou Ren. Favored  $\alpha$ -decays of medium mass nuclei in density-dependent cluster model. *Nuclear Physics A*, 760(3):303 – 316, 2005.
- [53] Z Ren and C Xu. Alpha decay half-lives of odd-z superheavy elements  $z = 115$ -113-111. *Journal of Physics: Conference Series*, 111(1):012040, 2008.
- [54] G. Röpke, P. Schuck, Y. Funaki, H. Horiuchi, Zhongzhou Ren, A. Tohsaki, Chang Xu, T. Yamada, and Bo Zhou. Nuclear clusters bound to doubly magic nuclei: The case of  $^{212}\text{Po}$ . *Phys. Rev. C*, 90:034304, Sep 2014.
- [55] T. T. Ibrahim, S. M. Perez, and S. M. Wyngaardt. Hybrid potential model of the  $\alpha$ -cluster structure of  $^{212}\text{Po}$ . *Phys. Rev. C*, 82:034302, Sep 2010.
- [56] T. T. Ibrahim, S. M. Perez, S. M. Wyngaardt, B. Buck, and A. C. Merchant. Hybrid potential analysis of exotic clustering in heavy nuclei. *Phys. Rev. C*, 85:044313, Apr 2012.
- [57] T. T. Ibrahim, S. M. Wyngaardt, and B. D. C. Kimene Kaya. Analysis of the clustering in  $^{212}\text{Po}$ ,  $^{218}\text{Rn}$  and  $^{232}\text{U}$ . *Nuclear Physics A*, 966:73 – 81, 2017.
- [58] Norio Yamaguchi, Sinobu Nagata, and Takaaki Matsuda. Optical model potential in the lowest order brueckner theory and complex effective n-n interaction. *Progress of Theoretical Physics*, 70(2):459, 1983.
- [59] C. J. Horowitz. Relativistic love-franey model: Covariant representation of the nn interaction for n-nucleus scattering. *Phys. Rev. C*, 31:1340–1348, Apr 1985.

- [60] D. P. Murdock and C. J. Horowitz. Microscopic relativistic description of proton-nucleus scattering. *Phys. Rev. C*, 35:1442–1462, Apr 1987.
- [61] C. Beck. *Clusters in Nuclei, volume 2*. Lecture Notes in Physics. Springer Berlin Heidelberg, 2012.
- [62] Erasmus Johannes du Toit. Cluster model analysis of exotic decay in actinide nuclei. Master's thesis, Department of Physics, University of Stellenbosch, 2014.
- [63] Ibrahim Taofiq Toyin. *A cluster study of the nuclei  $^{212}\text{Po}$  and  $^{218}\text{Rn}$* . PhD thesis, Stellenbosch University, 2009.
- [64] B. Buck, A. C. Merchant, and S. M. Perez.  $\alpha$  decay calculations with a realistic potential. *Phys. Rev. C*, 45:2247–2253, May 1992.
- [65] K. Wildermuth and Th. Kanellopoulos. The cluster model of the atomic nuclei. *Nuclear Physics*, 7:150 – 162, 1958.
- [66] S. A. Gurvitz and G. Kalbermann. Decay width and the shift of a quasistationary state. *Phys. Rev. Lett.*, 59:262–265, Jul 1987.
- [67] S. A. Gurvitz. Novel approach to tunneling problems. *Phys. Rev. A*, 38:1747–1759, Aug 1988.
- [68] B. Buck, A. C. Merchant, S. M. Perez, and P. Tripe. Diffuse well analysis of exotic decay of heavy nuclei. *Phys. Rev. C*, 47:1307–1308, Mar 1993.
- [69] V. E. Viola and G. T. Seaborg. Nuclear systematics of the heavy elements lifetimes for  $\alpha$ ,  $\beta$  and spontaneous fission decay. *Journal of Inorganic and Nuclear Chemistry*, 28(3):741 – 761, 1966.
- [70] N. Zettili. *Quantum Mechanics: Concepts and Applications*. John Wiley and Sons, 2001.
- [71] K. Gottfried and G. Kalbermann. *Quantum Mechanics: Fundamentals*. Springer, New York, 2004.
- [72] Samuel S.M. Wong. *Introductory Nuclear Physics*. Wiley-VCH Verlag GmbH & Co. KGaA, 2004.
- [73] D. M. Brink and G. R. Satchler. *Angular Momentum*. Oxford Univ. Press, N. Y., 1993.
- [74] V. F. Weisskopf. Radiative transition probabilities in nuclei. *Phys. Rev.*, 83:1073–1073, Sep 1951.
- [75] B. Buck and A. A. Pilt. Alpha-particle and triton cluster states in  $^{19}\text{F}$ . *Nuclear Physics A*, 280(1):133 – 160, 1977.
- [76] Herman Feshbach. Unified theory of nuclear reactions. *Annals of Physics*, 5(4):357 – 390, 1958.

- [77] Herman Feshbach. A unified theory of nuclear reactions. ii. *Annals of Physics*, 19(2):287 – 313, 1962.
- [78] N. K. Glendenning. *Direct nuclear reactions*. Academic Press, 1983.
- [79] M. B. Johnson and A. Picklesimer. *Relativistic dynamics and quark-nuclear physics*. J. Wiley, 1986.
- [80] Khin Maung Maung and Franz Gross. Covariant multiple scattering series for elastic projectile-target scattering. *Phys. Rev. C*, 42:1681–1693, Oct 1990.
- [81] A. K. Kerman, H. McManus, and R. M. Thaler. The scattering of fast nucleons from nuclei. *Annals of Physics*, 8(4):551 – 635, 1959.
- [82] Khin Maung Maung, John W. Norbury, and Trina Coleman. Relativistic multiple scattering theory and the relativistic impulse approximation. *Journal of Physics G: Nuclear and Particle Physics*, 34(9):1861, 2007.
- [83] F. A. Brieva and J. R. Rook. Nucleon-nucleus optical model potential. *Nuclear Physics A*, 291(2):299 – 316, 1977.
- [84] K. Nakayama and W. G. Love. Effective interaction for nucleon-nucleus scattering based on a one-boson-exchange model. *Phys. Rev. C*, 38:51–73, Jul 1988.
- [85] L. Rikus, K. Nakano, and H. V. Von Geramb. Microscopic analysis of elastic and inelastic proton scattering from  $^{12}\text{C}$ . *Nuclear Physics A*, 414(3):413 – 455, 1984.
- [86] Norio Yamaguchi, Sinobu Nagata, and Junji Michiyama. Systematic analyses of proton elastic scattering between  $65 < E_p < 200$  mev with microscopic effective interaction. *Progress of Theoretical Physics*, 76(6):1289, 1986.
- [87] T. Furumoto, Y. Sakuragi, and Y. Yamamoto. New complex  $g$ -matrix interactions derived from two- and three-body forces and application to proton-nucleus elastic scattering. *Phys. Rev. C*, 78:044610, Oct 2008.
- [88] T. Furumoto, Y. Sakuragi, and Y. Yamamoto. Effect of repulsive and attractive three-body forces on nucleus-nucleus elastic scattering. *Phys. Rev. C*, 80:044614, Oct 2009.
- [89] K. A. Brueckner and J. L. Gammel. Properties of nuclear matter. *Phys. Rev.*, 109:1023–1039, Feb 1958.
- [90] F. Petrovich, R. J. Philpott, A. W. Carpenter, and J. A. Carr. Spin dependence in the nucleus-nucleus optical potential. *Nuclear Physics A*, 425(3):609 – 652, 1984.
- [91] C. D. Goodman. *The (p,n) Reaction and the Nucleon-Nucleon Force*. Springer US, 2012.

- [92] G. R. Satchler and W. G. Love. Folding model potentials from realistic interactions for heavy-ion scattering. *Physics Reports*, 55(3):183 – 254, 1979.
- [93] A. K. Chaudhuri, D. N. Basu, and Bikash Sinha. An alpha-nucleus optical potential using a realistic effective interaction. *Nuclear Physics A*, 439(3):415 – 426, 1985.
- [94] A. K. Chaudhuri and Bikash Sinha. A microscopic optical model analysis of heavy ion elastic scattering data using the realistic nn interaction. *Nuclear Physics A*, 455(1):169 – 178, 1986.
- [95] Dao Tien Khoa. Exchange effects in nuclear rainbow scattering. *Nuclear Physics A*, 484(2):376 – 396, 1988.
- [96] L. D. Miller and A. E. S. Green. Relativistic self-consistent meson field theory of spherical nuclei. *Phys. Rev. C*, 5:241–252, Jan 1972.
- [97] L. D. Miller. Exchange potentials in relativistic hartree-fock theory of closed-shell nuclei. *Phys. Rev. C*, 9:537–554, Feb 1974.
- [98] Charles M. Werneth. Nucleus-nucleus relativistic multiple scattering theory with delta degrees of freedom. *Can. J. Phys.*, 91:424–432, 2013.
- [99] J. A. Tjon and S. J. Wallace. Symmetric, lorentz invariant nn amplitude: Yukawa representation. *Phys. Rev. C*, 35:280–297, Jan 1987.
- [100] J. A. Tjon and S. J. Wallace. Generalized impulse approximation for relativistic proton scattering. *Phys. Rev. C*, 36:1085–1104, Sep 1987.
- [101] L. Ray, G. W. Hoffmann, and W. R. Coker. Nonrelativistic and relativistic descriptions of proton-nucleus scattering. *Physics Reports*, 212(5):223 – 328, 1992.
- [102] J. A. McNeil, J. R. Shepard, and S. J. Wallace. Impulse-approximation dirac optical potential. *Phys. Rev. Lett.*, 50:1439–1442, May 1983.
- [103] Z. P. Li, G. C. Hillhouse, and J. Meng. Energy-dependent lorentz covariant parameterization of the *NN* interaction between 50 and 200 mev. *Phys. Rev. C*, 77:014001, Jan 2008.
- [104] O. V. Maxwell. Energy-dependent lorentz covariant representation of the nn interaction. *Nuclear Physics A*, 600(4):509 – 528, 1996.
- [105] J. D. Walecka. A theory of highly condensed matter. *Annals of Physics*, 83(2):491 – 529, 1974.
- [106] G. E. Brown and Mannque Rho. Scaling effective lagrangians in a dense medium. *Phys. Rev. Lett.*, 66:2720–2723, May 1991.
- [107] G. Krein, Th. A. J. Maris, B. B. Rodrigues, and E. A. Veit. Medium effects on spin observables of proton knockout reactions. *Phys. Rev. C*, 51:2646–2655, May 1995.



- [108] F. A. Brieva and J.R. Rook. Nucleon-nucleus optical model potential. *Nuclear Physics A*, 291(2):317 – 341, 1977.
- [109] C. J. Horowitz and Brian D. Serot. Self-consistent hartree description of finite nuclei in a relativistic quantum field theory. *Nuclear Physics A*, 368(3):503 – 528, 1981.
- [110] Y. K. Gambhir, P. Ring, and A. Thimet. Relativistic mean field theory for finite nuclei. *Annals of Physics*, 198(1):132 – 179, 1990.
- [111] J. Boguta. Ground state properties of  $^{16}\text{O}$ ,  $^{40}\text{Ca}$  and  $^{48}\text{Ca}$  in a relativistic hartree theory of nuclear matter. *Nuclear Physics A*, 372(3):386 – 396, 1981.
- [112] C. J. Horowitz and Brian D. Serot. Relativistic hartree theory of finite nuclei: The role of the quantum vacuum. *Physics Letters B*, 140(3):181 – 186, 1984.
- [113] G. A. Lalazissis, J. König, and P. Ring. New parametrization for the lagrangian density of relativistic mean field theory. *Phys. Rev. C*, 55:540–543, Jan 1997.
- [114] C. J. Horowitz and J. Piekarewicz. Neutron star structure and the neutron radius of  $^{208}\text{Pb}$ . *Phys. Rev. Lett.*, 86:5647–5650, Jun 2001.
- [115] R. Utama, Wei-Chia Chen, and J. Piekarewicz. Nuclear charge radii: density functional theory meets bayesian neural networks. *Journal of Physics G: Nuclear and Particle Physics*, 43(11):114002, 2016.
- [116] B. G. Todd-Rutel and J. Piekarewicz. Neutron-rich nuclei and neutron stars: A new accurately calibrated interaction for the study of neutron-rich matter. *Phys. Rev. Lett.*, 95:122501, Sep 2005.
- [117] J. D. Bjorken and S. D. Drell. *Relativistic quantum mechanics*. International series in pure and applied physics. McGraw-Hill, 1964.
- [118] BIS Van der Ventel. Code provided by bis van der ventel. private communications. 2000.
- [119] K. V. Lukyanov. Double folding model of nucleus-nucleus potential: Formulae, iteration method and computer code. Communication of the Joint Institute for Nuclear Research., 2007.
- [120] Dao Tien Khoa, A. Faessler, and N. Ohtsuka. Exchange part of the real heavy-ion optical potential within the double-folding model and the nuclear matter approach. *Journal of Physics G: Nuclear and Particle Physics*, 16(8):1253, 1990.
- [121] A. B. Garnsworthy, N. J. Thompson, Zs Podolyak, P. M. Walker, S. J. Williams, G. D. Dracoulis, G. de France, G. J. Lane, K. Andgren, A. M. Bruce, A. P. Byrne, W. N. Catford, B. Cederwall, G. A. Jones, B. McGuirk, S. Mandal, E. S. Paul, V. Pucknell, N. Redon, B. Rosse, R. J. Senior, and G. Sletten. Spectroscopy of  $^{212}\text{Po}$  and  $^{213}\text{At}$  using a  $^8\text{He}$  radioactive beam and exogam. *Journal of Physics G: Nuclear and Particle Physics*, 31(10):S1851, 2005.

- [122] Y. A. Akovali. Nuclear data sheets for  $A = 222$ . *Nuclear Data Sheets*, 77(1):271 – 298, 1996.
- [123] Agda Artna-Cohen. Nuclear data sheets for  $A = 228$ . *Nuclear Data Sheets*, 80(3):723 – 786, 1997.
- [124] I. Angeli and K. P. Marinova. Table of experimental nuclear ground state charge radii: An update. *Atomic Data and Nuclear Data Tables*, 99(1):69 – 95, 2013.
- [125] G. A. Lalazissis, S. Raman, and P. Ring. Ground-state properties of even even nuclei in the relativistic mean-field theory. *Atomic Data and Nuclear Data Tables*, 71(1):1 – 40, 1999.